The Dissertation Committee for Yaoyu Pang

certifies that this is the approved version of the following dissertation:

Surface Evolution and Self Assembly of Epitaxial Thin Films: Nonlinear and Anisotropic Effects

Committee:

Rui Huang, Supervisor

K.Ravi-Chandar

Kenneth Liechti

Shaochen Chen

Sanjay Banerjee

Surface Evolution and Self Assembly of Epitaxial Thin Films: Nonlinear and Anisotropic Effects

by

Yaoyu Pang, B.S., M.S.E.

Dissertation

Presented to the Faculty of the Graduate School of

The University of Texas at Austin

in Partial Fulfillment

of the Requirements

for the Degree of

Doctor of Philosophy

The University of Texas at Austin

December 2007

To my family

Acknowledgments

On completion of this dissertation, I owe my gratitude to all those people who have made this possible and because of whom my graduate experience has been one that I will cherish forever.

Foremost, on the academic front, I wish to thank my advisor Dr. Rui Huang, a gracious mentor and good friend who encouraged me to develop independent thinking and research skills throughout my doctoral work. Without his guidance and patience, this dissertation would not have been possible.

I am very grateful for having an exceptional doctoral committee and wish to thank Dr. K. Ravi-Chandar, Dr. Kenneth Liechti, Dr. Shaochen Chen, and Dr. Sanjay Banerjee for their generous time and commitment. I would also like to express my deepest gratitude to my fellow graduate students, Bin Li, Ying Tian, Sehyuk Im, Min Kyoo Kang, Dewei Xu and many others who I have interacted with over the years. They have created a friendly and productive environment that is difficult to match elsewhere.

Finally, and most importantly, I owe my warmest thanks to my family. Their love, support, encouragement, unwavering faith and confidence in me were undeniably the bedrock upon which the past few years of my life have been built.

Yaoyu Pang

The University of Texas at Austin

December 2007

Surface Evolution and Self Assembly of Epitaxial Thin Films: Nonlinear and Anisotropic Effects

Publication No. _____

Yaoyu Pang, Ph.D.

The University of Texas at Austin, 2007

Supervisor: Rui Huang

A strained epitaxial film can undergo surface instability and self assemble into discrete islands. The unique physical features of these islands make self-assembly an enabling technique for advanced device technology while control of the island size, shape, and alignment is critical. During the process of self-assembly, the stress field and the interface interaction have profound effects on the dynamics of surface evolution. In this dissertation, a continuum model is developed to study the nonlinear dynamics of surface pattern evolution and self assembly in epitaxial thin films. Within the framework of

non-equilibrium thermodynamics, a nonlinear evolution equation is developed, and a spectral method is implemented for numerical simulations. The effects of stress and wetting are examined. It is found that, without wetting, the nonlinear stress field induces a "blow-up" instability. With wetting, the thin film self assembles into an array of discrete islands lying on a thin wetting layer. The dynamics of island formation and coarsening over a long time and a large area is well captured by the interplay of the nonlinear stress field and the wetting effect in the present model.

For single-crystal epitaxy, the anisotropic material properties in the bulk and surface play important roles in the process of self assembly and pattern formation. In particular, this study investigates the effects of anisotropic mismatch stress and generally anisotropic elasticity. First, under an anisotropic mismatch stress, a bifurcation of surface pattern is predicted. The effect of anisotropic elasticity on pattern evolution is then investigated for two specific systems, one for SiGe films on Si substrates with different surface orientations, and the other for hexagonal silicides on Si substrates. It is shown that the consideration of elastic anisotropy reveals a much richer dynamics of surface pattern evolution as opposed to isotropic models. Based on the theoretical and numerical results from the present study, experimental approaches may be developed to control the size and organization of self assembled surface patterns in epitaxial systems.

Contents

List of Tables

List of Figures

xiv

xvii

Chapter 1

Introduction

1.1 Background and motivation

Since Gordon Moore first predicted in 1965 [1] that the number of transistors per integrated circuit chip would continue to double in each technology generation, the microelectronics industry has followed an exponential progress based on scaling down device features. However, significant challenges to decrease the limiting feature size will be faced in the near future [2]. Therefore, it has been recognized that the development of future microelectronics industry may rely on the establishment of alternative fabrication methods and novel device structures. In particular, unique quantum phenomena in low-dimensional electronic materials such as quantum wells, wires and dots (Fig.1.1) have been demonstrated due to their ultra small dimensions. The confinement in one (well), two (wire) and three (dots) dimensions discretizes the density of states, enabling great tunability for adsorption and emission of electrons or holes, and resulting in superb transport and opto-electrionic properties [3]. With advan-
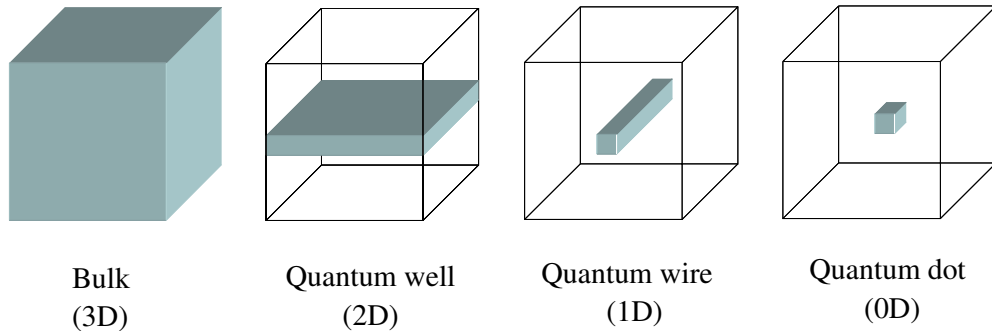
Figure 1.1: Schematic illustration of different forms of electronic materials.

tages for high device integration and ultra-low power consumption, this kind of nanostructure based device has great prospects to revolutionize conventional technology.

The rapid growth of the microelectronics technology in the past two decades has been enabled by sustained advances in essentially two different fabrication paradigms, respectively referred to as "top-down" and "bottom-up" [4, 5]. The *top-down* method begins with large homogeneous objects and removes material as needed to create smaller-scale structures. Lithography, etching, and epitaxial growth techniques are all belonging to the *top-down* method. As device sizes continue to shrink toward the nanometer scale, however, these "traditional" technologies will encounter significant limitations [6]. To fully develop nanoelectronics technology, low-cost and high-throughput manufacturing techniques are essential [6, 7].

During the last several years, development of the unconventional *bottom-up* method for fabricating nanostructures has drawn tremendous research ef-

fort across the world. A *bottom-up* approach involves putting together smaller components to form a larger or more complex system, during which chemical, physical, and biological processes may coexist [8, 9]. Self-assembly offers such an atom-by-atom synthesis approach, which is universally conceded to be the prime route to manufacturable functional nanoscale systems. In self-assembly, subunits (atoms, molecules, or mesoscale objects) spontaneously organize and form stable, well-defined structures. Because the final self-assembled structures are at or close to thermodynamic equilibrium, they tend to reject defects [10]. A variety of strategies for self-assembly have been developed to fabricate structures with dimensions ranging from molecular, through mesoscopic, to macroscopic sizes. Examples include self-assembled monolayers, phase-separated block copolymers, and colloidal particles. However, the development of these methods into practical routes to useful nanostructures still requires great ingenuity. Neither our understanding nor our control of self-assembly is adequate to map out the road to achieving the desired functionality and versatility that is already achieved routinely by the most lowly forms of living organisms in nature.

Motivated by the exciting developments of nanofabrication and self assembly in the recent years, the research objective of this dissertation is to develop a fundamental understanding on the dynamic process of self assembly in epitaxial systems.

1.2   Epitaxy and self assembly

1.2.1   Thin film growth

Various thin film growth methods have been developed. The growth process could be as simple as depositing atoms onto a substrate surface such as in molecular beam epitaxy (MBE) and related sputtering techniques [4]. More complex process may involve chemical reactions on the substrate surface, e.g., chemical vapor deposition (CVD) [4, 11]. The microstructures and properties of thin films depend on the growth condition such as the growth rate, temperature, and vapor pressure [12].

Based on a simple thermodynamics consideration, three different growth modes of thin films are commonly observed [13]. As illustrated in Fig.1.2, they may be described as layer-by-layer growth, layer-by-layer plus island growth, and island growth. When the thin film material has a lower surface energy than the substrate, it wets the substrate surface and grows continuously with a nominally flat film surface to minimize the surface energy; this is the so-called Frank-Van der Merwe (FV) mode [14]. When the film is subjected to a stress (e.g., due to lattice mismatch between the film and the substrate), however, the continuous 2D growth of flat film becomes unstable beyond a critical thickness and a transition to 3D growth of islands occurs, which is the Stranski-Krastanow (SK) mode [15]. On the other hand, if the film material has relatively high surface energy compared to the substrate, the growth process begins with discrete clusters of atoms on the substrate surface, followed by growth and coalescence of islands to form continuous films, and it is called the Volmer-Weber (VW) mode [16].
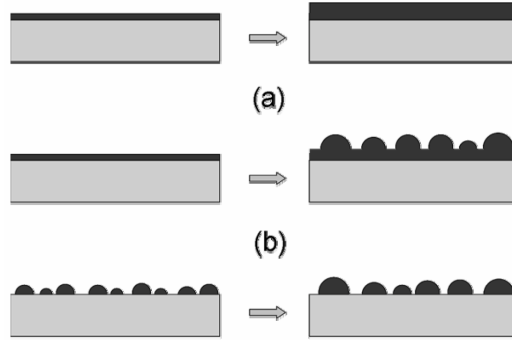
Figure 1.2: Modes of thin-film growth: (a) Frank-Van der Merwe growth mode, (b) Stranski-Krastanow growth mode, (c) Volmer-Weber growth mode.

Practical applications in microelectronic devices often require high-quality, single-crystal semiconductor thin films. The most common technique to produce such films is thin film epitaxy. The word "epitaxy" refers to the extension of the crystal structure of the substrate into the film. An interface between the film and the substrate is considered epitaxial if the atoms of the film material occupy the natural lattice positions of the substrate. Two types of epitaxy can be distinguished [4]. One is *homoepitaxy*, which refers to the cases when the film and the substrate are the same material. The other is *heteroepitaxy*, when the film material is different from the substrate. Examples of thin films grown by heteroepitaxy include Ge or SiGe films on Si and InAs compound films on GaAs. The growth process of these films often follows the SK mode. For applications requiring flat film surfaces, the surface roughening due to the 3D island growth beyond the critical thickness is undesirable and various techniques have been developed to suppress the roughening process. On the other hand, the spontaneous formation of nanoscale 3D islands during the SK growth of heteroepitaxial films has emerged as an at-

tractive approach for synthesis of self-assembled quantum dots (SAQDs) for both microelectronic and optoelectronic applications [17, 18].

1.2.2   Self assembled quantum dots

The potential to grow nanoscale islands by self assembly has attracted much attention since 1990s with an objective to develop novel applications in microelectronics. Early attempts with respect to SK growth of SAQDs were given independently by Mo et al. [19] and Eaglesham et al. [20]. Mo et al. studied the 2D-3D transition during the SK growth of Ge on Si(001) with Scanning Tunneling Microscopy (STM), and observed special faceting along certain directions and alignment. Eaglesham et al. [20] reported formation of dislocation-free SiGe islands on Si(001) and a critical thickness for the island growth. The critical island size for dislocation introduction was also investigated. Later, Cullis et al. [21] performed a comprehensive image contrast analysis of SiGe alloy films on Si, showed that the driving force for surface roughening in thermodynamics terms as the lowering of the overall free energy of the system. More investigations about the strain relaxation and defect formation during the self-assembly process were performed by Hansson et al. [22], Osten et al. [23], Ozkan et al. [24], and Floro et al. [25]. The composition-dependent size of self-assembled islands was first studied by Dorsch et al. [26, 27]. A variation of the layer composition for SiGe alloy was found to play a role in corresponding island scaling. Similar conclusion was given by Floro et al. [28] that the sequence of morphological transitions at low mismatch strain is qualitatively identical to that for high mismatch strain, while the length scale of islands can be significantly different with respect to
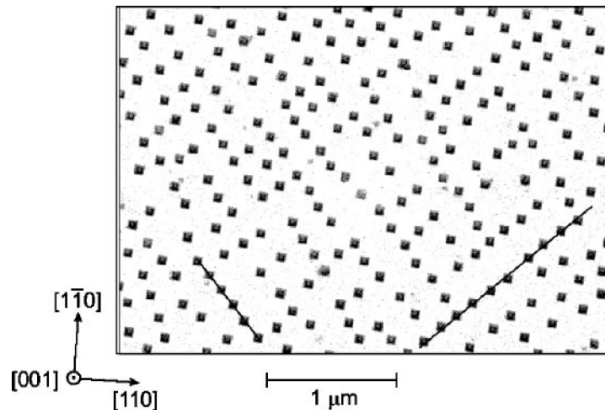
Figure 1.3: Scanning electron micrograph (SEM) of $Si_{0.75}Ge_{0.25}$ island chains along <100> [31].

different misfit. More recently, Berbezier et al. [29] performed a comprehensive investigation of the different growth modes of SiGe alloy films on Si with Ge composition varying from 0 to 1, and presented distinct growth regimes according to different surface orientation.

Recently, tremendous efforts have been devoted to improving the size uniformity and spatial ordering of SAQDs by optimizing growth conditions and using various templates to control strain and surface conditions.

One such approach is to take advantage of the anisotropic material properties in the epitaxial system. Bimberg et al. [30] fabricated InAs quantum dots in GaAs matrix by Molecular Beam Epitaxy (MBE), and observed dot arrays self-organized in rows along <100> directions. By Liquid Phase Epitaxy (LPE) $Si_{1-x}Ge_x$ on Si, Meixner et al. [31] found that the interplay between the kinetics and the anisotropic strain field results in ordered "island chains" along certain directions (Fig.1.3) [31]. Discussions for Ge on other orientation of Si surface were presented by Ohmori et al. [32].

7
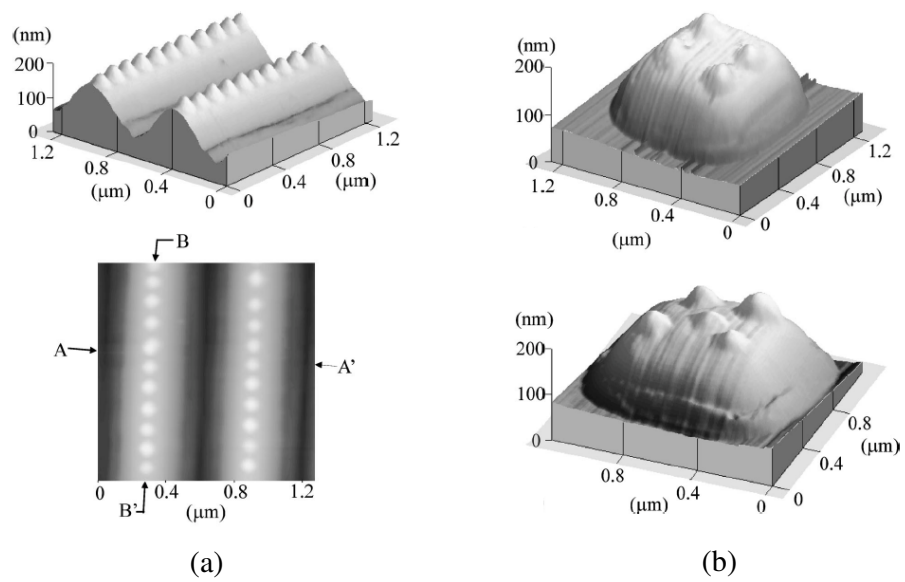
Figure 1.4: (a) 3D and 2D AFM images of the self-assembled Ge islands on the <110> oriented Si stripe with a window width of 0.6μm [33]. (b) AFM images with Ge islands located on a square Si mesa with the base lines parallel to the <110> directions [34].
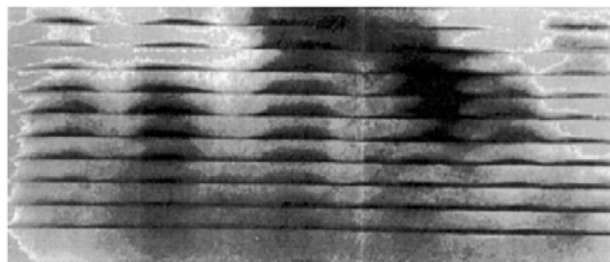
(a)
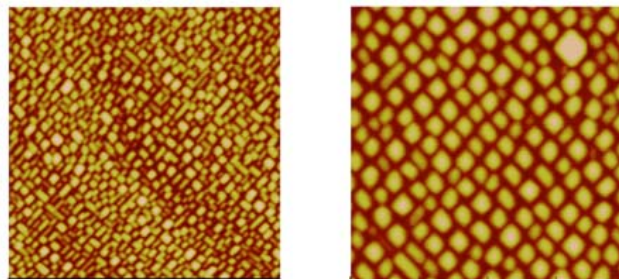
(b)

Figure 1.5: (a) Cross-sectional TEM of a 10 period $Si/Si_{0.5}Ge_{0.5}$ dot multilayer [36]. (b) AFM images of first and 25th layer of a GeSi dot superlattice [37].
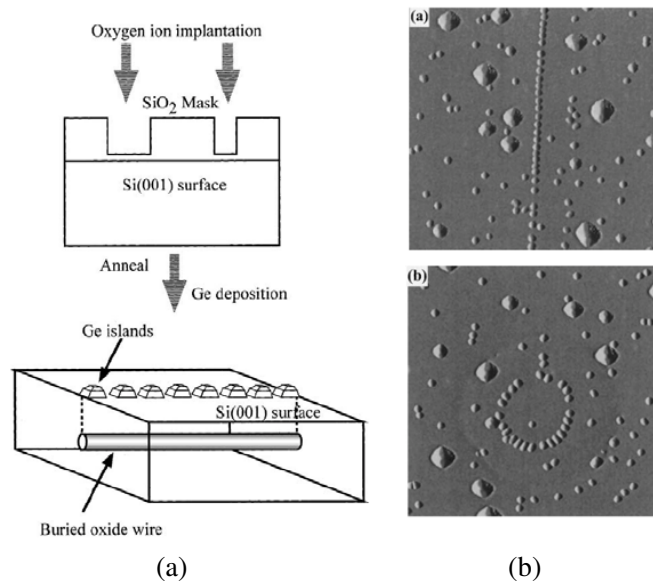
Figure 1.6: (a) Schematic view of a strain-distribution control using buried oxide inclusions. (b) Well-ordered Ge nanostructures on strain-controlled Si(001) surfaces [43].

Increasing effort has been devoted to methods using the substrate as a template for island nucleation and growth (Fig.1.4). Kamins and Williams [33] deposited Ge islands on raised Si stripes on a (001) wafer, and islands nucleated preferentially at the edges were obtained, forming a linear array. Jin et al. [34] investigated the arrangement of Ge islands on lithographically patterned sub-micron mesas, and ordered arrays with uniform size were obtained. Recently, Yang et al. [35] investigated the self-assembly of Ge quantum dots on patterned Si(001) substrate using only simple photolithography and annealing. Ordered 1D quantum dot arrays were also achieved.

Stacked growth of multilayers of islands has also been demonstrated to improve the dots ordering. As investigated by Teichert et al. [36], multiple layers of SiGe islands are continuously grown, separated by Si layers (Fig.1.5). The strain field from each buried layer of islands influences the positioning of islands in the next layer and so on, thereby leading to more uniform spacing in successive layers. A similar method was used by Bauer et al. [37], and ordered patterns were achieved.

Many other techniques are also being used to control the self-assembled patterns, such as growth on miscut substrates with surface steps [38] and on relaxed templates with dislocation networks [39, 40]; adjust the stress fields within the thin film for pattern selection [41]. Artificial design of a non-uniform strain field in the substrate, either by a strained template or embedded quantum dots, offers a better approach to directly control the size and spatial ordering of SAQDs grown, as shown in Fig.1.6 [42–45].

In addition to SAQDs, other different self-assembled nanostructures are being investigated concomitantly. One-dimensional nanowires were first re-

ported by Loretto et al. [46] by growing CaF_2 on Si. Anisotropic surface energy was believed to be the reason for line formation. Following that, extensive work has been done for fabricating self-assembled nanowires by using the benefits of elasticity anisotropy of the substrate [43, 47–52]. More recently, one-dimensional silicide nanowires have gained enough interests, and plenty of efforts are given for both experimental and theoretical investigations [53–59]. Meanwhile, research with respect to other interesting structures such as quantum rings and quantum molecules have never been stopped, which makes self-assembled nanostructures possible to have distinct optic and electronic properties for novel device applications [60–65].

All these experimental works mentioned above have demonstrated the feasibility of achieving tailored nanostructures. However, in spite of enormous experiments, the kinetics and thermodynamics mechanisms underlying the thin film self assembly have not been clearly understood yet. Complementary theoretical investigations of the growth and formation process are therefore required to guide the technology development, which motivates the outset of this thesis.

1.2.3 Modeling approaches

It has been generally understood that a macroscopically flat surface of a stressed solid is thermodynamically unstable. The first theoretical investigation of the morphological instability in a stressed solid was given by Asaro and Tiller [66], and later independently by Grinfeld [67] and Srolovitz [68]. They performed linear stability analyses for a surface bounding a two-dimensional semi-infinite solid under stress-assisted surface diffusion. The general finding

is that planar surfaces are unstable to small disturbances with wavelengths greater than a critical value. Such an instability is driven by the elastic energy associated with the applied stress and was inhibited by the surface energy of the solid. The rate of surface roughening is controlled by associated kinetics of material transport, such as surface diffusion. More recently, several researchers performed nonlinear analyses and showed that the stress-driven surface instability evolves into a deep, crack-like groove or cusp morphology [69–72]. Experimental investigations have observed similar surface instability and morphology evolution in a number of material systems [73, 74].

A thin single-crystal layer on top of another substrate with the same crystalline structure but different lattice spacing is inherently stressed due to mismatch of crystal lattices, thus unstable. For the most common growth mode, SK mode, a transition from two-dimension (2D) growth of a nominally flat film to three-dimensional (3D) growth of islands occurs above a critical mean film thickness. Unlike a semi-infinite homogeneous solid, the presence of the substrate affects the instability in several ways. First, the elastic stiffness of the substrate may differ from that of the film, which leads to a different critical wavelength [75–77]: a stiffer substrate tends to stabilize the film and increases the critical wavelength, while the contrary is true for a softer substrate. At the limit of a rigid substrate, a critical film thickness exists, below which the thin film is stable against perturbations of any wavelengths. However, the stiffness effect is insignificant for cases when the film and the substrate have similar elastic properties, such as a SiGe film on a Si substrate [78]. A more important effect is owing to the interface between the film and the substrate. At close proximity to the interface, the wetting interaction between the film

13

and the substrate becomes significant. If the film wets the substrate, the wetting interaction will prevent the substrate from being exposed. Even when the wetting interaction is weak or the film is non-wetting, in which case the substrate surface may be partly exposed, the surface of the unstressed substrate is stable against further roughening. In both cases, instead of forming deep grooves, the film breaks up into discrete islands [20, 24, 78, 79]. The critical thickness for the 2D-3D transition during SK growth can be predicted by introducing a wetting potential that is in competition with the strain energy and surface energy [80, 81]. Subsequent growth of 3D islands exhibit intriguingly rich dynamics with shape transition and self organization.

Different modeling approaches have been developed to simulate surface pattern evolution and self assembly of quantum dots, such as kinetic Monte Carlo simulations [31, 82, 83], energy minimization methods [84–86], mean-field analyses [87–89], molecular dynamics simulations [90], phase-field modeling [91–94], and surface differential equation approaches [81, 95–98]. In particular, the differential equation approaches have been most popular, possibly owing to the direct connections to surface physics (thermodynamics, kinetics, and mechanics) as well as relatively simple mathematical forms, and yet nontrivial nonlinear solutions.

Despite extensive research with both experimental and modeling progresses, many questions remain open for the growth and evolution dynamics of epitaxial surfaces, regarding the conditions under which ordered surface patterns form as well as the underlying science that controls the size and ordering of self-assembled surface structures (e.g., quantum dots and nanowires) in various epitaxial systems.

1.3 Scope of this dissertation

In this dissertation, a continuum theory based on nonequilibrium thermodynamics is developed for modeling surface evolution and self assembly in epitaxial systems. A nonlinear evolution equation is derived to study the nonlinear effects of the stress field and wetting. Furthermore, the effects of anisotropic mismatch stresses and anisotropic crystal elasticity on pattern evolution are analyzed theoretically, with respect to specific epitaxial systems.

This dissertation is organized as follows. As an introduction, Chapter 1 gives a brief account of the background and motivation for this work. Experimental and theoretical aspects on thin film growth and self assembly are reviewed.

Chapter 2 presents the general formulation of the theoretical model and the technique for numerical simulations. An asymptotic analysis of the nonlinear stress field is presented for generally anisotropic systems. A spectral method is developed for numerical simulations.

In Chapter 3, the nonlinear effects of the stress field and wetting are analyzed. An isotropic system is considered here. Linear analyses and numerical simulations are presented, first without the wetting effect and then with a nonlinear wetting potential.

Chapter 4 presents an analysis of pattern evolution under anisotropic mismatch stresses. Analytical linear analysis and numerical simulations show that the rotational symmetry in the isotropic system is broken, leading to nontrivial anisotropic patterns.

Chapter 5 considers more general anisotropic systems with both stress

and material anisotropy. Two specific epitaxial systems are investigated. First, SiGe films on Si substrates with different crystal orientations are considered. The effects of crystal orientation, Ge concentration, and film thickness on pattern evolution are examined. Second, self-assembled metal silicide nanowires on Si substrates are simulated.

In conclusion, Chapter 6 outlines the theoretical findings from the present study and remarks on potential directions for future work.

Chapter 2

Model Formulation and Solution Methods

The underlying mechanism of the surface evolution and self-assembly process in epitaxial systems has been understood as a result of strain-induced instability, mediated by deposition and diffusion kinetics. In this chapter, general formulation of a theoretical model is developed. For a general anisotropic system, an asymptotic approach is adopted to solve the nonlinear stress field. Then, a spectral method is developed for numerical simulations of the epitaxial surface evolution and self assembly.

2.1 General formulation

Consider a single-crystal thin film on a substrate of another crystal with a similar crystalline structure but different lattice spacing, such as the simple 2D configuration shown in Fig.2.1(a). For a very thin film, the substrate can be

regarded as an infinite half-plane, the lattice mismatch is fully accommodated by an elastic mismatch strain in the film [14] and the effect of substrate is ignored, briefly,

$$\epsilon_m = (a_s - a_f)/a_f, \qquad (2.1)$$

where a_f and a_s are the lattice spacing for the film and the substrate, respectively. In a 3D configuration, the mismatch strain can be isotropic (equi-biaxial) or anisotropic, depending on the epitaxial system. For example, an equi-biaxial mismatch strain is usually obtained for cubic crystal film epitaxy, e.g., SiGe on Si [20, 99]. For hexagonal crystal films on cubic substrates, due to the different lattice spacing in the hexagonal structures, anisotropic mismatch strains are possible [53, 100]. Details of the two systems are discussed later in Chapter 5.

Mechanisms of relaxation of the mismatch strain can be either island formation by mass transport along the surface or accumulation of misfit dislocations within the stressed thin film. The motion of crystal dislocations have been reviewed by Freund [101]. Under appropriate growth conditions, it is possible to compensate the lattice mismatch by distortion of the lattice of the overlayer without formation of misfit dislocations or islands [20, 23]. This growth mode continues only up to a certain critical thickness of the film, which depends on the lattice mismatch and the growth temperature. In the present work, the purpose here is to focus on the strain relaxation by means of mass transport, and self-assembled islands for films beyond the critical thickness are assumed dislocation-free.

A set of right-handed Cartesian coordinate systems (x_1, x_2, x_3) can be
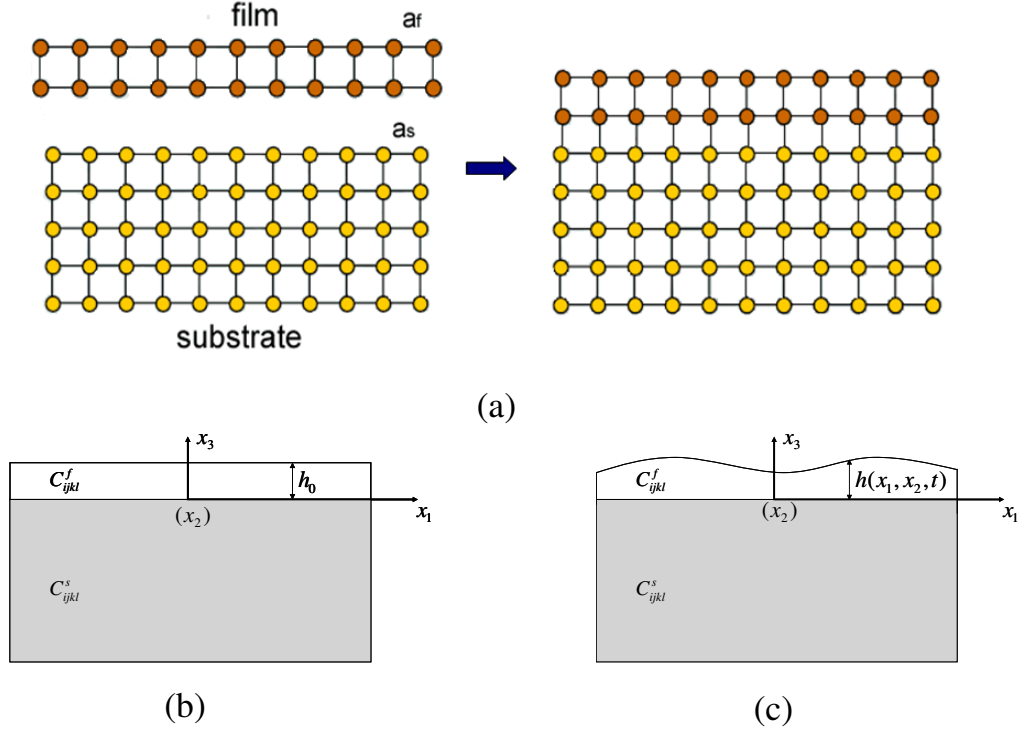
Figure 2.1: A heteroepitaxial thin film structure. (a) schematic of a lattice structure, (b) reference state, (c) evolving state with wavy surface.

attached, with x_3 aligned in the thickness direction and $x_3 = 0$ at the interface between the film and the substrate. At the reference state (Fig.2.1(b)) with flat film surface, the film has a mean thickness h_0, and is unbounded in the x_1 and x_2 directions. The film surface is free of traction and is allowed to undulate by mass transport with respect to time, with an evolving surface profile $h(x_1, x_2, t)$ (Fig.1.2(c)).

The free energy of such an epitaxial system includes contributions from the elastic strain energy and the surface energy. Assuming that the thickness

of the substrate is always much thicker than that of the film, the substrate is taken to be an elastic half-space. The crystal material will tend to alter its overall surface shape in order to change the elastic free energy, as well as the surface free energy, thermodynamically minimizing the total free energy of the system. Simple energetic analyses given by Srolovitz [68] and Mullins [102] demonstrate the nature of this instability: the initial waviness of an arbitrarily small amplitude in the surface shape of a stressed system will tend to increase in amplitude to reduce the strain energy, while the slightly wavy surfaces also tend to become flat in order to minimize the free surface energy. Similar arguments are given by Freund and Jonsdottir [76] and Gao [103].

By definition, the total free energy of the system is evaluated by

$$G = \int_{V_s+V_f} U_E dV + \int_{A_0} \gamma(h)\sqrt{1 + h_\alpha h_\alpha} dA, \qquad (2.2)$$

where U_E is strain energy density within the whole system, and takes the form,

$$U_E = \frac{1}{2}\sigma_{ij}\epsilon_{ij}, (i,j = 1 \sim 3), \qquad (2.3)$$

σ_{ij} and ϵ_{ij} represent the stress and strain in both the film and the substrate, $\gamma(h)$ is the surface energy per unit area of the film surface, and is assumed isotropic here as a function of the film thickness, $h_\alpha = \partial h/\partial x_\alpha (\alpha = 1, 2)$ is the gradient of the surface morphology. V_s and V_f are the volume of the film and the substrate, respectively, and A_0 refers to the projected area of the curved film surface on the (x_1, x_2) plane. A repeated Greek subscript implies summation over its value.

It is important to note that although such a simple form for surface

20

energy in Eq.(2.2) is sufficient for understanding the onset of the surface instability, more complex forms of surface energy accounting for crystal surface anisotropy and surface stress have been developed in order to understand the size and shape of self-assembled islands. Chiu [96] assumed a surface energy as a function of surface normal. The anisotropic surface energy leads to an additional term in the chemical potential. Zhang [104] used an anisotropic surface energy of four-fold symmetry in the (001) plane to simulate shape transition of self-assembled epitaxial islands. Zhang and Bower [105] defined a general form of surface energy that produces shallow and localized minima for specific surface orientations, and their simulations reproduced many observed features in experiments such as island shape transition and surface faceting. A strongly anisotropic surface energy was used by Savina et al. [106], with dependence on both the surface normal and the local mean curvature. In addition to the dependence on surface orientation, the surface energy of a stressed solid also depends on surface deformation through surface stress [107–109]. The effect of surface stress on epitaxial surface instability was investigated by Savina et al. [110], using an isotropic surface energy with an additional surface stress term. Shenoy and Freund [98] derived a general form of surface energy as a function of both surface slope and strain. However, an extension of this form to account for the crystal symmetry within the epitaxial plane for 3D surfaces is not yet available. In general, the application of complex surface energy functions is hindered by the very limited knowledge of the additional parameters from either experiments or first-principle models. For the present study, we take the surface energy to be isotropic and independent of strain, and focus on the effects of anisotropy in the elastic strain energy. It is believed that, while the

21

surface energy anisotropy plays an important role in determining the island shape, the elastic strain energy offers a long-range effect that controls the size and organization of the island array.

Following the approach given by Freund and Jonsdottir [76], variation of the total free energy gives,

$$\delta G = \int_{V_s+V_f} \delta U_E dV + \int U_E \delta V + \int_{A_f} \delta \gamma dA + \int \gamma \delta A_f. \qquad (2.4)$$

For a system in mechanical equilibrium with no external work done,

$$\int_{V_s+V_f} \delta U_E dV = 0. \qquad (2.5)$$

Consider a wavy surface with variational thickness h,

$$\delta V = \int_{A_0} \delta h dA, \qquad (2.6)$$

and

$$\delta A_f = \int_{A_0} \delta(\sqrt{1+h_\alpha h_\alpha}) dA. \qquad (2.7)$$

Variation of the surface energy gives

$$\delta \gamma(h) = \frac{d\gamma}{dh} \delta h. \qquad (2.8)$$

Then, rewriting the variation form of the total free energy leads to

$$\delta G = \int_{A_0} \left[U_E - \gamma \kappa + \frac{d\gamma}{dh} \frac{1}{\sqrt{1+h_\alpha h_\alpha}} \right] \delta h dA. \qquad (2.9)$$

Here κ takes the form

$$\kappa = \frac{(1 + h_\alpha h_\alpha)h_{\beta\beta} - h_\alpha h_\beta h_{\alpha\beta}}{(1 + h_\alpha h_\alpha)^{3/2}}, \tag{2.10}$$

and is the local mean curvature of the surface. The sign of κ is defined such that it is positive for a concave surface and negative otherwise.

Consider the thickness change can be interpreted as the atomic volume of the material, say, Ω, times the number of atoms q, being added to per unit area of the film surface, then

$$\delta h = \Omega \delta q. \tag{2.11}$$

Thus the chemical potential for the mass transport process along the curvy film surface can be defined as,

$$\mu(x_1, x_2, t) = \Omega \left[U_E - \gamma\kappa + \frac{d\gamma}{dh} \frac{1}{\sqrt{1 + h_\alpha h_\alpha}} \right]. \tag{2.12}$$

The strain energy density U_E is evaluated by Eq.(2.3). The second term in Eq.(2.12) is due to surface energy,

$$U_S = -\gamma\kappa. \tag{2.13}$$

which is simply a product of the surface energy density (or surface tension) and the local mean curvature of the surface.

Besides strain and surface energy terms, the third term in Eq.(2.12) represents the interaction between the film surface and the film/substrate interface as the local film thickness varies, which may be termed as the wetting

potential,

$$U_W = \frac{d\gamma}{dh} \frac{1}{\sqrt{1 + h_\alpha h_\alpha}}. \tag{2.14}$$

The characteristic 2D-3D transition of SK growth along with the presence of a thin wetting layer underlying self-assembled islands at the later stage suggests that a critical thickness exists, below which the flat film surface is stabilized. Different physical origins and modeling approaches of the critical thickness have been proposed. Kukta and Freund [111] suggested a regularization of the film/substrate interface by assuming a thin transition layer with a continuous variation in the mismatch strain. The same idea was adopted by Zhang and Bower [97] and their subsequent works, assuming a linear variation of the strain in the transition layer. Alternatively, a transition layer of surface energy density may be assumed [80, 112–114], which postulates a gradual variation of the surface energy density from substrate to film, as illustrated in Fig.2.2. This model specifies a surface energy that depends on the film thickness and undergoes a rapid transition from γ_f (film) to γ_s (substrate) over a length scale b. The curved line in the figure represents the variation behavior across the interface and through a smooth transition over the region b. Out of the transition region, the surface energy is γ_f if the film has relatively high thickness and is γ_s if the substrate is exposed. To promote a wetting layer along the interface, $\gamma_f < \gamma_s$ is required.

Following this transition idea, a proper mathematical expression is given by Spencer [114], described as

$$\gamma(h) = \frac{1}{2}(\gamma_f + \gamma_s) + \frac{1}{\pi}(\gamma_f - \gamma_s)\arctan(\frac{h}{b}) \tag{2.15}$$
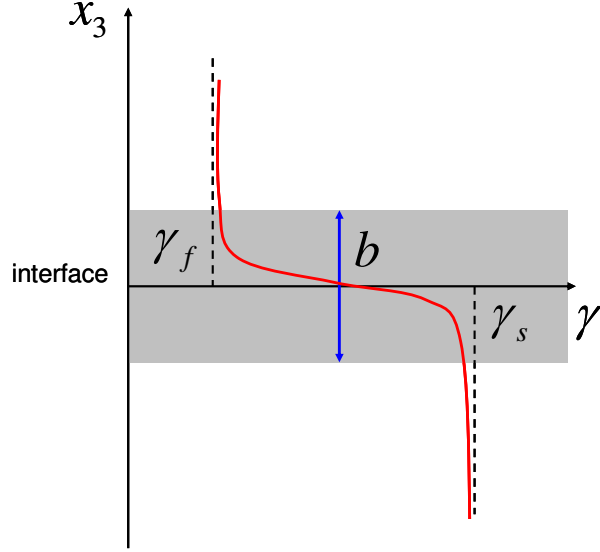
Figure 2.2: Schematic of surface energy model across the film/substrate interface.

This function offers the properties that $\gamma(h) \to \gamma_s$ with $h \to -\infty$, and $\gamma(h) \to \gamma_f$ when $h \to +\infty$, which recovers the surface energy properties above and below the interface, and for the present work, it is adopted as the surface energy which leads to a nonlinear wetting potential as follows,

$$U_W = \frac{\gamma_f - \gamma_s}{\sqrt{1 + h_\alpha h_\alpha}} \frac{b}{\pi(b^2 + h^2)}. \tag{2.16}$$

Different functional forms of the wetting potential have also been obtained by considering physical interactions between the film and the substrate, such as quantum confinement and van der Waals interactions [96, 105, 115]. A general discussion on the effect of the wetting potential on surface instability and pattern evolution dynamics was presented by Golovin et al. [116]. In

principle, the wetting potential can be anisotropic, for example, as a result of the transition of anisotropic surface energy. This however is not considered in the present study, to be consistent with the assumption of isotropic surface energy.

Under the circumstance of high temperature $(500^{o}C)$ and large mismatch stress (1GPa), the material tends to change its surface shape by mass transport, principally through the surface diffusion. The surface chemical potential, if non-uniform, drives the surface diffusion process. A linear kinetic law has been proposed, where the diffusion flux is proportional to the gradient of the chemical potential, namely

$$J_\alpha = -M_{\alpha\beta} \frac{\partial}{\partial x_\beta} (\mu \sqrt{1 + h_\chi h_\chi}), \qquad (2.17)$$

where $M_{\alpha\beta}$ represents a generally anisotropic surface mobility. Note that, in Eq.(2.17), the chemical potential is projected onto a plane parallel to the film/substrate interface before taking the gradient with respect to the in-plane coordinates. Assuming isotropic surface diffusion, we have $M_{\alpha\beta} = M_0 \delta_{\alpha\beta}$, where M_0 is a constant and $\delta_{\alpha\beta}$ is the Kronecker delta.

Conservation of mass at each point along the surface requires that the normal velocity is proportional to the divergence of the local surface flux [102],

$$\frac{\partial h}{\partial t} = -\Omega \nabla \cdot \mathbf{J} \qquad (2.18)$$

Combination of (2.12), (2.17) and (2.18) leads to the change of the local thick-

ness, namely

$$\frac{\partial h}{\partial t} = \Omega^2 M_{\alpha\beta} \frac{\partial^2}{\partial x_\alpha \partial x_\beta} [(U_E + U_S + U_W)\sqrt{1 + h_\chi h_\chi}]. \qquad (2.19)$$

This is a typical diffusion equation valid for any nonlinear, anisotropic situations. A flux term may be included to simulate growth during deposition, but often ignored for surface evolution upon annealing. The elastic strain energy density at the surface is to be determined by solving an anisotropic boundary value problem (details will be given in the next section). Further complication of the differential evolution equation may involve the kinetics. Considerations of anisotropic surface diffusion [117] and nonlinear kinetics [118] may reveal more interesting surface dynamics. In addition, coupling of surface and volume diffusion may also be important in some cases [119]. These issues will be left for future study.

2.2 Nonlinear, anisotropic stress field

Suppose that the half-space thin film/substrate system is not subjected to externally applied surface traction. The traction free boundary condition at the film surface ($x_3 = h$) is generically imposed and self-satisfied by

$$\sigma_{ij} n_j = 0 \qquad (2.20)$$

with a unit vector of the surface normal given by

$$n_\alpha = \frac{-h_\alpha}{\sqrt{1 + h_\beta h_\beta}}, n_3 = \frac{1}{\sqrt{1 + h_\beta h_\beta}}. \qquad (2.21)$$

For a perfectly flat surface, which refers to the reference state, the normal vector takes the form,

$$\mathbf{n} = \{0, 0, 1\}, \tag{2.22}$$

and above traction free boundary condition yields the vanish of out-of-plane stress components, say,

$$\sigma_{i3}^{(0)} = 0. (i = 1 \sim 3) \tag{2.23}$$

The reference state stress fields are uniform in the film, with in-plane components, $\sigma_{11}^{(0)}$, $\sigma_{12}^{(0)}$ and $\sigma_{22}^{(0)}$ only. For a given in-plane mismatch strain state, $\epsilon_{\alpha\beta}^{(0)}$, the stress and strain fields in the epitaxial thin film is connected by the generalized Hooke's law,

$$\sigma_{ij}^{(0)} = C_{ijkl}^f \epsilon_{kl}^{(0)}, \tag{2.24}$$

where C_{ijkl}^f represents the elastic constants for the film. Thus, a solvable determinant equation system is presented, with 6 unknowns $\sigma_{\alpha\beta}^{(0)}$, and $\epsilon_{3i}^{(0)}$. Eq.(2.23) decouples the stress and strain terms, and makes it possible to solve strain and stress separately.

In specific, the three unknown strain components are calculated first,

$$\begin{pmatrix} \epsilon_{33}^{(0)} \\ \epsilon_{23}^{(0)} \\ \epsilon_{31}^{(0)} \end{pmatrix} = -A_2^{-1} A_1 \begin{pmatrix} \epsilon_{11}^{(0)} \\ \epsilon_{22}^{(0)} \\ \epsilon_{12}^{(0)} \end{pmatrix}, \tag{2.25}$$

where

$$A_1 = \begin{bmatrix} C_{31} & C_{32} & C_{36} \\ C_{41} & C_{42} & C_{46} \\ C_{51} & C_{52} & C_{56} \end{bmatrix}, \tag{2.26}$$

and

$$A_2 = \begin{bmatrix} C_{33} & C_{34} & C_{35} \\ C_{43} & C_{44} & C_{45} \\ C_{53} & C_{54} & C_{55} \end{bmatrix}. \tag{2.27}$$

It is worth mention that the existence of nonzero out-of-plane shear strains is depending on the characteristics of compliance matrix: for cubic crystalline films epitaxy on certain orientated surfaces, such as (001), (110), and (111), Eq.(2.25) gives zero shear strains, while for cubic films on particular surface such as (113), nonzero shear strain components are obtained, which indicates the existence of out-of-plane shear deformation induced by in-plane epitaxial mismatch strains in the film.

After the strain components are obtained by Eq.(2.25) the unknown stress components are in turn calculated by Eq.(2.24). Corresponding strain energy density at the reference state is simply calculated by

$$U_E^{(0)} = \frac{1}{2}\sigma_{\alpha\beta}^{(0)}\epsilon_{\alpha\beta}^{(0)}. \tag{2.28}$$

When the surface starts to evolve, general forms Eq.(2.21) sustain for

unit vector, and the value keep changing along with the undulation of surface. The nonlinearity in Eq.(2.21) is raised with respect to the moving boundary. Corresponding stress and strain components in the film need to be evaluated by solving a half-plane boundary value problem subjected to the action of surface traction. This can be clearly interpreted by a superposition procedure [103]. The interface between the film and the substrate ($x_3 = 0$) remains coherent, implying continuity for tractions and displacements. The substrate is assumed to be infinitely thick with both the stress and the displacement diminishing as $x_3 \rightarrow -\infty$. Due to the nonlinearity in the boundary condition (2.20), the elasticity problem in general must be solved numerically, which is computationally expensive in 3D. An alternative approach will be introduced next.

Following an asymptotic analysis by Xiang and E [72], we expand the stress field into a series in the order of the surface gradient, namely,

$$\sigma_{ij} = \sigma_{ij}^{(0)} + \sigma_{ij}^{(1)} + \sigma_{ij}^{(2)} + \cdots , \qquad (2.29)$$

where $\sigma_{ij}^{(0)}$ is the mismatch stress at the reference state, $\sigma_{ij}^{(1)}$ represents a linear perturbation to the reference stress field. The third term, $\sigma_{ij}^{(2)}$, is to the second order of the magnitude of the surface gradient, as the leading nonlinear term (second-order perturbation) of the stress field. In principle, successively higher order terms can be included.

By substituting series (2.29) into the boundary condition (2.20) and

keeping only the first-order terms, we obtain,

$$-\sigma_{i\alpha}^{(0)}h_\alpha + \sigma_{i3}^{(1)} = 0. \qquad (2.30)$$

Since only in-plane components exist for zeroth-order stresses, a boundary condition for the first-order stresses is derived from Eq.(2.30):

$$\sigma_{3\alpha}^{(1)} = \sigma_{\alpha\beta}^{(0)}h_\beta, \sigma_{33}^{(1)} = 0. \qquad (2.31)$$

Similarly, for the second-order stresses, we still put Eq.(2.29) into the boundary condition and keep up to second-order terms,

$$-\sigma_{i\alpha}^{(1)}h_\alpha + \sigma_{i3}^{(2)} = 0. \qquad (2.32)$$

With the help of Eq.(2.31), nonlinear boundary conditions take the form

$$\sigma_{3\alpha}^{(2)} = \sigma_{\alpha\beta}^{(1)}h_\beta, \sigma_{33}^{(2)} = \sigma_{\alpha\beta}^{(0)}h_\alpha h_\beta. \qquad (2.33)$$

Both linear and nonlinear boundary conditions should be applied at the film surface, i.e., $x_3 = h(x_1, x_2, t)$. A couple of approximations may be used to solve such boundary value problems. First, for a film surface with relatively slow variation of its thickness along the in-plane directions, the undulated surface may be approximated by a flat surface with the average film thickness ($x_3 = h_0$). As will be shown later from simulations, the surface pattern usually has a characteristic length (e.g., wavelength for periodic patterns) much larger than the amplitude of its thickness undulation. From experimen-

tal observations, the diameter of self-assembled quantum dots is typically 1-2 orders of magnitude greater than the height [24, 42, 120, 121]. The second approximation is to take the film-substrate problem as a semi-infinite homogeneous half-space problem. This is a reasonable approximation when the elastic moduli for the film and the substrate are similar, such as SiGe films on Si substrate [76, 78]. It has also been shown that, at the limit of very thin films, the surface displacement at the film surface is predominantly controlled by the substrate elasticity [77]. Therefore, in the following, the surface displacements corresponding to the linear and nonlinear stress fields are approximately determined by solving the half-space problem with boundary conditions (2.31) and (2.33). By this approach, the effect of substrate elasticity is taken into account in the calculation of the surface displacement, while the elastic moduli of the film are used in calculating the mismatch stresses (i.e., $\sigma_{\alpha\beta}^{(0)}$). As a result, the effect of anisotropy is decomposed into two origins, one due to the mismatch stress as related to the elastic anisotropy of the film and the other due to the substrate. The generally anisotropic, linear elastic half-space problem is solved by a Fourier transform method as detailed in Appendix A. The solution gives a relationship between the surface traction and the surface displacement in the Fourier space, namely

$$\hat{u}_i^{(n)}(k_1, k_2) = Q_{ij}(k_1, k_2)\hat{\sigma}_{3j}^{(n)}. \tag{2.34}$$

where k_1, k_2 are the coordinates in the Fourier space (i.e., components of the wave vector), Q_{ij} is a compliance matrix that depends on the elastic moduli of the substrate, and $n = 1, 2$ for the first and second-order solutions, respectively.

In accordance with the series expansion of the stress field in (2.29), the strain energy density at the film surface can be written in form of a series as well:

$$U_E = U_E^{(0)} + U_E^{(1)} + U_E^{(2)} + \cdots . \tag{2.35}$$

$U_E^{(0)}$ is given in Eq.(2.28), and, by using the symmetry property of stiffness matrix, other order strain energy terms are derived accordingly,

$$U_E^{(1)} = \sigma_{\alpha\beta}^{(0)} \frac{\partial u_\alpha^{(1)}}{\partial x_\beta}, \tag{2.36}$$

$$U_E^{(2)} = \sigma_{\alpha\beta}^{(0)} \frac{\partial u_\alpha^{(2)}}{\partial x_\beta} + \frac{1}{2} \sigma_{\alpha\beta}^{(1)} \frac{\partial u_\alpha^{(1)}}{\partial x_\beta} + \frac{1}{2} \sigma_{\alpha\beta}^{(0)} h_\beta \left(\frac{\partial u_3^{(1)}}{\partial x_\alpha} + \frac{\partial u_\alpha^{(1)}}{\partial x_3} \right). \tag{2.37}$$

The term $U_E^{(1)}$ is the strain energy density to the first order of surface perturbation and $U_E^{(2)}$ is to the second order of surface perturbation, which is the leading nonlinear term. The higher order terms are truncated for the present study.

2.3 Spectral method for numerical simulations

In this dissertation, the evolution problem is formulated and governing diffusion equation is integrated numerically by a spectral method. All simulations are implemented and performed by commercial software MATLAB®. This section is intended to give an introduction to spectral methods and corresponding implementations in MATLAB.

Spectral method is a nice technology for solving ordinary differential equations (ODEs) and partial differential equations (PDEs). The fundamental

principle of spectral method is: given discrete data on a grid, interpolate the data globally, and evaluate the derivative of the interpolant on the grid. This approach offers a solution with higher accuracy for ODEs or PDEs defined smoothly on a simple domain.

Depending on specific type of differential equations, the geometry of spatial domains, and specific boundary conditions, different spectral schemes have been developed [122]. For our present problem with unbounded domain, the evolution process is unrelated to boundaries, and periodic boundary condition seems to be appropriate to use. In this dissertation, the spectral method using Fourier series is employed in our simulation. Other approaches can be found from general resources of numerical methods [123].

Fourier spectral method is processed by doing Fourier transform to the objects and performing the calculation in Fourier space. After that, functions are transformed back to the original space by taking the inverse Fourier transform. This process is then iterated for each time step of the algorithm. Specifically, the procedure for using Fourier spectral method to solve differential equations in a discrete simulation domain:

Step 1. For a given function $f(x)$, calculate the $\hat{f}(k)$ by using Discrete Fourier Transform (DFT) in physical space.

Step 2. Evaluate $\hat{f}'_x$ by $\hat{f}'_x = ik\hat{f}(k)$ in Fourier space.

Step 3. Obtain the spectral differentiation $f'(x)$ by applying inverse DFT, giving the value in physical space again.

The computation of the DFT and inverse DFT can be accomplished by the Fast Fourier Transform (FFT) and inverse Fast Fourier Transform (IFFT), respectively. FFT is the technique for performing discrete Fourier transform

in a computationally efficient way. Details can be found in many references [124–127]. In MATLAB, the operations are performed by built-in functions **fft** and **ifft**.

Now we look at the problem being described by a general nonlinear PDE:

$$\frac{\partial h}{\partial t} = L(h) + N(h), \tag{2.38}$$

where L and N are linear and nonlinear operators, respectively. Fourier transform of Eq.(2.38) gives

$$\frac{\partial \hat{h}}{\partial t} = \alpha(k) \cdot \hat{h} + \phi(\hat{h}), \tag{2.39}$$

where $\alpha(k)$ is the coefficient from the linear term, which is a function of the wave vector k in Fourier space, and $\phi(\hat{h})$ is the nonlinear term, in terms of the Fourier transformed thickness $\hat{h}$.

Eq.(2.39) can be integrated by a semi-implicit method in Fourier space: the backward finite difference scheme is used for the linear part, and the forward finite difference scheme is used for the nonlinear part, namely,

$$\frac{\hat{h}^{(n+1)} - \hat{h}^{(n)}}{\Delta t} = \alpha(k) \cdot \hat{h}^{(n+1)} + \phi(\hat{h}^{(n)}). \tag{2.40}$$

Solving for $\hat{h}^{(n+1)}$ leads to

$$\hat{h}^{(n+1)} = \frac{\hat{h}^{(n)} + \phi(\hat{h}^{(n)})\Delta t}{1 - \alpha(k)\Delta t}. \tag{2.41}$$

It is important to note that the scheme is not unconditionally stable. There exists a maximum Δt, which is determined by both linear and nonlinear terms [127].

Figure 2.3 illustrates the flow chart for the integration of Eq.(2.41). By communicating between the physical and Fourier spaces back and forth, linear and nonlinear terms are calculated separately, and the surface profile h can be traced at each time step by circling the loop.
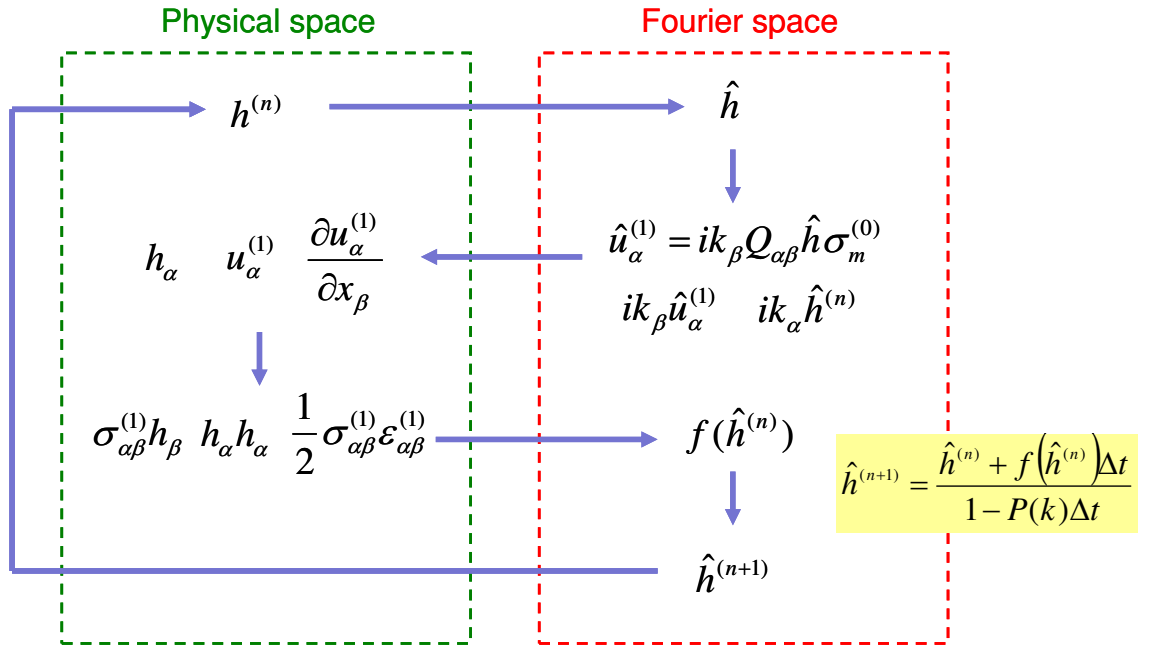
Figure 2.3: Flow chart for the numerical integration of surface profile.

Chapter 3

Nonlinear Effect of Stress and Wetting

Early investigations for a stressed solid by performing only the linear analyses energetically revealed the reason for surface instability. Followed nonlinear analyses, however, obtained a deep, crack-like groove or cusp morphology, which has been supported by experiments observations. Different from the stresses solid, for a thin film/substrate epitaxial system, the effect of wetting energy attributed from the interface can even play an important role in surface evolution and can not be ignored.

In this chapter, we will focus on the nonlinear effect in isotropic systems. With the general formulation developed in Chapter 2, we solve the boundary value problems for the first- and second-order stress fields, and analyze the nonlinear effects of stress and wetting. The effects of anisotropy will be discussed in subsequent chapters.

3.1 First-order solution: linear analysis

At the present study, an isotropic system is defined as both the surface properties (surface energy) and the bulk properties (elastic moduli for film and substrate) are isotropic, and the epitaxial growth offers an equi-biaxial in-plane mismatch strain,

$$\epsilon_{\alpha\beta}^{(0)} = \epsilon_m \delta_{\alpha\beta}. \tag{3.1}$$

For an isotropic system, at the reference state, an equi-biaxial stress state is induced by the mismatch strain,

$$\sigma_{\alpha\beta}^{(0)} = \sigma_m \delta_{\alpha\beta}, \tag{3.2}$$

and corresponding zeroth-order strain energy density is,

$$U_E^{(0)} = \frac{1 - \nu_f}{E_f} \sigma_m^2, \tag{3.3}$$

where E_f is Young's modulus of the film and ν_f is Poisson's ratio. The reference state is an unstable equilibrium configuration because certain small perturbations can grow. The boundary condition for the first-order stress field, for isotropic system, can be simplified from Eq.(2.31),

$$\sigma_{3\alpha}^{(1)} = \sigma_m h_\alpha, \sigma_{33}^{(1)} = 0. \tag{3.4}$$

For a semi-infinite solid subjected to surface tractions, the displacement at the same surface can be evaluated analytically in the Fourier space (Appendix A). From the solution to the classical Cerruti's problem in linear

38

elasticity, a simple form of the surface displacement with respect to first-order traction boundary is obtained in terms of Fourier transforms:

$$\hat{u}_\alpha^{(1)} = ik_\beta Q_{\alpha\beta} \sigma_m \hat{h}, \qquad (3.5)$$

where $\hat{u}_\alpha^{(1)}$ and $\hat{h}$ are the Fourier transforms of the surface displacement and the thickness profile, respectively, $Q_{\alpha\beta}$ is the compliance matrix of the substrate given by (A.19), and k_β is the component of the wave vector in the Fourier space. The thin-film approximation effectively takes into account the elastic properties of the substrate, while the mismatch stress σ_m depends on the elastic properties of the film. Consequently, different elastic properties can be accommodated. Equation (3.5) is exact if the film and the substrate have identical elastic properties, thus can also be used as a reasonable approximation for cases with elastically similar film and substrate materials.

Corresponding to the surface displacement in Eq.(3.5), the first-order elastic strain energy density at the surface is

$$U_E^{(1)} = \sigma_m \frac{\partial u_\alpha^{(1)}}{\partial x_\alpha}. \qquad (3.6)$$

The surface curvature as given in Eq.(2.10) can be expanded as

$$\kappa = h_{\alpha\alpha}(1 - \frac{1}{2}\delta^2) - h_{\alpha\beta}h_\alpha h_\beta + O(\delta^4), \qquad (3.7)$$

where $\delta = \sqrt{h_\alpha h_\alpha}$ is the magnitude of the surface gradient vector. In the present study, only the linear term ($\kappa = h_{\alpha\alpha}$) is used for the first and second-order analyses, because the first nonlinear term in Eq.(3.7) is of the third

order.

The surface energy $\gamma(h)$ can be expanded with respect to reference thickness ,

$$\gamma(h) = \gamma(h_0) + \gamma'(h_0)\delta h + \cdots . \tag{3.8}$$

Truncate higher order terms, we can take first term $\gamma(h_0)$ for linear analysis, and it can be reasonably approximated by constant film surface tension γ_f for very thin transition layer thickness.

To investigate the nonlinear stress effects, the wetting energy is not considered at this part. By keeping the first-order terms only in Eq.(2.19), we obtain a linearized evolution equation

$$\frac{\partial h}{\partial t} = \Omega^2 M \frac{\partial^2}{\partial x_\beta \partial x_\beta}(\sigma_m \frac{\partial u_\alpha^{(1)}}{\partial x_\alpha} - \gamma_f h_{\alpha\alpha}). \tag{3.9}$$

Fourier transform of Eq.(3.9) leads to the linear equation in the Fourier space,

$$\frac{\partial \hat{h}}{\partial t} = \Omega^2 M k^2 (\frac{2\sigma_m^2}{\overline{E}_s}k - \gamma_f k^2)\hat{h}. \tag{3.10}$$

where $\overline{E}_s = E_s/(1 - \nu_s^2)$ is the plane-strain modulus of the substrate and $k^2 = k_1^2 + k_2^2$.

The two terms in the bracket of Eq.(3.10) compete with each other: to relax the total free energy, the first term, strain energy, drives surface instability, while the second term, surface energy, stabilizes the surface to minimize the surface area. The competition sets up a length scale and an

associated time scale, namely,

$$L = \frac{\gamma_f \overline{E}_s}{2\sigma_m^2}, \tag{3.11}$$

$$\tau = \frac{L^4}{\Omega^2 M \gamma_f} = \frac{\gamma_f^3 \overline{E}_s^4}{16\Omega^2 M \sigma_m^8}. \tag{3.12}$$

Eq.(3.10) takes the form of an ordinary differential equation (ODE). For a constant wave number k, the solution to Eq.(3.10) is simply

$$\hat{h}(k,t) = A \exp(\frac{st}{\tau}), \tag{3.13}$$

where s is the normalized growth rate,

$$s = (kL)^3(1 - kL), \tag{3.14}$$

and A is the initial amplitude.

A critical wavelength ($\lambda_c = 2\pi L$) and the fastest growing mode ($\lambda_m = \frac{8}{3}\pi L$) can be determined according to Eq.(3.14). This result agrees with previous studies by linear perturbation analysis [75, 77]. To simulate surface evolution with an arbitrary initial perturbation, the spectral method is employed for numerical simulations. At each step, the current thickness profile is transformed into the Fourier space by Fast Fourier Transform (FFT). The evolution equation (3.10) is integrated by a backward Euler scheme of finite difference:

$$\hat{h}^{(n+1)} = \frac{\hat{h}^{(n)}}{1 - s\Delta t}, \tag{3.15}$$

where δt is the time step, normalized by the time scale in (3.12). The new profile can then be obtained by an inverse FFT, assuming periodic boundary conditions in the plane of the film. Same procedure can be applied for both 2D and 3D configurations. Notably, normalization with the length L and the time τ leads to a generic equation with no system-specific parameters. Consequently, numerical simulations can be performed without specifying any particular material properties; the result is general for all isotropic systems in the linear regime, with the system dependence implicitly accounted for by the definitions of the length and time scales.
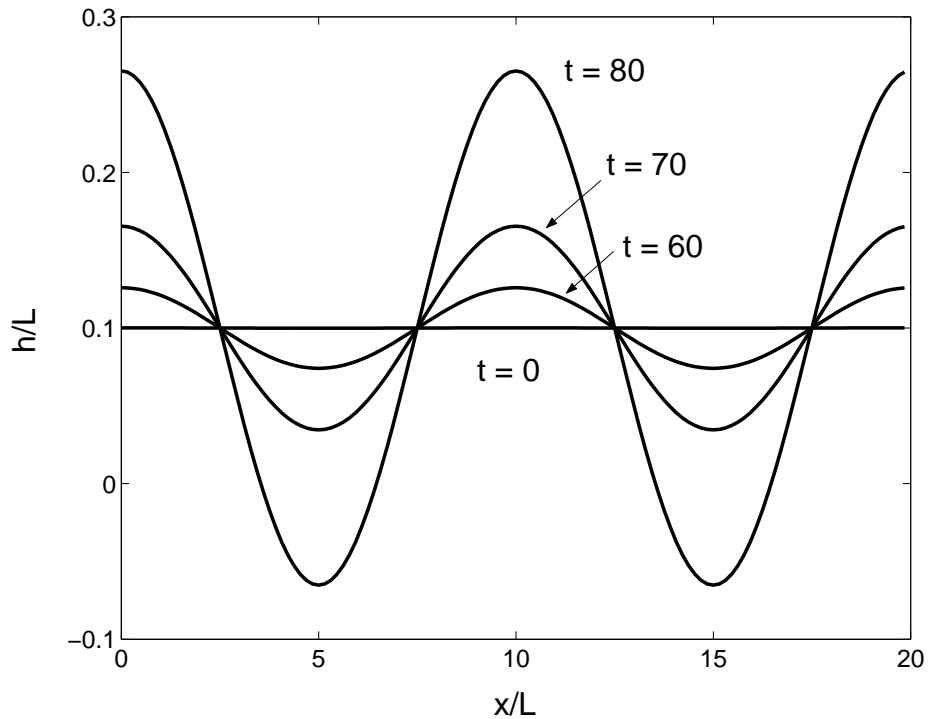
Figure 3.1: Two-dimensional simulation of surface evolution based on the linear analysis.

The result from a 2D simulation is shown in Fig.3.1, where the film thickness varies in one direction only. A film stripe of $20L$ width is considered, whose surface is discretized into 128 grid points. The simulation starts from a sinusoidal perturbation with a wavelength $10L$ (close to the fastest growing mode) and a small amplitude ($10^{-4}L$), using the normalized time step $\Delta t = 0.1$. As the amplitude of the perturbation grows, the surface profile remains sinusoidal, as expected from the linear perturbation analysis. Figure 3.2 shows the result from a 3D simulation, with a square computational cell of size $100L$ by $100L$, starting from a random initial perturbation (Fig.3.2(a)). The computational cell is discretized into a 128 by 128 grid, and the normalized time step is again 0.1. Refining the computational grid and the time step leads to no difference in the simulation results. As shown in Fig.3.2 (b)-(e), the surface pattern quickly selects a characteristic length. Subsequently, the overall pattern remains unchanged, while the surface roughness grows. Therefore, using the first-order evolution equation, the film surface evolves self-similarly in both 2D and 3D configurations. The Fourier spectrum of the surface pattern (Fig.3.2(f)) exhibits a circular ring of the peak intensity at the radius corresponding to the wave number of the fastest growing mode, $2\pi L/\lambda_m = 0.75$. The randomly oriented labyrinth-type surface pattern is a common feature for isotropic systems, similar to the domain patterns of modulated phases in a variety of physical-chemical systems [128] and the wrinkling patterns of thin films [129, 130].
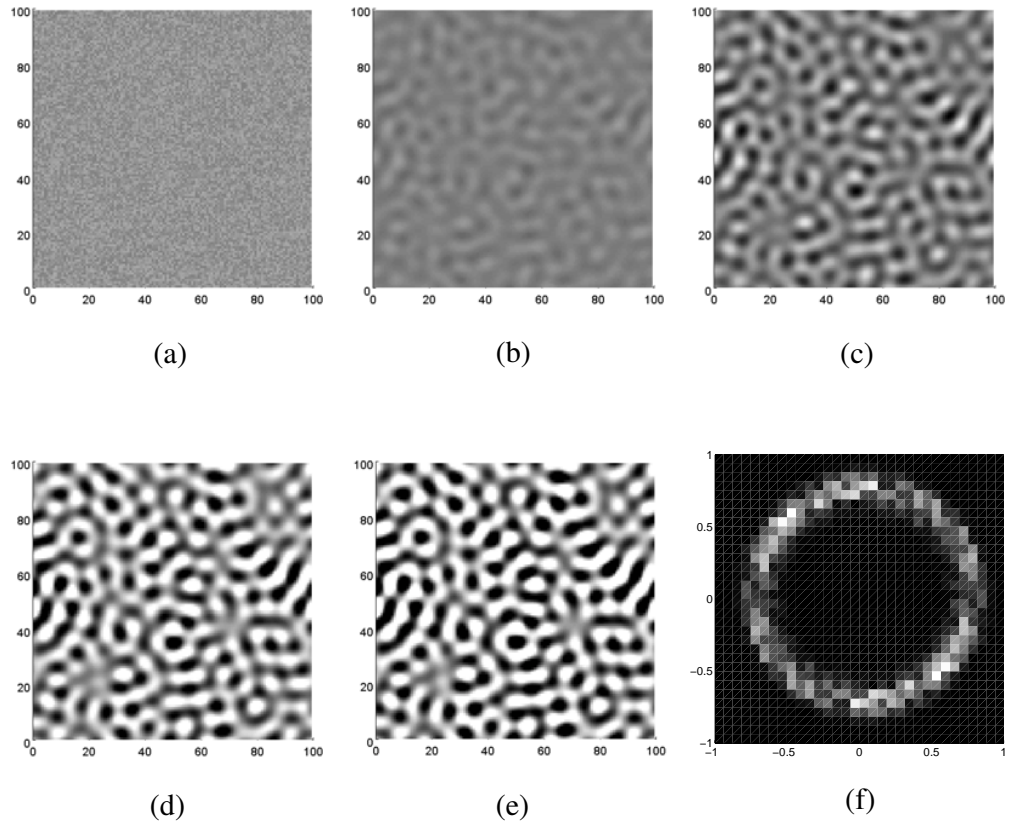
Figure 3.2: Three-dimensional simulation of surface evolution based on the linear analysis. (a)-(e) are gray scale contour plots of the thickness profile, $h(x_1, x_2)$, white for crests and dark for troughs; (a) random perturbation at t = 0, RMS = 5.77×10-5; (b) t = 20, RMS = 7.40×10-5; (c) t = 50, RMS = 1.64×10-3; (d) t = 75, RMS = 2.39×10-2; (e) t = 100, RMS = 3.60×10-1; (f) The Fourier spectrum of the surface pattern, which remains the same for (b)-(e).

3.2   Nonlinear effect of stress

Following the same procedure as in the previous section, the second-order terms in the nonlinear boundary condition (2.33) lead to

$$\sigma_{3\alpha}^{(2)} = \sigma_{\alpha\beta}^{(1)} h_\beta, \sigma_{33}^{(2)} = \sigma_m h_\beta h_\beta. \tag{3.16}$$

Here both shear and normal tractions are in action for the second-order field. Under the thin-film approximation as described earlier, the Fourier transform of the second-order surface displacement is

$$\hat{u}_\alpha^{(2)} = Q_{\alpha\beta} \hat{\varphi}_\alpha + Q_{\alpha3} \sigma_m \hat{\phi}, \tag{3.17}$$

where $\varphi_\alpha = \sigma_{\alpha\beta}^{(1)} h_\beta$, $\phi = h_\beta h_\beta$. The corresponding second-order strain energy density at the surface is

$$U_E^{(2)} = \frac{1}{2} \sigma_{ij}^{(1)} \epsilon_{ij}^{(1)} + \sigma_m \frac{\partial u_\alpha^{(2)}}{\partial x_\alpha}. \tag{3.18}$$

Noting Eq.(3.4) for the first-order surface tractions, the first term at the right hand side of Eq.(3.18) can be written as

$$\frac{1}{2} \sigma_{ij}^{(1)} \epsilon_{ij}^{(1)} = \frac{1 + \nu_f}{1 - \nu_f} U_E^{(0)} \phi + \psi \tag{3.19}$$

where $\psi = \frac{1}{2} \sigma_{\alpha\beta}^{(1)} \epsilon_{\alpha\beta}^{(1)}$ and

$$\epsilon_{\alpha\beta}^{(1)} = \frac{1}{2} \left[\frac{\partial u_\alpha^{(1)}}{\partial x_\beta} + \frac{\partial u_\beta^{(1)}}{\partial x_\alpha} \right], \tag{3.20}$$

$$\sigma_{\alpha\beta}^{(1)} = \frac{E_f}{1+\nu_f} \left[\epsilon_{\alpha\beta}^{(1)} + \frac{\nu_f}{1-\nu_f} \epsilon_{\gamma\gamma}^{(1)} \delta_{\alpha\beta} \right]. \tag{3.21}$$

Substituting Eq.(3.19) into Eq.(3.18) and then into the governing equation (2.19), together with the zero and first-order strain energies in Eq.(3.3) and Eq.(3.6), and keeping terms up to the second order, we obtain a nonlinear evolution equation for the isotropic system,

$$\frac{\partial h}{\partial t} = \Omega^2 M \frac{\partial^2}{\partial x_\beta \partial x_\beta} \left[\sigma_m \frac{\partial u_\alpha^{(1)}}{\partial x_\alpha} - \gamma_f h_{\alpha\alpha} + \sigma_m \frac{\partial u_\alpha^{(2)}}{\partial x_\alpha} + \frac{3+\nu_f}{2(1-\nu_f)} U_E^{(0)} \phi + \psi \right]. \tag{3.22}$$

The first two terms in the bracket of Eq.(3.22) are the linear terms as in the first-order equation (3.9), and the last three terms are the nonlinear terms of the second order. Fourier transform of Eq.(3.22) leads to

$$\frac{\partial \hat{h}}{\partial t} = \Omega^2 M k^2 \left[(\frac{2\sigma_m^2}{E_s} k - \gamma_f k^2) \hat{h} - i k_\alpha Q_{\alpha\beta} \hat{\varphi}_\beta \sigma_m - A U_E^{(0)} \hat{\phi} - \hat{\psi} \right]. \tag{3.23}$$

where

$$A = \frac{3+\nu_f}{2(1-\nu_f)} + \frac{(1+\nu_f)(1-2\nu_s)\overline{E}_f}{(1-\nu_s)\overline{E}_s}. \tag{3.24}$$

The semi-implicit algorithm introduced in Chapter 2 is adopted to integrate Eq.(3.23), where the linear part is integrated by a backward finite difference scheme and the nonlinear part by a forward scheme. The time integration takes the form

$$\hat{h}^{(n+1)} = \frac{\hat{h}^{(n)} - \phi^{(n)} \Delta t}{1 - s \Delta t}, \tag{3.25}$$

46

where s is the normalized growth rate as obtained from the linear analysis, and

$$\phi = \frac{1}{2}k^2 \left[\frac{A\overline{E}_s}{(1+\nu_f)\overline{E}_f}\hat{\phi} + \frac{\overline{E}_f}{\overline{E}_s}\hat{\psi} + \frac{\overline{E}_f}{\overline{E}_s}ik_\alpha\overline{Q}_{\alpha\beta}\hat{\varphi}_\beta \right]. \qquad (3.26)$$

The length scale L, the time scale τ, and the modulus $\overline{E}_f$ have been used above to normalize length, time, and stress, respectively. Unlike the first-order equation, numerical simulation of the second-order equation requires specification of a set of physical parameters, including the modulus ratio $(\overline{E}_f/\overline{E}_s)$, and the Poisson's ratios (ν_f and ν_s).

A brief description of the numerical procedures follows. Starting with a thickness profile, $h(x_1, x_2, t)$, compute $\hat{h}(k_1, k_2, t)$ with the Fast Fourier Transform (FFT). Then, in the Fourier space, compute $ik_\alpha\hat{h}$, $\hat{u}_\alpha^{(1)} = ik_\beta Q_{\alpha\beta}\hat{h}\sigma_m$, and $ik_\beta\hat{u}_\alpha^{(1)}$, by simple multiplications. Next, we obtain h_α, $u_\alpha^{(1)}$, and $\partial u_\alpha^{(1)}/\partial x_\beta$ by inverse FFT, and compute the nonlinear terms, ϕ, φ_α, and ψ, in the real space, again by simple multiplications at each grid point. After transforming the nonlinear terms into the Fourier space, Eq.(3.25) is used to update the Fourier transform of the thickness profile, $\hat{h}(k_1, k_2, t + \Delta t)$. The new thickness profile is then obtained by an inverse FFT. The procedures repeat to simulate evolution of the thickness profile. Similar numerical methods have been used in simulations of other evolution problems [131, 132] with good stability and efficiency.

The result from a 2D simulation is shown in Fig.3.3. The normalized physical parameters are: $\overline{E}_f/\overline{E}_s = 1.1$, and $\nu_s = \nu_f = 0.25$. All other numerical parameters are identical to those in Fig.3.1, and the convergence of the result was confirmed with finer discretization and time steps. The result

47
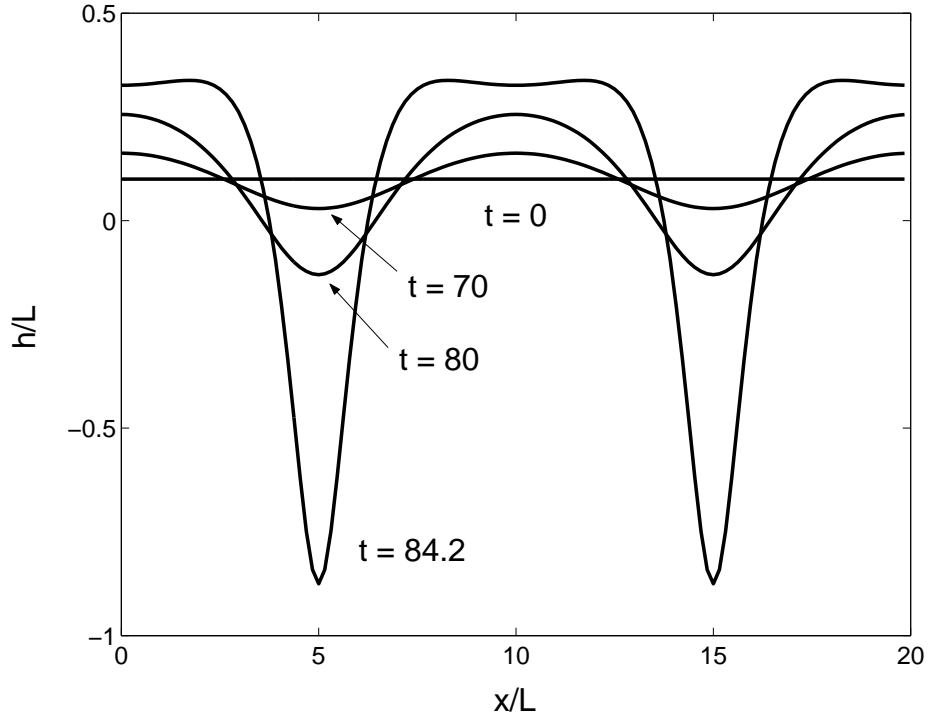
Figure 3.3: Two-dimensional simulation of surface evolution by the nonlinear analysis with no wetting effect.

is dramatically different from Fig.3.1. Instead of self-similar evolution of a sinusoidal perturbation, the surface develops deep grooves, exemplifying the effect of the nonlinear stress field. The result is similar to those obtained by Spencer and Meiron [71] and Xiang and E [72], but somewhat different from that by Yang and Srolovitz [69, 70]. In the latter case, the grooving was more localized, which may be a result of stronger nonlinearity as opposed to the second-order consideration in the present study. As pointed out by Yang and Srolovitz [69, 70], the grooving may lead to nucleation of surface cracks in a stressed solid, even with an initially defect-free, nearly flat surface. For an epitaxial thin film on a substrate, however, the development of deep groov-

48

ing would be suppressed by the wetting effect at the film/substrate interface, which will be discussed in the following section.

A 3D simulation is shown in Fig.3.4, with the same physical parameters as for Fig.3.3. The numerical parameters (including the initial random perturbation) are identical to those in Fig.3.2. The initial stage of surface evolution is similar to Fig.3.2. However, after a finite time, the solution blows up (Figs.3.4(e) and 3.4(f)). Instead of a crack-like grooving expected from the 2D simulations, the surface develops a circular pit-like morphology. The result persists with finer numerical grids and time steps. Similar features were also observed in previous studies [116]. This is believed to be a result of the isotropic model, where both the driving force and the kinetics are isotropic, with no particular direction(s) favored for grooving. On the other hand, the crack-like morphology observed in experiments could be due to the effect of anisotropy in the real systems. For example, in one case, the applied stress was uniaxial [74]. Furthermore, even for an isotropic system, it has been known that a circular void in a stressed solid can be unstable and evolve into a crack-like slit [133]. This process, however, is not captured in the present model because the simulation becomes numerically unstable shortly after the blow-up: the tip of the circular pit advances increasingly faster, requiring higher-order nonlinear analysis for simulations of further evolution.

The above numerical simulations clearly demonstrate the effect of the nonlinear stress field on the dynamics of surface evolution. The nonlinear behavior is far from what can be expected from a linear analysis, and the results can be quite different between 2D and 3D configurations. Since the wetting potential is ignored, the effect of the film/substrate interface is not
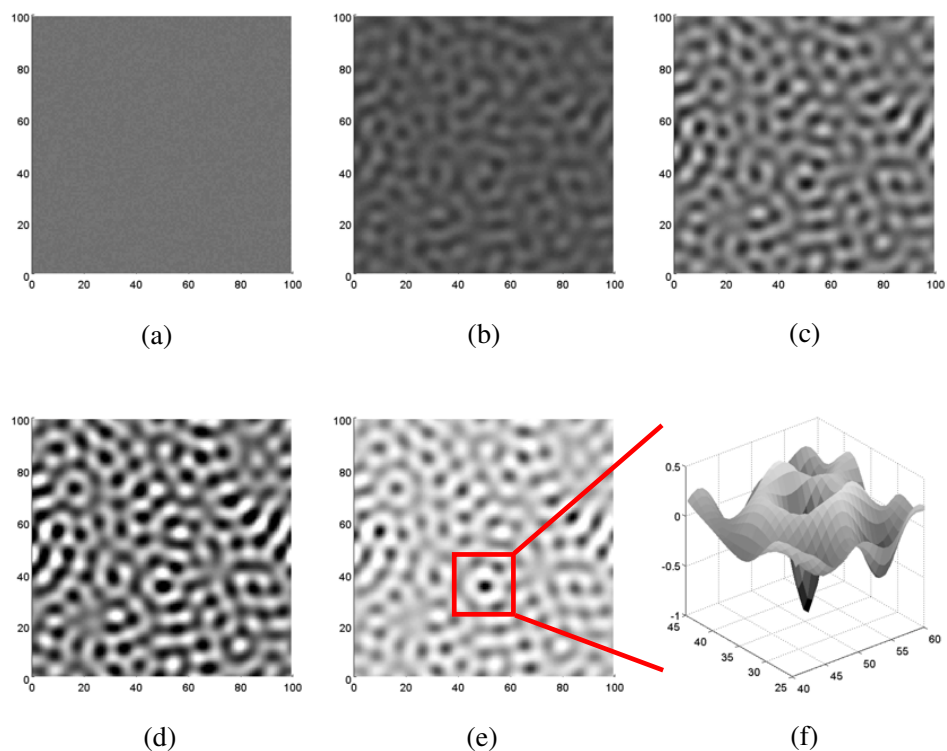
Figure 3.4: Three-dimensional simulation of surface evolution based on the nonlinear analysis with no wetting effect. (a)-(e) are gray scale contour plots of the thickness profile, $h(x_1, x_2)$, white for crests and dark for troughs; (a) random perturbation at t = 0, RMS = 5.77×10-5; (b) t = 20, RMS = 6.67×10-5; (c) t = 50, RMS = 1.3×10-3; (d) t = 70, RMS = 0.97×10-2; (e) t = 93, RMS = 1.16×10-1; (f) The local 3D view of a circular pit at t = 93.

accounted for and the result is essentially identical to that for stressed semi-infinite solids. For thin films, however, the wetting effect must be considered explicitly.

3.3 Effect of wetting

For the SK mode epitaxial growth in our discussion, wetting energy along the interface favors a thin wetting layer, and prevents the substrate to be exposed. The effect of this wetting potential on surface evolution is discussed in this section.

With the same procedure of doing the linear analysis for the stress effects, by linearizing the wetting potential in Eq.(2.16), we obtain the first-order evolution equation taking into account the effect of wetting

$$\frac{\partial h}{\partial t} = \Omega^2 M \frac{\partial^2}{\partial x_\beta \partial x_\beta} \left[\sigma_m \frac{\partial u_\alpha^{(1)}}{\partial x_\alpha} - \gamma_f h_{\alpha\alpha} - \frac{2(\gamma_f - \gamma s)b}{\pi h_0^3} h \right]. \qquad (3.27)$$

Fourier transform of Eq.(3.27) leads to

$$\frac{\partial \hat{h}}{\partial t} = \Omega^2 M k^2 \left[\frac{2\sigma_m^2}{\overline{E}_s} k - \gamma_f k^2 + \frac{2b(\gamma_f - \gamma_s)}{\pi h_0^3} \right] \hat{h}. \qquad (3.28)$$

For a constant wave number k, the solution to Eq.(3.28) has the same form as (3.13), but with a different growth rate

$$s = (kL)^2 \left[kL - (kL)^2 + \frac{2bL^2(\gamma_f - \gamma_s)}{\pi h_0^3 \gamma_f} \right]. \qquad (3.29)$$

The third term in the bracket of Eq.(3.29) represents the effect of wetting
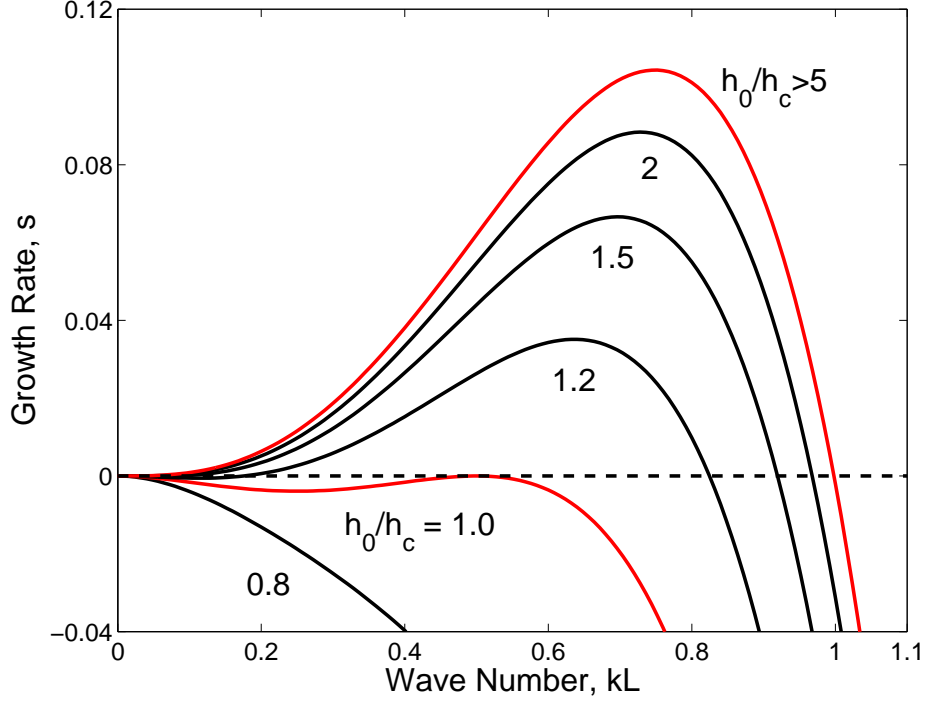
Figure 3.5: Linear analysis of the wetting effect: the growth rate versus the wave number for different film thickness. The critical thickness hc is defined by Eq.(3.28).

on the initial growth rate, which depends on the film thickness (h_0) and the transition of surface energy (i.e., γ_s, γ_f, b). The growth rate versus the wave number is plotted in Fig.3.5 for different film thicknesses.

When $\gamma_f < \gamma_s$, a critical thickness is defined as

$$h_c = 2L \left[\frac{b(\gamma_s - \gamma_f)}{\pi L \gamma_f} \right]^{1/3}. \tag{3.30}$$

If $h_0 < h_c$, the growth rate is negative for all wave numbers; the film is thus stable with a flat surface. If $h_0 > h_c$, the growth rate becomes positive for wave numbers between two critical values. Consequently the flat surface becomes

unstable. This is consistent with the characteristics of SK growth of epitaxial thin films, in which the film morphology undergoes a 2D-3D transition after a critical thickness [20]. Using typical values: $\sigma = 1\text{GPa}$, $\overline{E}_s = 150\text{GPa}$, $\gamma_f = 1\text{N/m}$, $\gamma_s = 1.2\text{N/m}$, and $b = 0.1\text{nm}$, we obtain that $h_c = 6.6\text{nm}$, which is in the reasonable range of the length scale reported by experiments. The critical thickness weakly depends on the length b, which may be selected empirically. For relatively thick films (e.g., $h_0 > 5h_c$), the wetting effect is negligible at the initial stage, and the growth rate is essentially independent of the film thickness. In between, both the growth rate and the fastest growing wave number increases as the film thickness increases. The wetting potential therefore has a significant effect on surface stability and evolution of thin films ($h_0 < 5h_c$).

Another feature which is worthy of more discussion in Fig.3.5 is the existence of a window for the wave number. Once the film thickness is beyond the critical thickness, according to each thickness, there is always a distinct minimum and maximum wave number, between which the fastest growing rate is positive and otherwise outside the window. This indicates that the onset of surface roughening process can be considered under the control of both the deposited film thickness and perturbation condition of the surface.

Interestingly, if $\gamma_f > \gamma_s$, the present analysis predicts that the film becomes increasingly unstable as the thickness decreases. Consequently, the film tends to form clusters at the beginning of growth, characteristic of the Volmer-Weber mode [134]. The dynamics of surface evolution for this case will be left for future studies.

To look at the effect of complete wetting energy form, we start with the

combination of linear other energy terms plus nonlinear wetting energy. By putting the nonlinear wetting term into Eq.(3.27), we obtain,

$$\frac{\partial h}{\partial t} = \Omega^2 M \frac{\partial^2}{\partial x_\beta \partial x_\beta} \left[\sigma_m \frac{\partial u_\alpha^{(1)}}{\partial x_\alpha} - \gamma_f h_{\alpha\alpha} - \frac{\gamma_s - \gamma_f}{\pi}(\xi h_{\alpha\alpha} + \frac{b}{b^2 + h^2}) \right], \quad (3.31)$$

where $\xi = \pi/2 - \arctan(\frac{h}{b})$.

Following the same procedures described in last section, numerical simulations of surface evolution are conducted using the spectral method. First, the result from a 2D simulation is shown in Fig.3.6. In addition to the same parameters used in Fig.3.3, we take $h_0 = 0.1L$, $b = 0.001L$, and $\gamma_s/\gamma_f = 1.2$, which leads to a critical thickness $h_c = 0.08L$. Starting from a sinusoidal perturbation of wavelength 40L, the initial stage of surface evolution ($t < 100$) is similar to those in Figs.3.1 and 3.3, but with a slower growth rate due to the wetting effect, as predicted by the linear analysis. Further evolution ($t = 200$) shows stabilization of a wetting layer between the peaks (or islands), differing from the deep grooving morphology observed in Fig.3.3. Evidently, the wetting effect prevents exposure of the substrate surface. This result is consistent with the "steady state" predicted by Tekalign and Spencer [80]. After a long-time, some islands grow at the expense of their adjacent ones. Eventually, only one island remains within the computational domain, resembling the coarsening process observed in experiments [87], where the number of islands decreases over time. It is noted that, the "steady state" predicted by Tekalign and Spencer was obtained from numerical simulations with one period of a sinusoidal perturbation, in which case no coarsening can occur. In our simulations over a large area, the coarsening process happened and blow-up occurred after
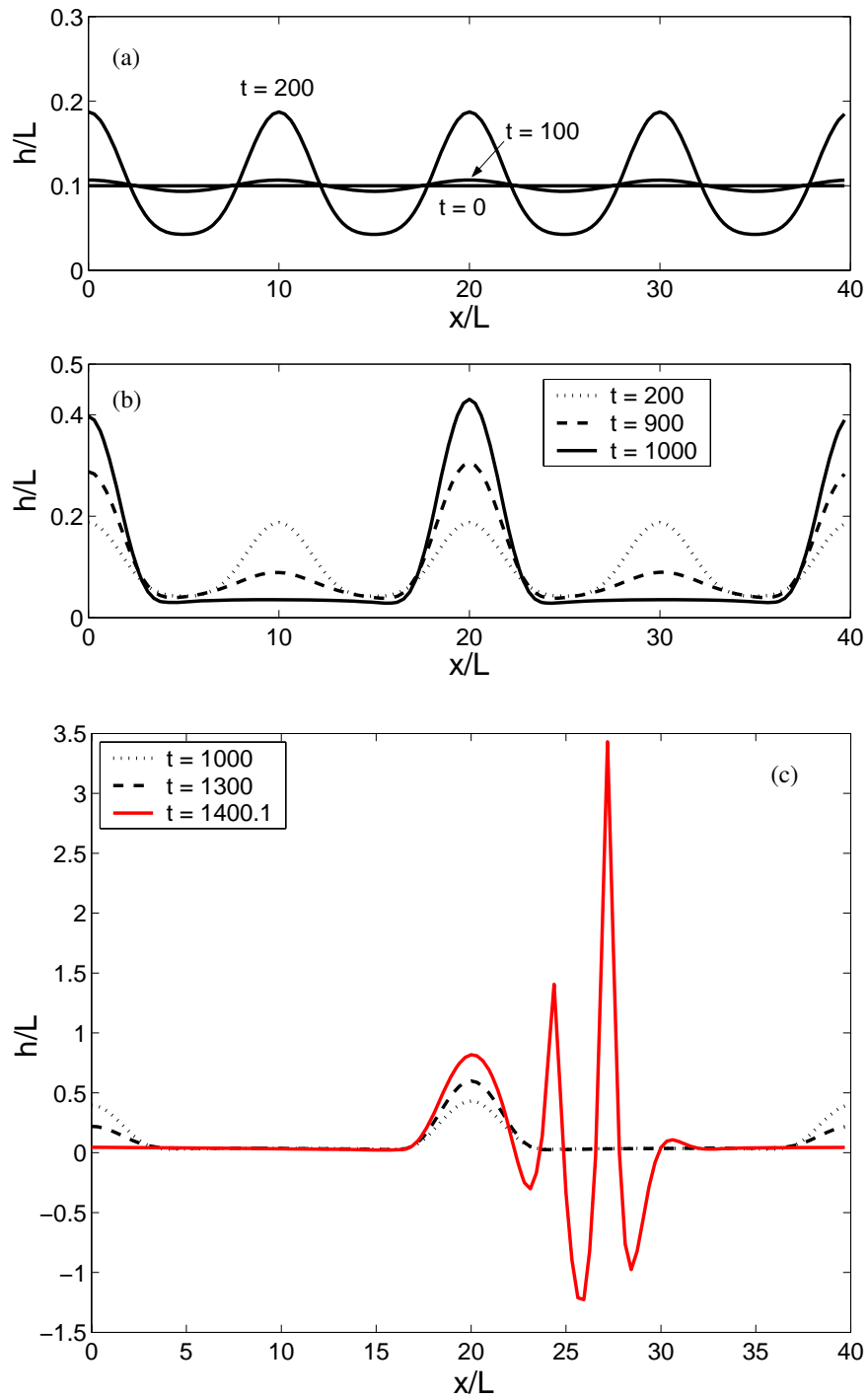
Figure 3.6: Two-dimensional simulation of surface evolution based on the linear stress field plus the nonlinear wetting energy: (a) stable growth (0<t<200); (b) coarsening (t>200); (c) blow-up pit forming (t>1400).

coarsening begins. The blow up solution appears after further evolution of one island morphology, similar to the computations for a perfectly rigid substrate given by Golovin et.al. [116]

Figure 3.7 shows a 3D simulation of the surface evolution. The computational parameters are the same as in Figs.3.2 and 3.4, including the initial perturbation, the computational grid, and the time step. The simulation shows similar surface roughening at the initial stage. During the evolution, instead of deep, circular pits in Fig.3.5, the film breaks up, forming discrete islands on a thin wetting layer. As observed in the 2D simulation, the wetting effect prevents exposure of substrate surface and leads to self-assembly of an array of islands. Further evolution observes coarsening of the island array: some islands grow higher at the expense of the others; consequently, the island number density decreases over time. At a certain stage during the coarsening process ($t > 300$), the blow-up whiskers come out around the highest islands, with other islands keep further coarsening. This can be reasonably explained by the interplay of stress field and wetting energy. Previous study shows that the nonlinear stress field favors downward circular cusp into the substrate for energy relaxation. While for present system, both the absence of nonlinear stress field and the consideration of wetting energy along the interface prevent the surface go deep into the substrate, isolated by a thin wetting layer. During the coarsening process, more and more materials are moved to the bottom of the growing islands with the diminishing of smaller ones. For those "saturated" islands, which thermodynamically reach a equilibrium state and stay with constant shapes and heights, further piling up at the bottom may squeeze the extra materials to blow up. Then, interestingly, stable islands without ei-
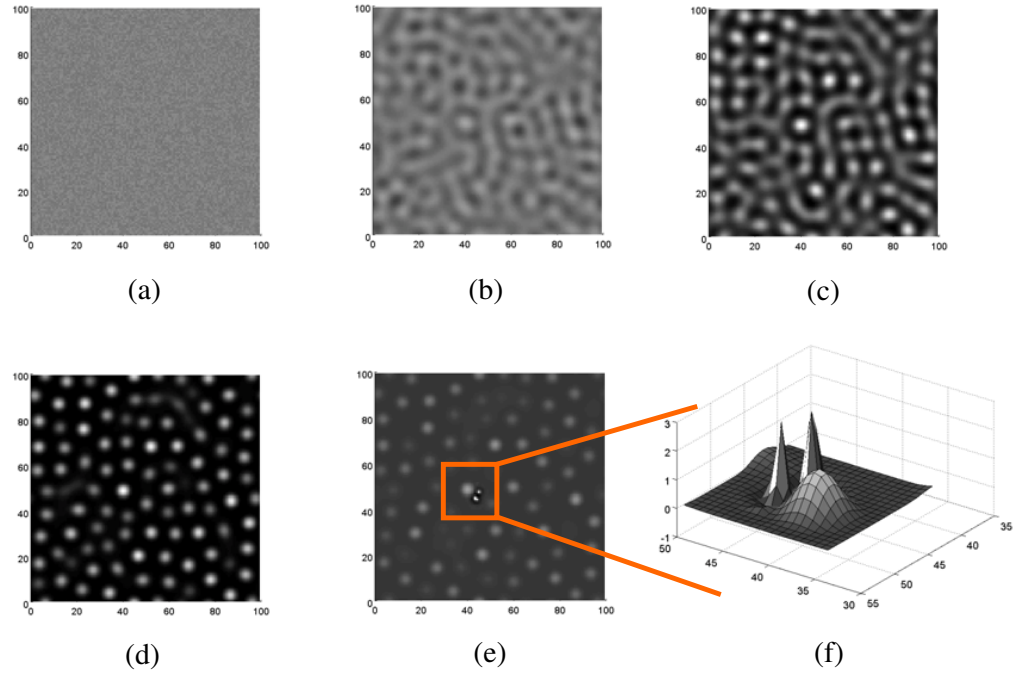
Figure 3.7: Three-dimensional simulation of surface evolution based on the linear analysis of stress field with nonlinear wetting energy. (a)-(f) are gray scale contour plots of the thickness profile, $h(x_1, x_2)$, white for crests and dark for troughs; (a) random perturbation at t = 0, RMS = 5.77×10-5; (b) t = 50, RMS = 5.41×10-5; (c) t = 200, RMS = 2.19×10-2; (d) t = 250, RMS = 9.97×10-2; (e) t = 299.1, RMS = 1.506×10-1; (f) The local 3D view of blow-up pits around the island at t = 301.4.

ther circular cusp into the substrate or upward pits are possible to be achieved by doing nonlinear analysis of both the stress field and the wetting energy.
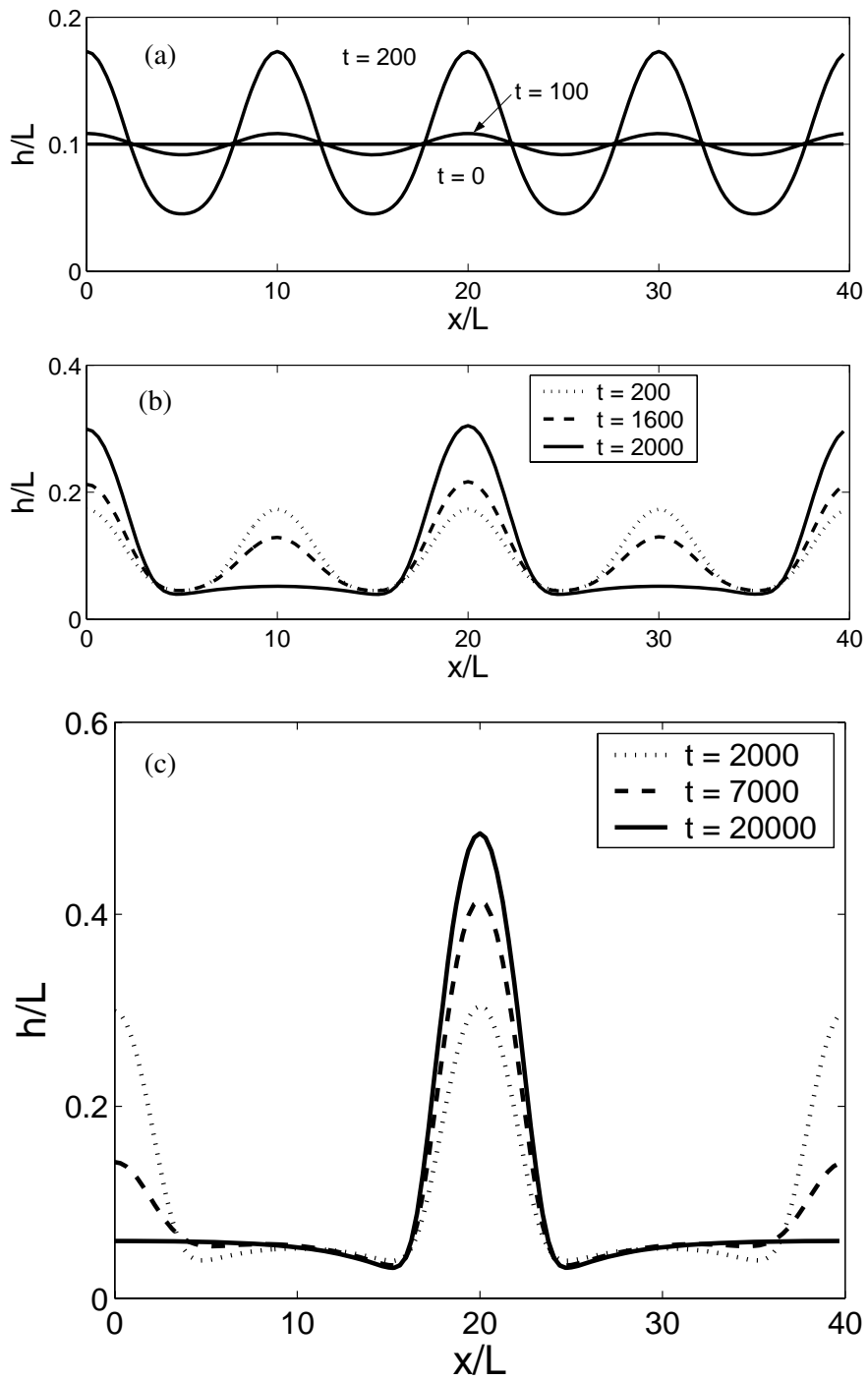
Figure 3.8: Two-dimensional simulation of surface evolution based on the non-linear analysis of both stress and wetting effect: (a) stable growth (0<t<200); (b) coarsening (t>200); (c) further coarsening (t>2000).

58

3.4 Self assembly of isotropic patterns

Including the second-order nonlinear stress field with the full wetting potential, Eq.(2.19) leads to a nonlinear evolution equation,

$$
\frac{\partial h}{\partial t} = \Omega^2 M \frac{\partial^2}{\partial x_\beta \partial x_\beta} \left[\sigma_m \frac{\partial u_\alpha^{(1)}}{\partial x_\alpha} - \gamma_f h_{\alpha\alpha} + \sigma_m \frac{\partial u_\alpha^{(2)}}{\partial x_\alpha} + \frac{3 + \nu_f}{2(1 - \nu_f)} U_E^{(0)} \phi + \right.
$$
$$
\left. \psi - \frac{\gamma_s - \gamma_f}{\pi} (\xi h_{\alpha\alpha} + \frac{b}{b^2 + h^2}) \right],
$$
(3.32)

2D and 3D numerical simulations of Eq.(3.32) are performed by spectral method, and parameters are used the same in Fig.3.6 and Fig.3.7. The result from 2D simulation is shown in Fig.3.8. Starting from a sinusoidal perturbation of wavelength 40L, the initial stage of surface evolution and the stabilization of a wetting layer between the islands ($t \leq 200$) are similar to those in Fig.3.6(a). Further evolution and coarsening, compare with Fig.3.6(b), has a much slower coarsening process due to the interplay of nonlinear stress field and wetting energy. The effect of the nonlinear stress field in the present study becomes prominent as the evolution continues (Fig.3.8(c)). Eventually, only one island remains within the computational domain. Remarkably, the solution does not blow up, even after a very long time ($t = 20000$). The present simulation shows that the height of the surviving island increases while its lateral size (diameter) and location remain nearly unchanged. This, however, seems to contradict with experiments where islands typically grow in both height and diameter. The contradiction is attributed to the effect of anisotropy in the surface energy of real materials, which tends to select a particular surface orientation, thus leading to simultaneous growth in the height and diameter

during coarsening as well as shape transition in the later stage [87]. With the isotropic model of the present study, however, more elastic energy can be released as the aspect ratio of the island increases, without much penalty of increasing the surface energy.

Figure 3.9 shows the 3D simulation of the surface evolution. The simulation shows similar surface roughening with higher island density. Further evolution observes coarsening of the island array. After a very long time of evolution (up to $t = 30000$), the island array seems to reach an equilibrium state with no further coarsening. The island size in the final array is nearly uniform, but no obvious spatial pattern is observed. In spite of the limitations of the present model, the dynamics of island formation and coarsening over a large area is reasonably captured by the interplay of the nonlinear stress field and the wetting effect. It should be noted that shape transition of individual islands predicted by previous works [96, 104–106] is not captured in the present simulation due to assumption of isotropic surface energy. Here we focus on macroscopic shape and large-area organization of islands rather than detailed surface facets and steps at atomic scale.

Figure 3.10 compares the evolution of the surface roughness obtained from the 3D simulations (i.e., Figs.3.2, 3.4, 3.7, and 3.9). The surface roughness is quantitatively determined by the root mean square (RMS) of the thickness profile, namely

$$\mathbf{RMS}(t) = \sqrt{\frac{1}{N^2} \sum_{m=1}^{N} \sum_{n=1}^{N} [h(m, n, t) - h_0]^2}. \qquad (3.33)$$

where N is the number of the grid points along one side of the computational
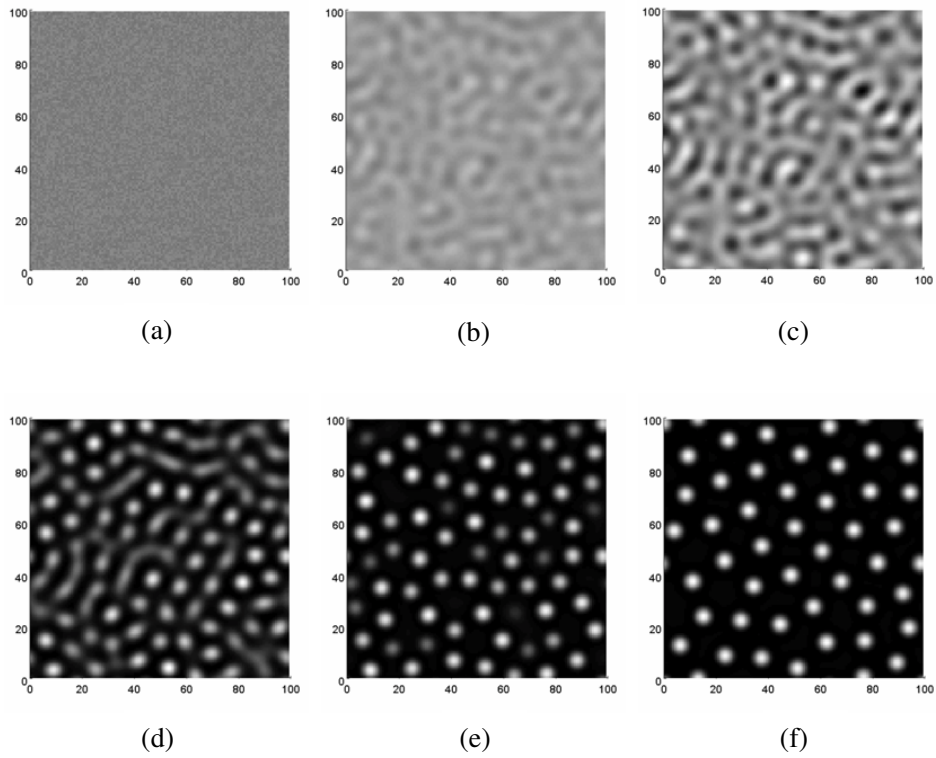
Figure 3.9: Three-dimensional simulation of surface evolution based on the nonlinear analysis of both stress and wetting effect. (a)-(f) are gray scale contour plots of the thickness profile, $h(x_1, x_2)$, white for crests and dark for troughs; (a) random perturbation at t = 0, RMS = 5.77×10-5; (b) t = 20, RMS = 1.98×10-5; (c) t = 50, RMS = 5.99×10-5; (d) t = 220, RMS = 5.01×10-2; (e) t = 500, RMS = 9.71×10-2; (f) t = 10000, RMS = 1.195×10-1.
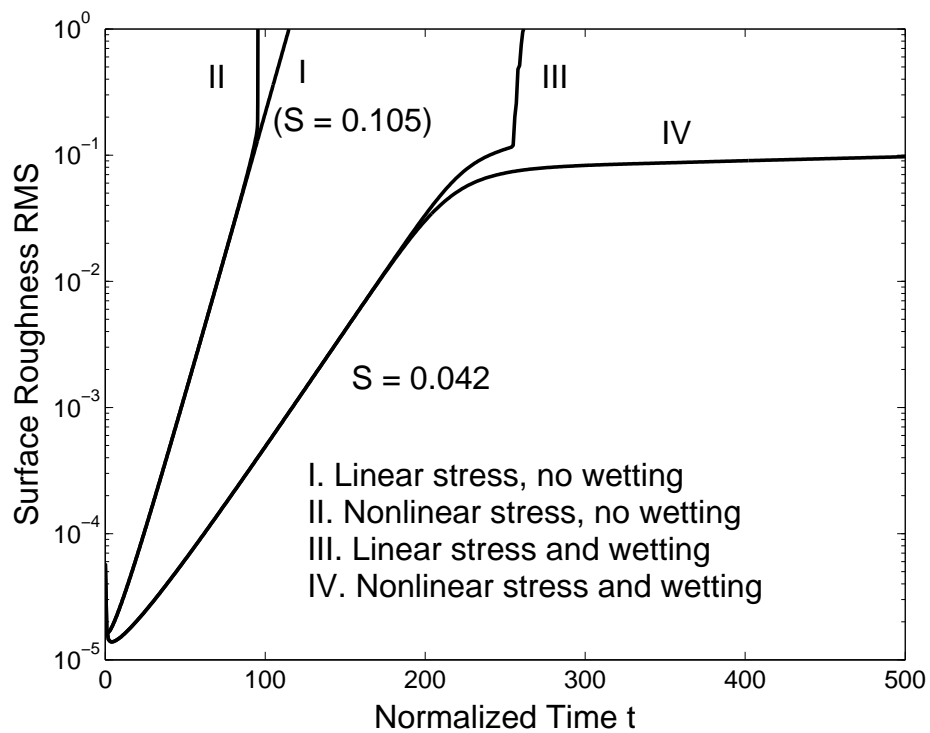
Figure 3.10: Comparison of the evolution of surface roughness from three-dimensional simulations using the linear equation (I), the nonlinear equation with no wetting (II), the linear equation with wetting (III), and the nonlinear equation with wetting (IV).

cell, and $h(m, n, t)$ is the local thickness at the grid point (m, n). Without the wetting effect, the surface roughness initially grows exponentially, with the same growth rate for the linear and nonlinear equations. The growth rate corresponds well with the fastest growing mode predicted by the linear analysis ($s = 0.105$ for $\lambda_m = \frac{8}{3}\pi L$). While the surface evolves self-similarly by the linear equation (Fig.3.2), the nonlinear stress field leads to blow-up of the surface roughness when it develops deep pit-like grooves as shown in Fig.3.4. Including the wetting effect leads to a lower growth rate at the initial stage ($s = 0.042$), as predicted by the linear analysis (Fig.3.5). Again, the growth rate agrees well with the fastest growing mode. After about $t = 200$, the surface roughness saturates. For the case with linear stress field and wetting potential, lack of nonlinear stress components induces the surface roughness to blow up at around $t = 260$, develops whisker-like morphology, in contrast to the "steady state" predicted by Tekalign and Spencer [80]. While for the nonlinear situation (IV), coarsening of the island array continues for a much longer time, the RMS surface roughness does not change significantly after $t = 500$, which can be understood as a result of the competition between roughening due to the growth of the island height and flattening due to the decrease of the island number density. Therefore, both the nonlinear stress field and the wetting effect must be included in studying long-time dynamics of surface evolution.

3.5   Summary

In summary, we have developed a nonlinear evolution equation with a second-order approximation for the stress field and a nonlinear wetting potential for the interface effect. The equation is solved numerically by a spectral method in both two-dimensional (2D) and three-dimensional (3D) configurations. In absence of the interface effect, the nonlinear stress field leads to a "blow-up" solution with crack-like grooving in 2D and circular pit-like morphology in 3D. The blow-up is suppressed by the wetting effect for thin films, leading to formation of an array of islands. Subsequent coarsening and stabilization are observed in the simulations. It is thus concluded that the interplay between the nonlinear stress field and the interfacial wetting has a profound effect on the dynamics of surface evolution that may lead to organization of self-assembled islands or quantum dots.

Chapter 4

Symmetry Breaking and Bifurcation Under Anisotropic Stresses

4.1 Introduction

Experimental investigations have observed deep grooving and cracklike surface patterns in stressed solids [73, 74]. This has been theoretically understood as a result of nonlinear stress effect, which has been discussed in Chapter 3. Recently, Berger et al. [135] analyzed the morphological instability of biaxially stressed solids during a melting-crystallization process, and predicted nontrivial dynamics of pattern formation when the two principal stresses at the solid surface take opposite signs (i.e., tension and compression). Numerical simulations by Paret [136] confirmed the analytical prediction and showed intricate patterns in the nonlinear regime.

65

An epitaxial thin film is stressed due to lattice mismatch with underlying substrate. Interaction between film and substrate further complicates the dynamics of surface evolution, leading to a large variety of surface patterns, such as self-assembled quantum dots. Previous studies have shown that the shape of an individual dot is largely controlled by anisotropy in surface energy [96, 104–106], while the spatial organization of dots is strongly influenced by long-range interactions through elastic stress fields [88, 137]. Experimental investigations have explored various techniques to manipulate the stress field in order to achieve directed organization of quantum dots [33–35, 43, 138–140]. Theoretically, although a few recent works considered the effect of elastic anisotropy [94, 117, 141, 142], systematic studies on the dynamics of pattern formation under influence of anisotropic and/or non-uniform stresses are lacking.

As discussed in Chapter 3, under an equi-biaxial mismatch stress, the rotational symmetry leads to isotropic patterns with no particular organization. Numerical simulations predict self-assembly of circular islands in an isotropic system. In this chapter, we consider epitaxial systems with anisotropic mismatch stresses. We show that, in addition to the generic symmetry breaking, a bifurcation in pattern selection occurs when the film is subjected to an anisotropic mismatch stress. While similar bifurcation was predicted for biaxially stressed solids [135, 136], the epitaxial system exhibits even richer dynamics in forming elongated islands or tilted line patterns. Practically, anisotropic mismatch stresses can be obtained in many systems with either elastically anisotropic film materials or anisotropic substrates. Examples include Ge on Si(113) [48] and hexagonally structured $ErSi_2$ on Si(001) [53],

66

which will be discussed in more details in Chapter 5.

4.2   Linear analysis

Now we consider a same 3D configuration as been presented in chapter 3. At the reference state, a general in-plane mismatch strain correspondingly induces a in-plane biaxial stress state, $\sigma_{11}^{(0)} = \sigma_{m1}$ and $\sigma_{22}^{(0)} = \sigma_{m2}$, and other stress components are zero. Upon annealing, the film surface evolves, with an instantaneous thickness profile, $h(x_1, x_2, t)$. The governing evolution equation still takes the from of Eq.(2.19), and controls the variation of surface profile. Procedures in Chapter 3 can still be followed to calculate every energy terms, but the stress anisotropy makes some difference with respect to specific forms.

In this section, we start with the linear analysis first. Under the general biaxial stress state, corresponding to boundary condition (2.20), the first-order stress field along the surface becomes,

$$\sigma_{31}^{(1)} = h_1\sigma_{m1}, \sigma_{32}^{(1)} = h_2\sigma_{m2}, \tag{4.1}$$

and

$$\sigma_{33}^{(1)} = 0. \tag{4.2}$$

Corresponding strain energy densities for present system are,

$$U_E^{(0)} = \frac{1}{2E_f(\sigma_{m1}^2 + \sigma_{m2}^2 - 2\nu_f\sigma_{m1}\sigma_{m2})}, \tag{4.3}$$

and

$$U_E^{(1)} = \sigma_{m1}\frac{\partial u_1^{(1)}}{\partial x_1} + \sigma_{m2}\frac{\partial u_2^{(1)}}{\partial x_2}, \qquad (4.4)$$

The first-order surface displacement is obtained in the form of Fourier transform:

$$\hat{u}_\alpha^{(1)} = \left(Q_{\alpha 1}ik_1\sigma_{m1} + Q_{\alpha 2}ik_2\sigma_{m2}\right)\hat{h}, \qquad (4.5)$$

For the convenience, the stress anisotropy can be defined as the ratio between the two stress components, namely,

$$c = \frac{\sigma_{m2}}{\sigma_{m1}}. \qquad (4.6)$$

$c = 1$ refers to the isotropic system, and when $c \neq 1$, an anisotropic system is presented. The rotational symmetry is expected to be broken for anisotropic case. To focus on the effect of stress anisotropy, the present study assumes an otherwise isotropic system in the following. Both the film and the substrate are elastically isotropic, with E and ν as Young's modulus and Poisson's ratio, respectively.

Keeping up to the first-order energy terms, a linearized evolution equation is reduced from Eq.(2.19), with different form of isotropic case in Eq.(3.27),

$$\frac{\partial h}{\partial t} = \Omega^2 M \frac{\partial^2}{\partial x_\beta \partial x_\beta}\left[\sigma_{m1}\frac{\partial u_1^{(1)}}{\partial x_1} + \sigma_{m2}\frac{\partial u_2^{(1)}}{\partial x_2} - \gamma_f h_{\alpha\alpha} - \frac{2(\gamma_f - \gamma s)b}{\pi h_0^3}h\right]. \qquad (4.7)$$

Fourier transform of Eq.(4.7) leads to an identical form of Eq.(3.13), with a

different growth rate s,

$$s(k_1, k_2) = \frac{1}{k(1 - \nu_s)} \left[(k_1^2 + k_2^2 c^2)k^2 - (k_1^2 + ck_2^2)^2 \nu_s \right] - k^4 + \frac{2bL^2(\gamma_f - \gamma_s)}{\pi h_0^3 \gamma_f}.$$
(4.8)

It is noted that, the stress anisotropy c comes into the growth rate, and the variation of c must lead to a variety of growth modes, in turn different surface patterns. Figure 4.1 plots the growth rate as contours in the plane of wave vector (k_1, k_2). When $c = 1$, the contours are concentric circles (Fig.4.1(a)), indicating rotational symmetry in the isotropic system. The growth rate is positive in an annular region (bounded by the black edges), and the fastest growing mode corresponds to a circle (the dark color circle). The symmetry is broken when $c \neq 1$. As shown in Fig.4.1(b) and (c), the fastest growing mode corresponds to two points (dark spots), located on one of the principal axes. This suggests that the initial evolution would develop parallel line patterns perpendicular to the principal direction. The generic symmetry breaking persists when c becomes negative, with the principal mismatch stresses tensile in one direction and compressive in the orthogonal direction. In addition, a bifurcation occurs at a critical value. As shown in Fig.4.1(d) for $c = -1$, the fastest growing mode now corresponds to four points located at angles $\pm 45^o$ from the principal directions, i.e., the two dark spots in Fig.4.1(b) have split into four.

Define the angle θ of wave vector such that $k_1 = k \cos\theta$ and $k_2 = k \sin\theta$ in Eq.(4.8). Setting $\partial s/\partial\theta = 0$ with respect to s leads to

$$(c - 1)[(1 - \nu_s)(1 + c) - \nu_s(1 - c)\cos 2\theta]\sin\theta\cos\theta = 0. \qquad (4.9)$$
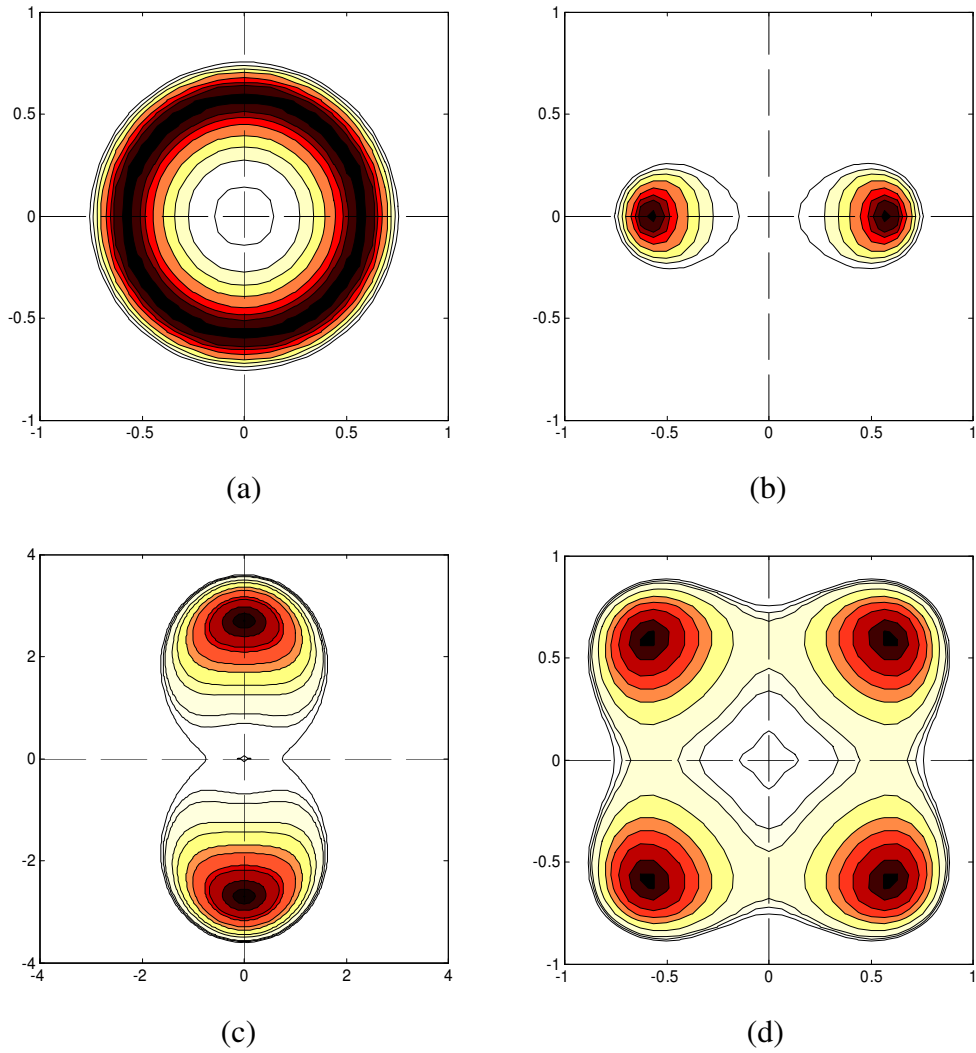
Figure 4.1: Contours of the growth rate, : (a) c = 1, (b) c = 0, (c) c = 2, and (d) c = -1.

When $c = 1$, $\partial s/\partial \theta = 0$ is satisfied all around, thus no particular angle is selected for the fastest growth. When $c \neq 1$, the angle of the fastest growing mode can be determined by examining the second derivative of the growth rate. For $0.5 > \nu_s > 0$, three cases exist: (I) When $1 > c > -(1 - 2\nu_s)$, $\sin\theta = 0$ for the fastest growth, giving $\theta = 0$. (II) When $c > 1$ or $c < -(1 - 2\nu_s)^{-1}$, the fastest growing mode corresponds to $\cos\theta = 0$, and thus $\theta = \pm 90^o$. Cases I and II are equivalent upon switching σ_{m1} and σ_{m2}. (III) When $-(1 - 2\nu_s)^{-1} < c < -(1 - 2\nu_s)$, the angle of the fastest growing mode is given by

$$\cos 2\theta = \frac{(1 + c)(1 - \nu_s)}{(1 - c)\nu_s}. \tag{4.10}$$

Figure 4.2 plots the angle of the fastest growing mode as a function of stress anisotropy. A pitchfork bifurcation occurs at $c = -(1 - 2\nu_s)^{\pm 1}$ ($c = -0.5$ in the figure). In between, the angle rotates from one principal direction to another, through two equivalent paths (clockwise or counterclockwise). In the present system, there exist two types of transition: a step transition at $c = 1$ as the result of generic symmetry breaking, and a smooth transition from $c = -(1 - 2\nu_s)$ to $c = -(1 - 2\nu_s)^{-1}$ via the bifurcation. Similar bifurcation patterns were reported for binary compositional fields in self-assembled monolayers [143, 144].

4.3 Numerical simulations

Nonlinear evolution process for the system with anisotropic mismatch stress is aimed to investigate by numerical simulation in this part.
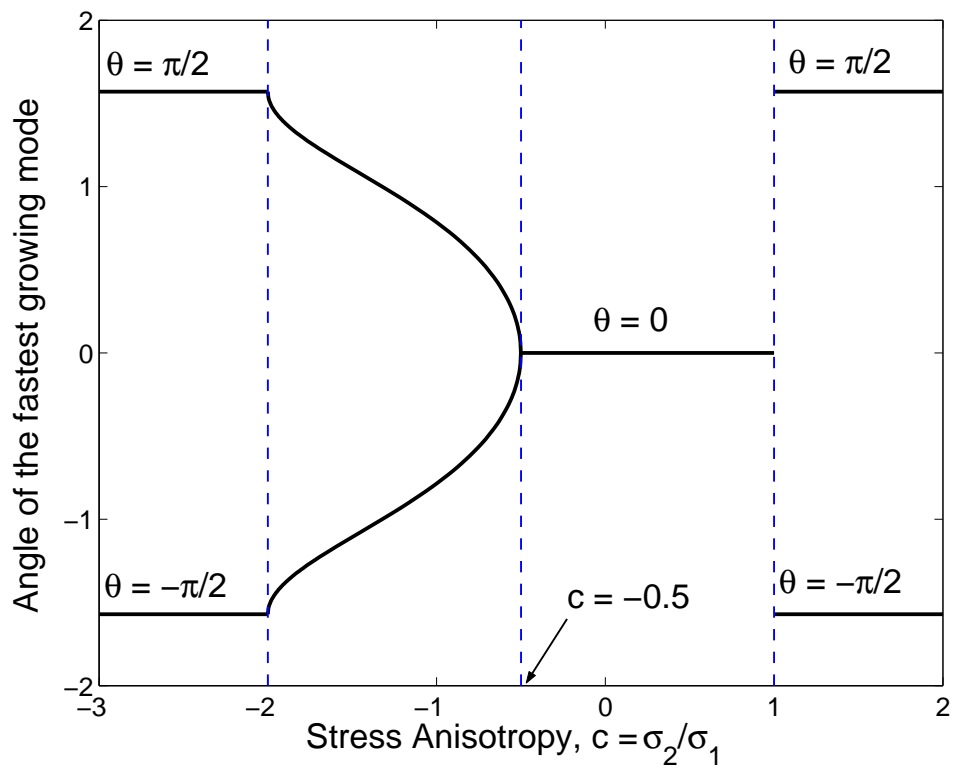
Figure 4.2: Angle(s) of the fastest growing mode as a function of stress anisotropy ($\nu_s = 0.25$).

Second-order nonlinear stress field are obtained similarly from Chapter 3,

$$\sigma_{3\alpha}^{(2)} = \sigma_{\alpha\beta}^{(1)} h_\beta, \tag{4.11}$$

and

$$\sigma_{33}^{(2)} = \sigma_{m1} h_1 h_1 + \sigma_{m2} h_2 h_2. \tag{4.12}$$

Second-order strain energy is

$$U_E^{(2)} = \frac{1}{2}\sigma_{ij}^{(1)}\epsilon_{ij}^{(1)} + \sigma_{m1}\frac{\partial u_1^{(2)}}{\partial x_1} + \sigma_{m2}\frac{\partial u_2^{(2)}}{\partial x_2}, \tag{4.13}$$

Corresponding second-order surface displacements are calculated in the Fourier space,

$$\hat{u}_\alpha^{(2)} = Q_{\alpha\beta} F[\sigma_{\beta\gamma}^{(1)}] + Q_{\alpha3} F[\sigma_{m1} h_1 h_1 + \sigma_{m2} h_2 h_2], \tag{4.14}$$

and

$$\hat{u}_3^{(2)} = Q_{3\beta} F[\sigma_{\beta\gamma}^{(1)}] + Q_{33} F[\sigma_{m1} h_1 h_1 + \sigma_{m2} h_2 h_2]. \tag{4.15}$$

Nonlinear governing equation is obtained by keeping the full wetting potential term together with up to second-order strain energy terms, namely,

$$\begin{aligned}
\frac{\partial h}{\partial t} = \Omega^2 M \frac{\partial^2}{\partial x_\beta \partial x_\beta} \Bigg[&\frac{1}{2} U_0 h_\alpha h_\alpha + \sigma_{m1}\frac{\partial u_1^{(1)}}{\partial x_1} + \sigma_{m2}\frac{\partial u_2^{(1)}}{\partial x_2} + \sigma_{m1}\frac{\partial u_1^{(2)}}{\partial x_1} + \\
&\sigma_{m2}\frac{\partial u_2^{(2)}}{\partial x_2} + \frac{1}{2}\sigma_{ij}^{(1)}\epsilon_{ij}^{(1)} - \gamma h_{\alpha\alpha} - \frac{\gamma_s - \gamma_f}{\pi}(\frac{b}{b^2 + h^2}) \Bigg],
\end{aligned} \tag{4.16}$$

Evolution equation (4.16) can be solved efficiently by the spectral method.

The numerical results are normalized by a similar length scale,

$$L = \frac{\gamma_f \overline{E}_s}{2\sigma_{m1}^2}, \tag{4.17}$$

and a time scale,

$$\tau = \frac{L^4}{\Omega^2 M \gamma_f} = \frac{\gamma_f^3 \overline{E}_s^4}{16\Omega^2 M \sigma_{m1}^8}. \tag{4.18}$$

The parameters used in simulations are the same as we used for the 3D simulation in Chapter 3. When the film is subjected to an equi-biaxial mismatch stress ($c = 1$), the surface evolves through the exact isotropic evolution sequence, which behaves identical to Fig.3.9 in Chapter 3: where the surface first evolves into a chaotic pattern without particular orientation preference, and breaks up into circular dots. For a long time evolution, after the coarsening process, the pattern is stabilized, with a nearly uniform dot size and random location. The rotational symmetry of the isotropic system is responsible for the initial chaotic pattern as well as the randomly organized circular dots.

Symmetry breaking predicted in Fig.4.1 is confirmed by numerical simulation as shown in Fig.4.3 for $c = 0$. A parallel line pattern emerges at the early stage for evolution. The nonlinear effects of stress and wetting take over for long-time evolution, breaking up the lines into elongated islands.

Figure 4.4 shows a simulated evolution sequence of surface pattern with $c = -1$. At the early stage, as opposed to the parallel line pattern in Fig.4.3, the two angles of the fastest growth, $\theta = \pm 45^o$, compete, leading to a diamond pattern. Subsequently, square-shaped islands form and undergo coarsening. Interestingly, after a long time, the islands coalesce to form tilted lines. The
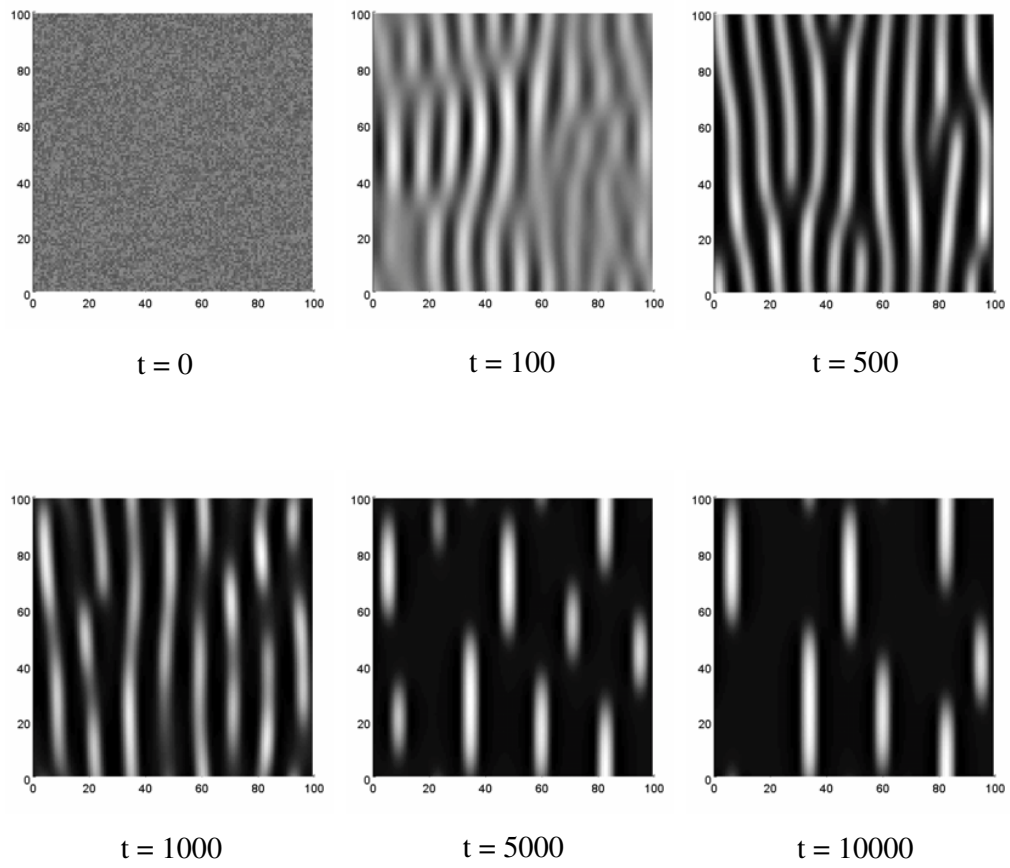
Figure 4.3: Contours of simulated surface morphology, $h(x1, x2, t)$, with $c = 0$.

t = 0   t = 50   t = 200

t = 500   t = 1000   t = 10000
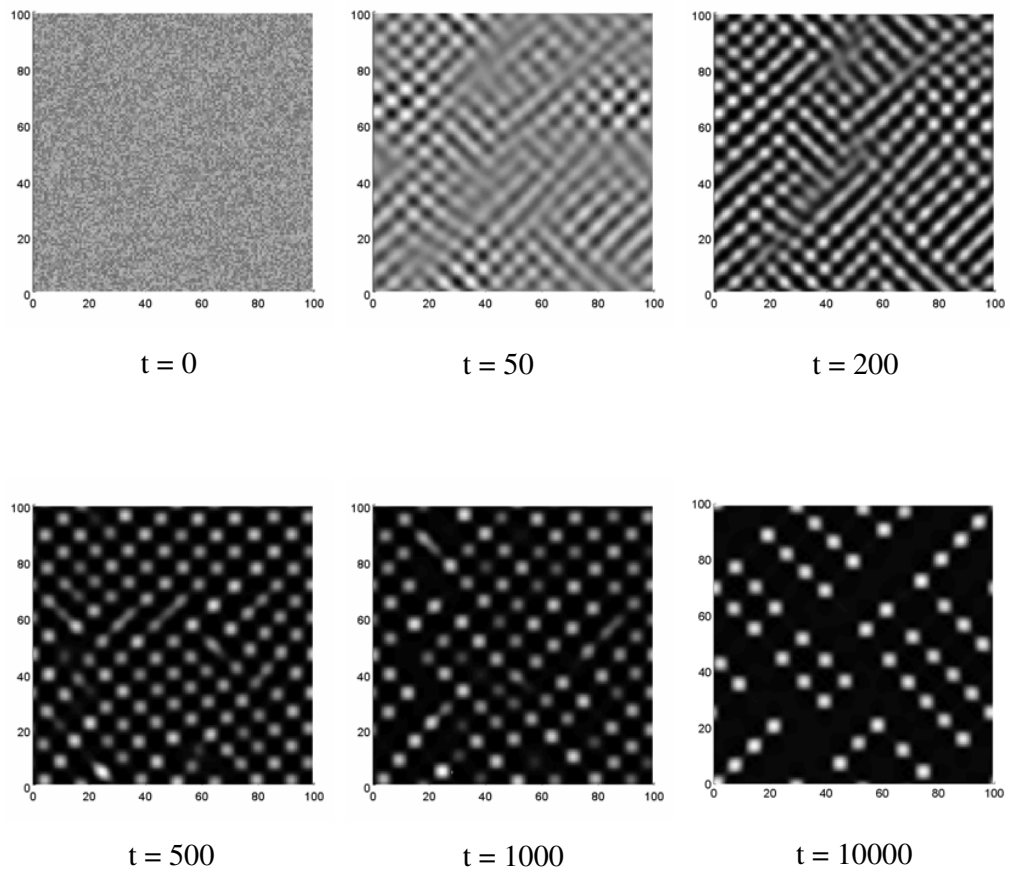
Figure 4.4: Contours of simulated surface morphology, $h(x1, x2, t)$, with $c = -1$.

c = 0.5   c = 0   c = - 0.25

c = - 0.5   c = - 0.75   c = - 1
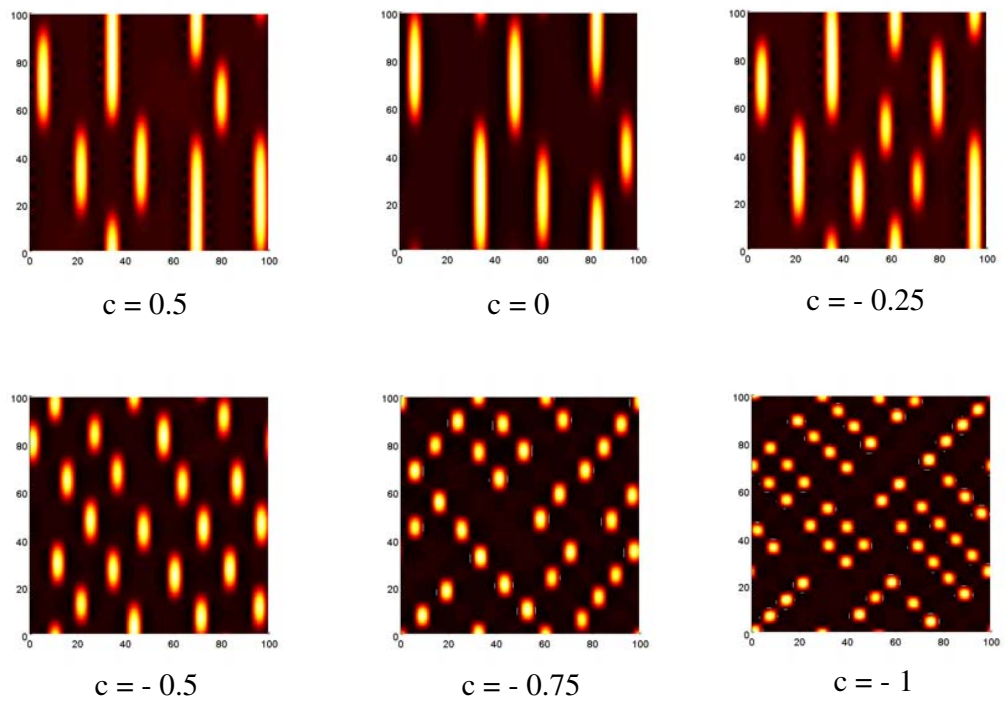
Figure 4.5: Surface patterns of different stress anisotropy.

competition of the two tilting directions leads to co-existing of long and short (broken) lines. Compared to previous studies on stressed solids [135, 136], the long-time dynamics of pattern evolution is more complicated in the epitaxial system due to film-substrate interaction.

A set of surface patterns with respect to different stress anisotropy c is illustrated in Figure 4.5. These 3D simulation results presents a quite rich variety of surface morphologies, following well with the prediction given by linear analysis in Fig.4.2.

4.4 Summary

The present study considers the effect of stress anisotropy in an otherwise isotropic epitaxial system. Rotational symmetry breaking and surface pattern selection are presented as the effect of anisotropy from mismatch stress. In real systems, stress anisotropy is usually coupled with other material anisotropy. For example, in an epitaxial system with Ge on Si(113), an in-plane stress state exists with two principle stresses in $[\bar{1}10]$ and $[\bar{3}\bar{3}2]$ directions, respectively, and with $\sigma_{m1} < \sigma_{m2}$. Based on the discussion in this chapter, parallel lines are expected to form in the $[\bar{1}10]$ direction, while lines in $[\bar{3}\bar{3}2]$ are mostly observed in experiments. This discrepancy may be resolved by including effects of elastic anisotropy and surface energy anisotropy. The interactions among different anisotropy would further complicate and also enrich the dynamics of pattern formation in the epitaxial system, which will be left for future studies.

Chapter 5

Evolution and Self Assembly of Anisotropic Patterns

5.1 Introduction

Most of the previous studies on surface evolution have assumed isotropic elasticity for the film and the substrate. This assumption however contradicts the crystalline nature in essentially all epitaxial systems. While the anisotropic elasticity may not be critically important for the understanding of the surface instability, it is expected to play a significant role in the ordering of surface structures over long term evolution [143]. Recently, by using anisotropic elastic properties of cubic crystals and solving the evolution equation by a finite element method, Liu et al. [145] showed alignment of self-assembled islands on both <100> and <110> directions on a (001) surface, depending on the strength of elastic anisotropy. Previously, Shenoy and Freund [98] developed an anisotropic elasticity solution by using the half-space Green's function to

the first order of the surface slope. In the present study, we have developed a nonlinear evolution equation for generally anisotropic epitaxial systems in Chapter 2, along with the asymptotic solution to the anisotropic nonlinear elasticity problem. In this chapter, we consider two specific epitaxial systems and discuss the effect of elastic anisotropy on surface pattern evolution. First, a cubic system, SiGe on Si, is considered. Four different crystal orientations of the substrate, Si(001), Si(110), Si(111), and Si(113), are studied here. Crystal orientations are expected to play an important role in the surface stability and pattern evolution [19, 42, 47, 50, 52, 87, 146]. Second, the self-assembly of rare-earth silicides on Si(001) is investigated, and the combined anisotropy effects are illustrated.

5.2 Epitaxial SiGe films on Si substrates

SiGe alloy on Si is one of the mostly studied systems exhibiting self-assembled nanostructures in semiconductor heteroepitaxy. During the past decades, the research activity in the growth, characterization and exploitations of SiGe on Si growth have been rapidly developed [25, 26, 31, 48, 137, 147–150]. In this part, we will focus our discussion on the evolution and self assembly properties of such an epitaxial system.

Both Si and Ge have cubic crystalline structures, and they form totally miscible solid solution, SiGe, over the entire range of Ge concentration [99]. Experiments have shown that the lattice constant of SiGe is closely matched

with a simple liner interpolation between Si and Ge [99], i.e.,

$$a_{SiGe} = (1 - x)a_{Si} + xa_{Ge}, \qquad (5.1)$$

where $a_{Si} = 0.5428nm$, $a_{Ge} = 0.5658nm$, and x is the Ge concentration of SiGe. Consequently, the lattice mismatch between an epitaxial SiGe film and its Si substrate induces an equi-biaxial compressive strain:

$$\epsilon_{11}^{(0)} = \epsilon_{22}^{(0)} = \epsilon_m = -0.04x. \qquad (5.2)$$

Note that the mismatch strain is independent of either the crystal orientation of the epitaxial surface or the selection of the in-plane coordinate axes. On the other hand, the mismatch stress varies with the crystal orientation due to anisotropy in the elastic moduli. The elastic moduli of SiGe are also obtained by a linear interpolation between those for Si and Ge [151], namely

$$C_{ijkl}^{SiGe} = (1 - x)C_{ijkl}^{Si} + xC_{ijkl}^{Ge}. \qquad (5.3)$$

Similarly, we take the surface energy density of SiGe as

$$\gamma_{SiGe} = (1 - x)\gamma_{Si} + x\gamma_{Ge}. \qquad (5.4)$$

The elastic moduli of Si and Ge, referring to their natural crystal coordinates, are listed in Table 5.1. The elastic moduli are taken from Freund and Suresh [12], referring to the natural crystal coordinates. The surface energy values are from Stekolnikov et al. [152] for (001), (110), and (111) surfaces and from

81

Table 5.1: Elastic moduli and surface energy density of Si and Ge.

		Si	Ge
Elastic moduli (GPa)	C_{11}	166.2	128.4
	C_{12}	64.4	48.2
	C_{44}	79.8	66.7
Surface energy density (J/m^2)	(001)	2.39	1.71
	(111)	1.82	1.32
	(110)	2.04	1.51
	(113)	2.21	1.61

Stekolnikov et al. [153] for (113) surfaces.Transformations of the elastic moduli to a different epitaxial coordinate (Fig.5.1) due to the variation of substrate orientations are performed by standard approach given in Appendix B. The values of surface energy density for Si and Ge are also listed in Table 5.1. Although the surface energy is assumed to be isotropic for each epitaxial system in the present study, different values are used for (001), (111), (110), and (113) surfaces [152, 153]. We note quite a scattering in the reported surface energy values obtained from experiments and theoretical calculations, which vary significantly with specific surface conditions such as surface relaxation, reconstruction, and hydrogenation [152, 153]. For simplicity, we use the values of unrelaxed surfaces in the present study.
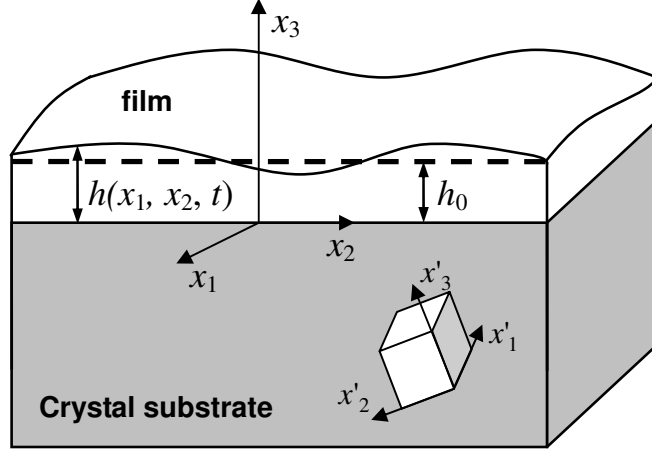
Figure 5.1: Schematic illustration of an epitaxial film on a crystal substrate. An arbitrarily rotated crystal lattice is noted by coordinates $x_i'(i = 1 - 3)$, while the epitaxial coordinates are x_i with $x_3 = 0$ at the film/substrate interface. The film has a mean thickness h_0 and an instantaneous local thickness, $h(x_1, x_2, t)$.

Referring to Chapter 2, governing equation (2.19) is adopted to trace the surface evolution for current SiGe/Si system. The linear analysis can be performed by keeping only the first order terms for the strain energy density, the surface mean curvature, and the wetting potential. Corresponding Fourier transform of linearized evolution equation leads to a differential equation, which takes the form of Eq.(3.13), with a general form of growth rate in Fourier space,

$$s(k_1, k_2) = -\Omega^2 M_0 k^2 [-k_\alpha k_\beta Q_{\chi\kappa} \sigma_{\alpha\chi}^{(0)} \sigma_{\beta\kappa}^{(0)} + \gamma_0 k^2 + \frac{2h_0 b(\gamma_s - \gamma_f)}{\pi(b^2 + h_0^2)^2}]. \qquad (5.5)$$

For an isotropic system with an equi-biaxial mismatch stress (i.e., $\sigma_{11}^{(0)} = \sigma_{22}^{(0)} = \sigma_m$ and $\sigma_{12}^{(0)} = 0$), Eq.(5.5) is reduced to Eq.(3.29). The first two terms in Eq.(3.29) represent a competition between the elastic strain energy and the

83

surface energy, and the competition defines a length scale and a time scale Eq.(3.11) and Eq.(3.12). Similar length and time scales can be defined for a generally anisotropic systems by using a combination of elastic moduli and mismatch strain. For the present study, we set

$$L = \frac{\gamma_f \overline{E}_s}{2(\overline{\epsilon}_m \overline{E}_f)^2}, \tau = \frac{\gamma_f^3 \overline{E}_s^4}{16\Omega^2 M (\overline{\epsilon}_m \overline{E}_f)^8}, \tag{5.6}$$

where $\overline{\epsilon}_m = \frac{1}{2}(\epsilon_{11}^{(0)} + \epsilon_{22}^{(0)})$ is the mean mismatch strain, $\overline{E}_s = C_{11\_s} - C_{12\_s}^2/C_{11\_s}$ as the effective plane-strain modulus for the substrate, and $\overline{E}_f = C_{11\_f} + C_{12\_f} - 2C_{12\_f}^2/C_{11\_f}$ as the effective biaxial modulus for the film; the elastic moduli are written in the Voigt's abbreviated notation with subscripts s and f for the substrate and film, respectively. The effective moduli are defined such that the scales in Eq.(5.6) recover those in Eq.(3.11) and Eq.(3.12) for an isotropic system.

The third term in the bracket of Eq.(3.27) represents the effect of wetting on the initial growth, which sets a critical thickness, Eq.(3.30), for an isotropic system. Similarly, the critical thickness for an anisotropic system can be determined, taking the form

$$h_c = \eta L \left[\frac{(\gamma_s - \gamma_f)b}{\pi \gamma_f L} \right]^{1/3}, \tag{5.7}$$

where the coefficient η depends on the elastic anisotropy of the substrate as well as the mismatch strain. The critical thicknesses for specific anisotropic systems are discussed in the following sections.

By far, the only parameter that remains to be determined in the present

model is the thickness b for the transition of surface energy. Noting that the critical thickness for the epitaxial surface given in Eq.(5.7) depends on the transition thickness, a value $b = 0.005L \approx 0.02nm$ is estimated by comparing the prediction with an experimentally measured critical thickness, $h_c \approx 0.7nm$ for epitaxial Ge films on Si(001) [148]. This value is used in the present study for all quantitative analyses.

By including all the second-order energy terms, the nonlinear evolution equation is obtained, and numerical simulations are given by spectral method. A brief description of the simulation procedures follows, which is similar but somewhat complicated than that of isotropic case introduced in Chapter 3. The mean film thickness and the mismatch strain is specified at first. With the anisotropic elastic moduli of the substrate, the compliance matrix, Q_{ij}, is calculated following the steps that lead to Eq.(A.33) in Appendix A. Then, taking a randomly generated thickness profile of small roughness as the initial condition, the surface evolution is simulated by updating the thickness profile over a number of time steps. For each time step, we compute the Fourier transform of the current thickness profile, $\hat{h}(k_1, k_2, t)$, by the Fast Fourier Transform (FFT) method. In the reciprocal Fourier space, the quantities $ik_\alpha \hat{h}$, $\hat{u}_i^{(1)} = ik_\beta Q_{i\alpha} \sigma_{\alpha\beta}^{(0)} \hat{h}$, and $ik_\beta \hat{u}_i^{(1)}$ are computed by simple multiplications at each grid point (Fourier component). Next, we obtain corresponding quantities in the real space, h_α, $h_i^{(1)}$, and $\partial u_i^{(1)}/\partial x_\beta$, by inverse FFT, and compute the nonlinear terms, such as $\sigma_{3\alpha}^{(2)} = \sigma_{\alpha\beta}^{(1)} h_\beta$, $\sigma_{33}^{(2)} = \sigma_{\alpha\beta}^{(0)} h_\alpha h_\beta$, $\sigma_{\alpha\beta}^{(1)} \partial u_\alpha^{(1)}/\partial x_\beta$, $h_\alpha h_\alpha$, and $\gamma h_{\alpha\alpha}$, by simple multiplications at each grid point (physical coordinate). After that, we transform the nonlinear terms back into the Fourier space and update the Fourier transform of the thickness profile, $\hat{h}(k_1, k_2, t+\Delta t)$. The final thickness profile

in the physical space is obtained by an inverse FFT at the end of the last time step. All numerical simulations, we normalize the evolution equation using the length and time scales defined in Eq.(5.6) and discretize the computational cell of size 100×100 into a 128 by 128 grid with a periodic boundary condition. To compare the results for different crystal orientations, the length scale for a pure Ge film on Si(001) substrate is used for all calculations. The length scale in this case is: $L = 3.83nm$. As will be shown later, the length scale increases dramatically for SiGe films as the Ge concentration decreases.

5.2.1   Effect of substrate crystal orientation

Starting from a nearly flat film surface, the evolution dynamics at the early stage can be understood by the linear analysis in above section. First, the growth rate of the Fourier component as a function of the wave vector dictates the stability and the fastest growing modes. Figure 5.2 plots the contours of the growth rate in the plane of (k_1, k_2) for Ge films of a mean thickness, $h_0 = 0.2L$, on the four Si substrates; only positive growth rates are shown in the contours. For the Ge/Si(001) epitaxy (Fig.5.2(a)), the growth rate is positive in a diamond shaped region, with four peaks symmetrically located on the k_1 and k_2 axes. This predicts the fastest growing modes at the early stage, with the wave vectors along the [100] and [010] directions. Apparently, the elastic anisotropy of the cubic crystal breaks the rotational symmetry of surface evolution as predicted previously for isotropic systems in Chapter 3. As will be shown later by numerical simulations, the break of symmetry eventually leads to ordered surface patterns as opposed to the lack of ordering in the isotropic systems.

86
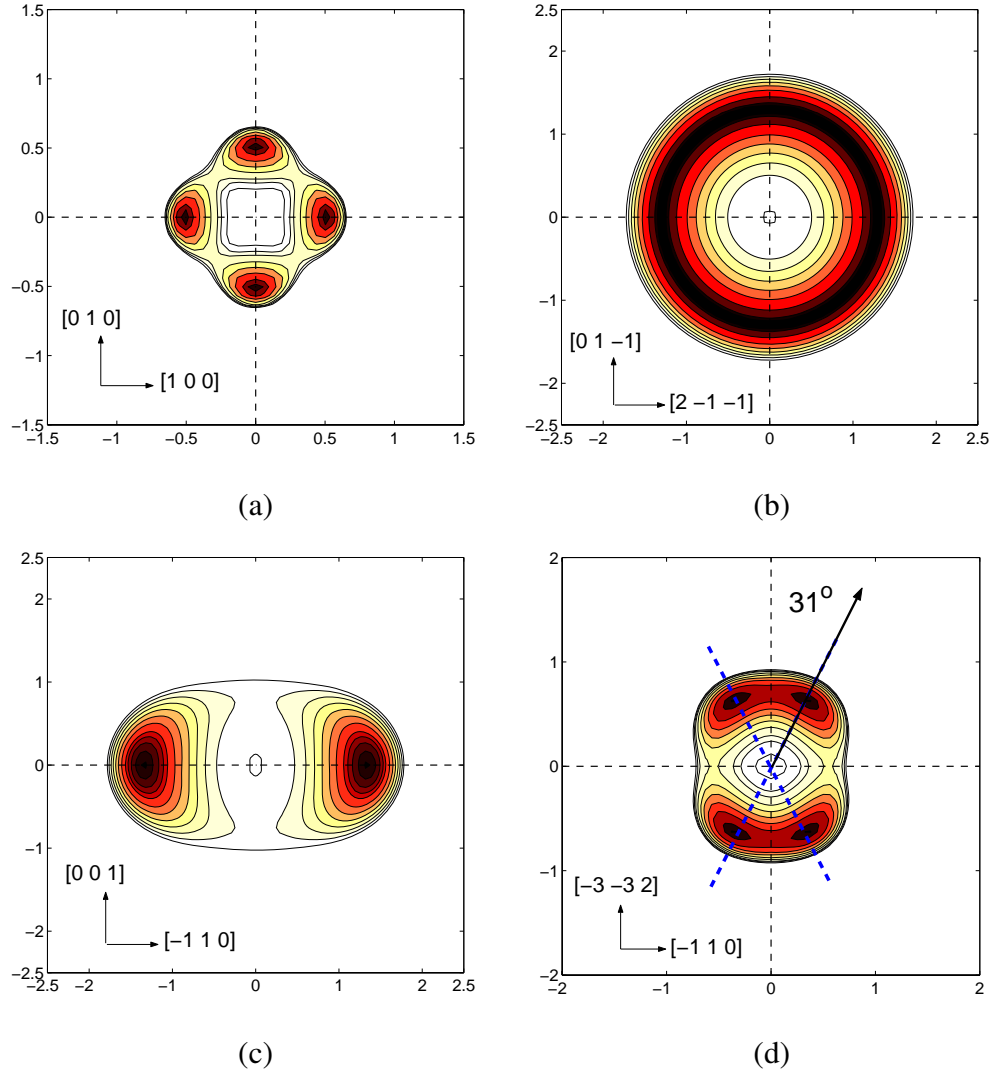
Figure 5.2: Contour plots of the initial growth rate with respect to the wave numbers in the $x_1 - x_2$ plane for Ge films on Si substrates of different crystal orientations. (a) Si(001) with x_1 and x_2 in the [100] and [010] crystal directions; (b) Si(111) with x_1 and x_2 in the $[2\bar{1}\bar{1}]$ and $[01\bar{1}]$ crystal directions; (c) Si(110) with x_1 and x_2 in the $[\bar{1}10]$ and [001] crystal directions; (d) Si(113) with x_1 and x_2 in the $[\bar{1}10]$ and $[\bar{3}\bar{3}2]$ crystal directions.
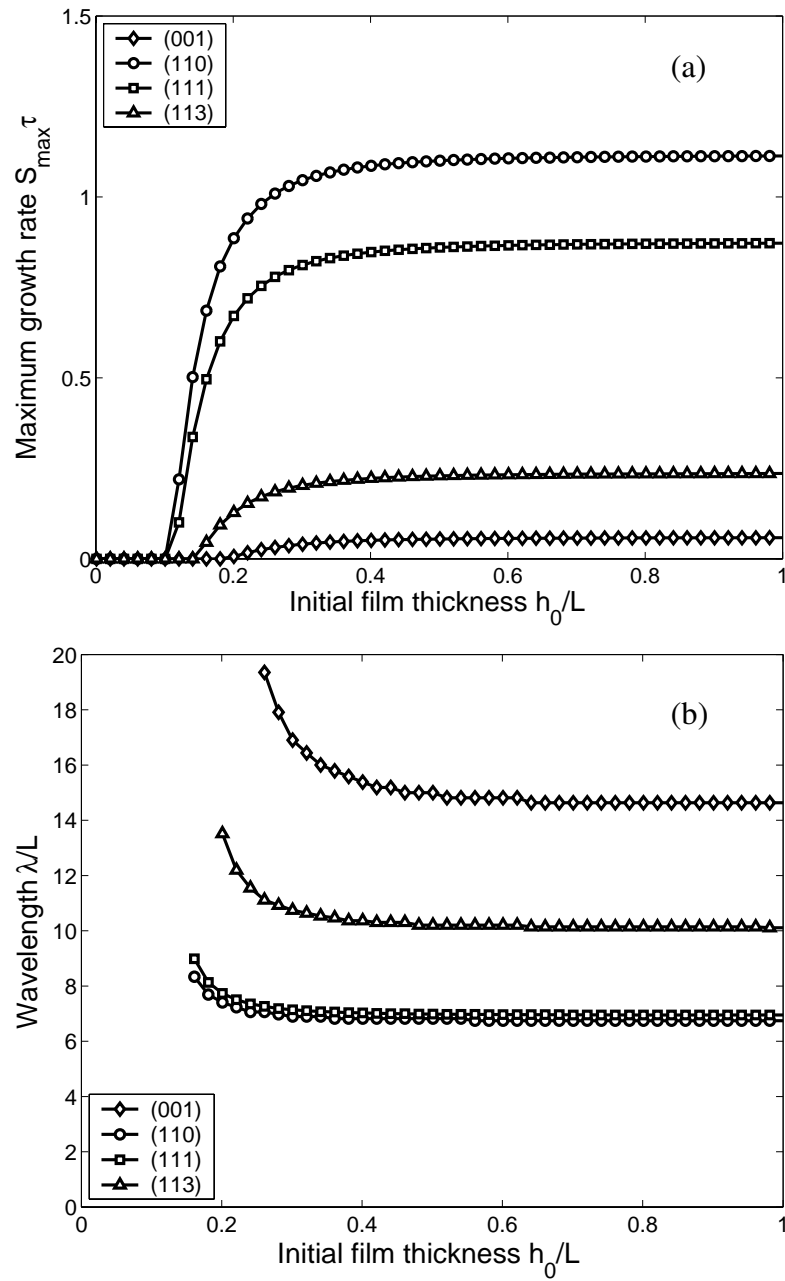
Figure 5.3: The maximum initial growth rate (a) and the corresponding wavelength (b) versus the average film thickness for Ge films on Si substrates of different crystal orientations. A critical thickness exists for each orientation, below which the growth rate is zero and the wavelength does not exist.

While the Si(001) has been the most commonly used substrate for SiGe epitaxy. Here we show that the surface evolution dynamics can be significantly different for epitaxial films on other orientations of Si. For Ge/Si(111) epitaxy (Fig.5.2(b)), the contours of the growth rate are nearly concentric circles, very similar to that for isotropic systems. This is not surprising as we notice that the triangular lattice structure on the Si(111) plane indeed leads to isotropic in-plane elastic properties. As a result, the early-stage surface evolution on Si(111) resembles that in an isotropic system, with the fastest growing modes in all directions, as predicted by the circle of the maximum growth rate in the contour plot; the radius of the circle gives the wave number of the fastest growth mode. For Ge/Si(110) epitaxy (Fig.5.2(c)), the contour plot shows two peaks of the growth rate on the axis parallel to the $[\bar{1}10]$ direction. This predicts growth of stripe patterns parallel to the [001] direction on the (110) surface. For Ge/Si(113) epitaxy (Fig.5.2(d)), there are four peaks in the growth rate contour, with corresponding wave vectors titled $\pm 31^o$ from the $[\bar{3}\bar{3}2]$ direction on the (113) surface. This is similar to the bifurcation of the growth mode due to anisotropic mismatch stresses in an otherwise isotropic system, as discussed in Chapter 4. Here, however, the bifurcation is a result of the combined effect of anisotropic mismatch stress and anisotropic substrate.

Figure 5.3 plots the peak growth rate and the corresponding wave length versus the mean film thickness. For each substrate orientation, there exists a critical thickness, below which the maximum growth rate is zero and thus the film is stable with a flat surface. The critical thickness varies slightly with the substrate orientation. For Ge on Si(001), $h_c = 0.18L \approx 0.7nm$, which is about 3-5 monolayers thick and agrees with experimental observa-

tions [19, 20, 120, 147, 148]. The predicted critical thicknesses for the other orientations are smaller: $h_c = 0.1L \approx 0.4nm$ for both Si(111) and Si(110), and $h_c = 0.14L \approx 0.55nm$ for Si(113). Supportive experimental data have been reported [43]. For a film with the mean thickness greater than the critical thickness, the maximum growth rate becomes positive and the flat film surface is unstable. The growth rate increases with the mean film thickness, and saturates for relatively thick films. Similar behavior was predicted for isotropic systems (Chapter 3), as a result of the wetting effect: the wetting potential suppresses the surface instability for thin films, but has little effect on the early-stage evolution for relatively thick films. Figure 5.3(b) shows the similar trend for the wave length of the fastest growing mode at the early stage. Only beyond the critical thickness, does there exist a dominant wavelength, which decreases with the mean film thickness and saturates for relatively thick films. Comparisons of the growth rates and wavelengths for different crystal orientations of the Si substrates in Fig.5.3 show an interesting trend. For a same mean film thickness, the Ge/Si(001) epitaxial system is the most stable among the four orientations, with the lowest growth rate, longest wavelength, and also the largest critical thickness. The epitaxial surfaces are increasingly unstable in the order of Ge/Si(113), Ge/Si(111), and Ge/Si(110). Interestingly, while the (111) surfaces of both Si and Ge have the lowest surface energy of all crystal orientations, the epitaxial Ge(111) surface on Si(111) substrate is less stable compared to the (001) and (113) surfaces. Apparently, the stability of the epitaxial surface is not controlled by the surface energy alone.

Evolution of the epitaxial surface morphology from numerical simulations are shown in Figs.5.4-5.7, for epitaxial Ge films on Si(001), Si(111),
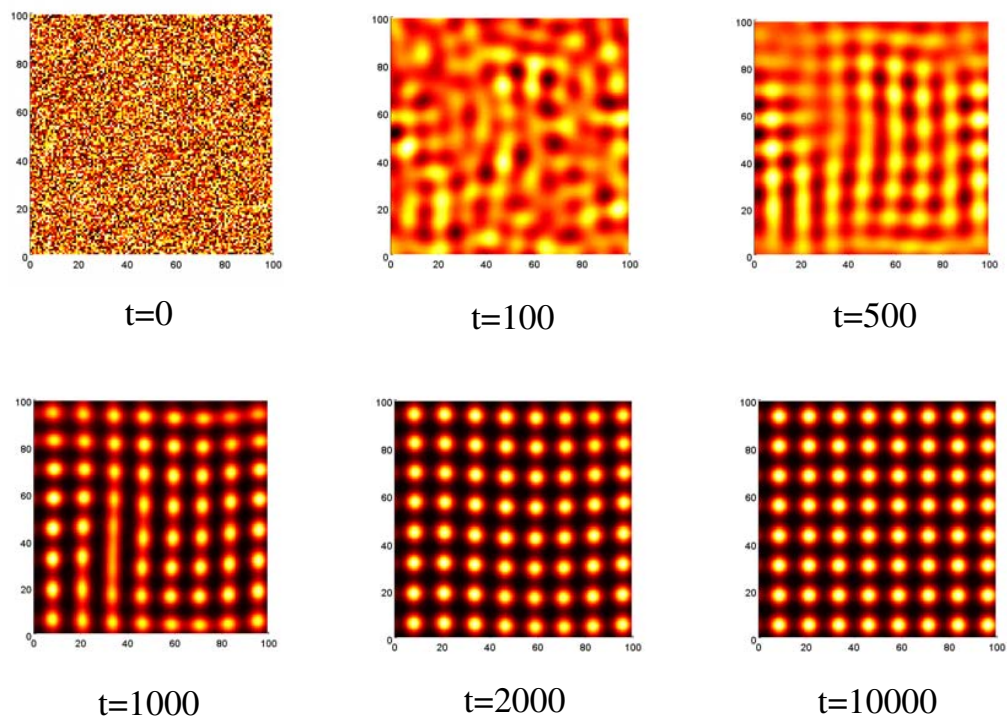
Figure 5.4: Simulated evolution of surface pattern for an epitaxial Ge film on a Si(001) substrate.

t=0   t=50   t=80

t=100   t=500   t=10000
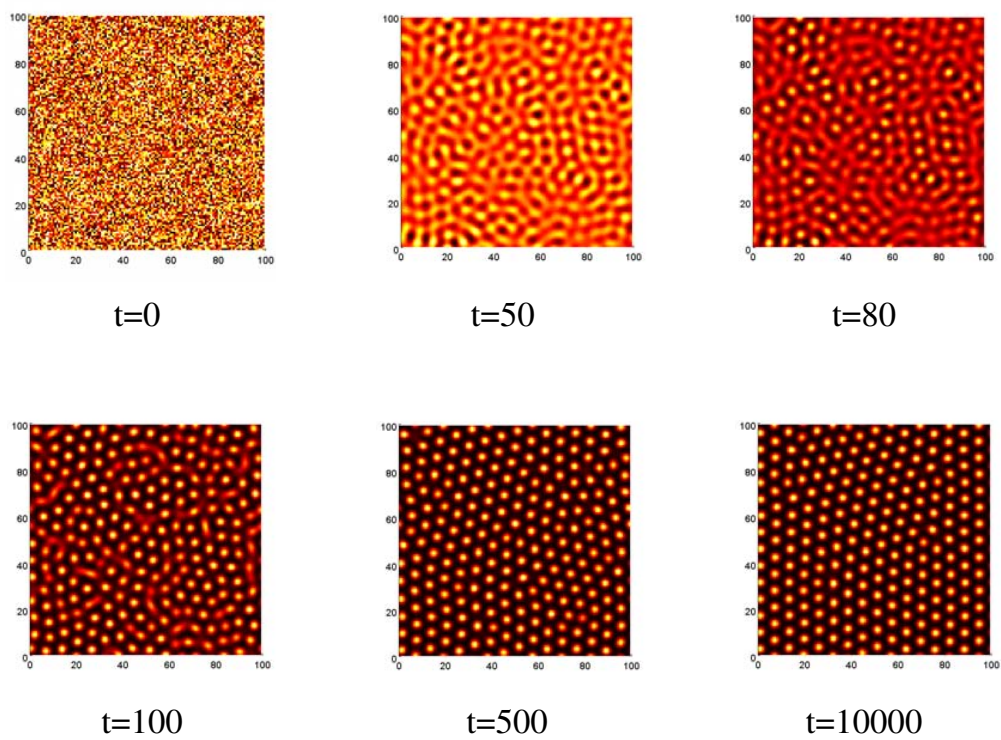
Figure 5.5: Simulated evolution of surface pattern for an epitaxial Ge film on a Si(111) substrate.

t=0   t=10   t=50

t=100   t=500   t=10000
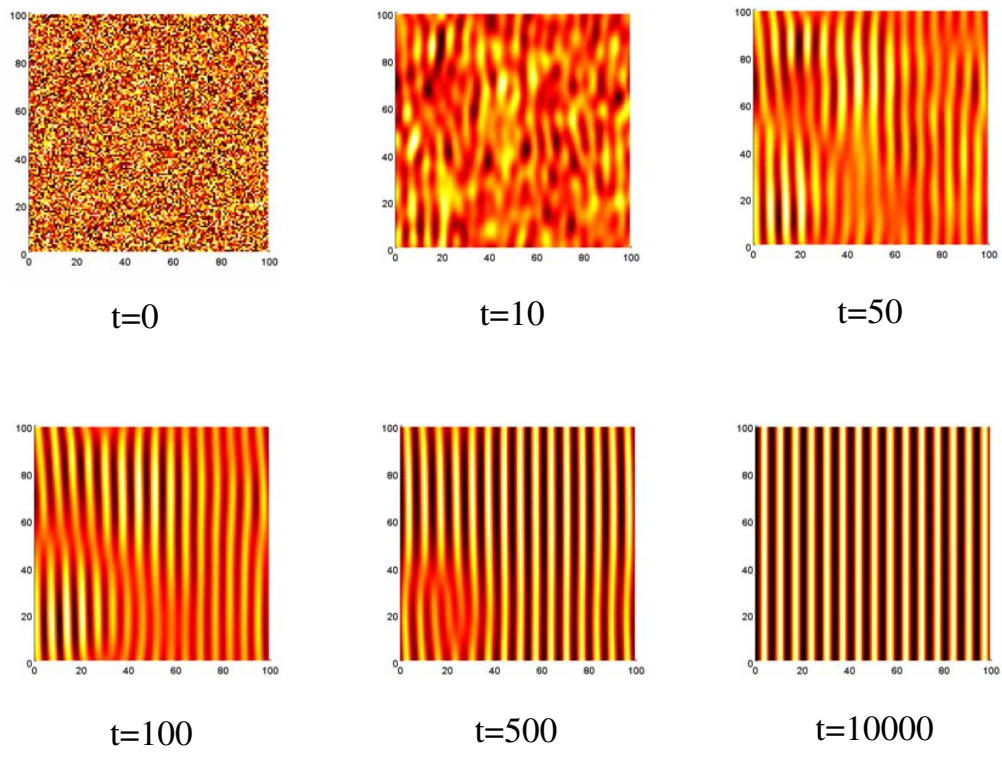
Figure 5.6: Simulated evolution of surface pattern for an epitaxial Ge film on a Si(110) substrate.
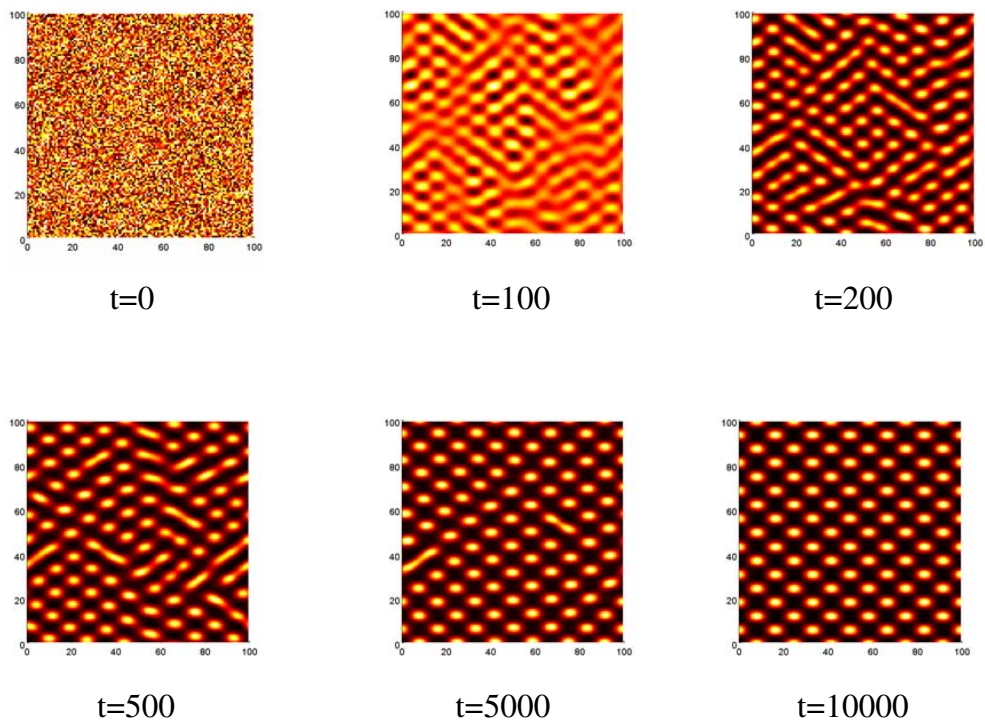
Figure 5.7: Simulated evolution of surface pattern for an epitaxial Ge film on a Si(113) substrate.

Si(110), and Si(113) substrates, respectively. The mean film thickness is: $h_0 = 1.2h_c$, where h_c corresponds to the critical thickness for each orientation. All simulations start from a randomly generated initial perturbation to the flat surface; the amplitude of the perturbation is 0.0001L. As predicted by the linear analysis, surface evolution at the early stage is dominated by the fastest growing modes. On the Si(001) substrate (Fig.5.4), the film surface first evolves into shallow ripples in both [100] and [010] directions. The initially interconnected ridges then break up into chains of islands. These islands are well organized, eventually forming a cubic array as a macroscopic replicate of the underlying cubic crystal structure. Apparently, the anisotropic elastic property effectively represents the cubic crystal structure and drives the ordering of the surface pattern. Similar evolution process occurs for the Si (113) substrate (Fig.5.7), where the initial ridges are aligned along two directions of angles $\pm 31^o$ off the $[\bar{1}10]$ direction and eventually the islands from a diamond pattern. For the Si(111) substrate (Fig.5.5), the early stage evolution shows similar surface patterns as that for isotropic systems, with shallow ridges and grooves growing in all directions. After a long-time evolution, however, discrete islands form and self-organize into a triangular array. Unlike the isotropic system, the anisotropic elastic property again reflects the triangular lattice of the cubic crystal on the (111) plane. While the early stage evolution is essentially isotropic, the anisotropic effect manifests over the long time evolution. For the Si(110) substrate (Fig.5.6), the film surface evolves from parallel ripples to self-assembled lines in the [001] direction.

Most experimental observations of Ge or SiGe films are on Si(001) substrates. Some reported arrays of self-assembled islands with no particular

ordering [19, 20, 22, 25, 87], while the others observed patterns of surface ripples and organized islands [21, 24, 26, 29, 31]. The results may depend on the detailed experimental conditions, but the physical origin for the different observations has not been well understood. The simulated surface evolution in Fig.5.4 compares well with experiments by Ozkan et al. [24] and Dorsch et al. [26], assuming similar patterns for SiGe films except for a change of the length scale. In particular, Dorsch et al. [26] observed surface ripples aligned in the <100> directions at the early stage and a transition to islands well aligned in the same directions, similar to the evolution sequence in Fig.5.4.

5.2.2 Effect of Ge concentration

For epitaxial SiGe alloy films, the evolution dynamics is similar except for the length and time scales. As defined in Eq.(5.6), the length scale depends on the mismatch strain, film and substrate moduli, and surface energy density, all varying with the Ge concentration x as given in Eqs.(5.2)-(5.4). The effects of elastic moduli and surface energy density on the length scale have been neglected in previous theoretical studies [68, 154], leading to a simple scaling, $L \propto 1/x^2$. However, as pointed out by Dorsch et al. [26], this scaling has to be corrected by considering the compositional dependence of the elastic moduli among other possible causes. The length scale plays an important role in the determination of the critical thickness and the dominant wavelength at the early stage. Figure 5.8 plots the critical thickness as a function of the Ge concentration for epitaxial SiGe films on Si substrates. Clearly, the critical thickness increases rapidly as the Ge concentration decreases, approaching infinity as $x \to 0$ for stable, homoepitaxial growth of Si. A few experimental

data [23, 137, 148, 155] are shown in Fig. 5.8 for comparison, all for SiGe films on Si(001) substrates. As mentioned earlier, one of these data has been used to determine the value of b in the present model. The agreement between the present model predictions and the other experimental data is reasonably good for a wide range of Ge concentration.

Figure 5.9 plots the wavelength of the fastest growing mode at the early stage of surface evolution in epitaxial SiGe films as a function of Ge concentration. This wavelength scales linearly with the length scale, but varies slightly with the crystal orientations of the substrates. It is noted that, while the wavelength is well above 1 μm for SiGe films with low Ge concentration (e.g., $x < 0.2$), the dominant wavelength is well below 100 nm for Ge-rich films with high Ge concentration (e.g., $x > 0.8$). The large variation in the length scale thus offers a potential approach to tunable surface patterns. Unfortunately, reliable experimental data is scarce for the early-stage evolution. Dorsch et al. [27] presented a detailed study on the morphological evolution during the growth of SiGe films of low Ge concentration ($0.05 \leq x \leq 0.15$), and their measurements for the wavelengths of the ripple patterns at the early stage are shown in Fig.5.9. The experimental data show a similar trend in the dependence on the Ge concentration, but are consistently lower than the present model predictions.

5.2.3   Effect of film thickness

Furthermore, it is found that the surface pattern depends on the mean film thickness. Figure 5.10 shows the surface patterns from numerical simulations of long-time evolution of Ge films on Si(001) substrates. When the mean
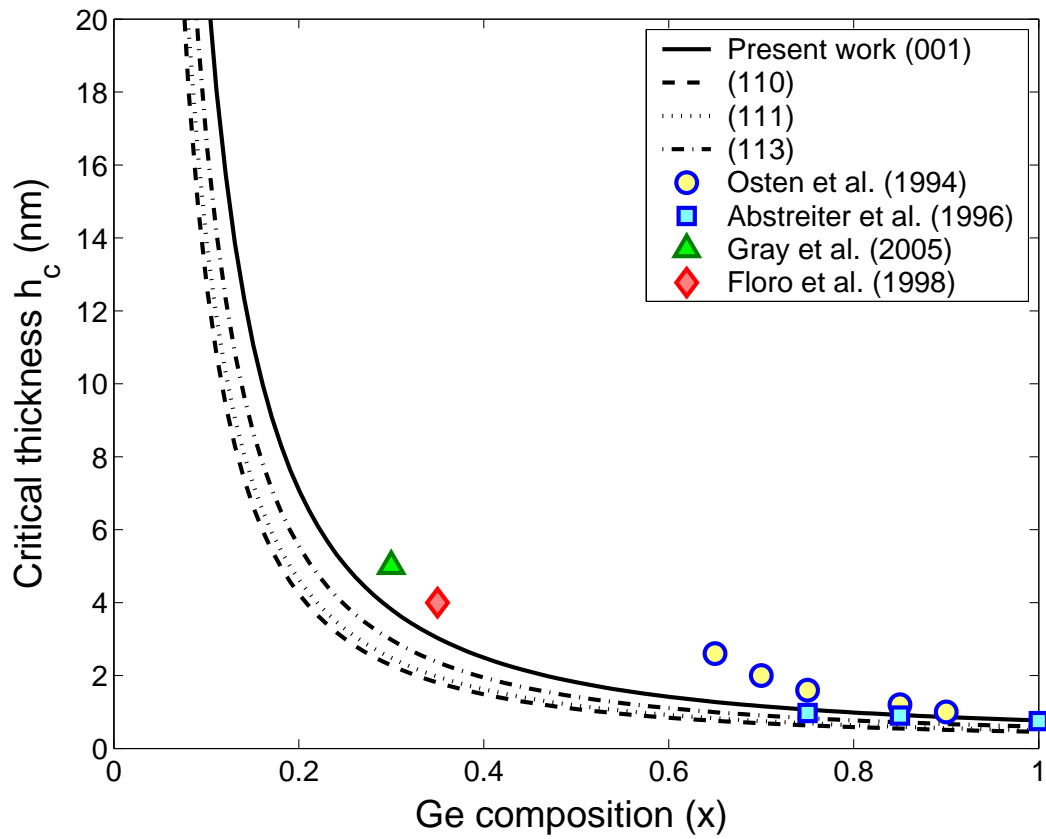
Figure 5.8: Comparison of the critical thickness predicted by the present study with previously published experimental data for SiGe films with varying Ge composition on Si substrates. All cited experiments are for Si(001) substrates.
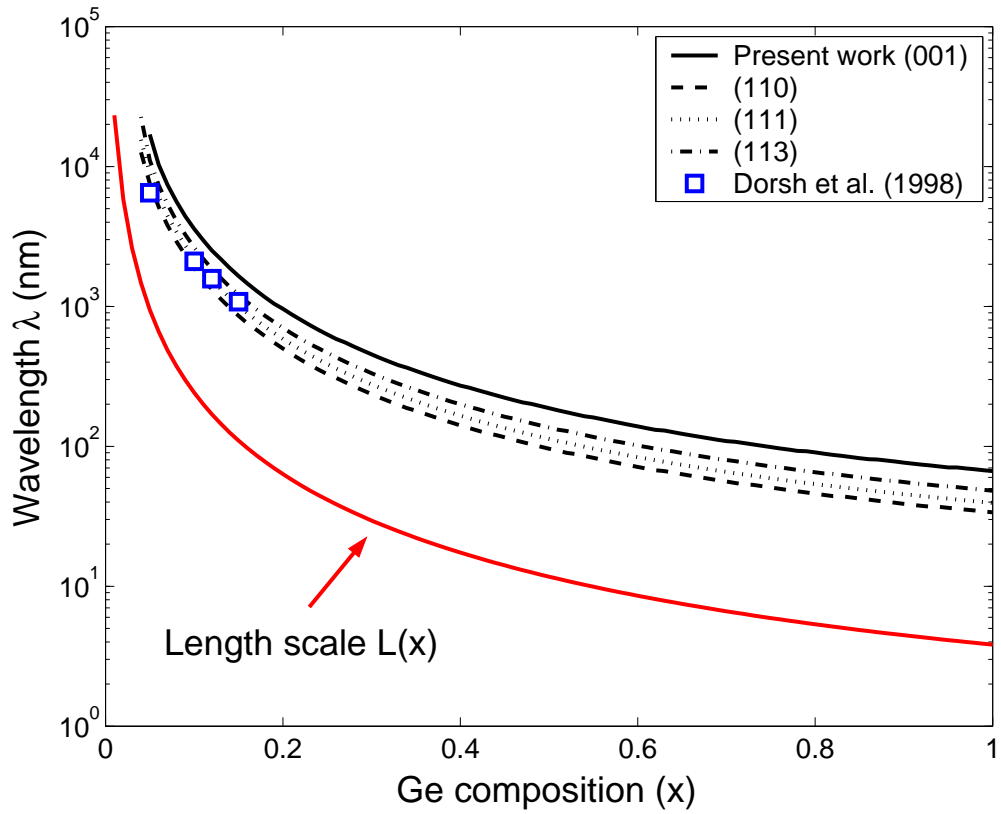
Figure 5.9: The wavelength corresponding to the fastest initial growth rate as a function of Ge composition for SiGe films on Si substrates. The experimental data from Dorsch et al. [26] are the measured wavelengths of surface ripples at the initial stage of epitaxial growth on Si(001) substrates. The length scaled defined in Eq.(5.6) is plotted for illustration.
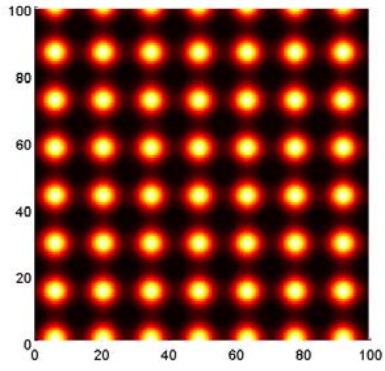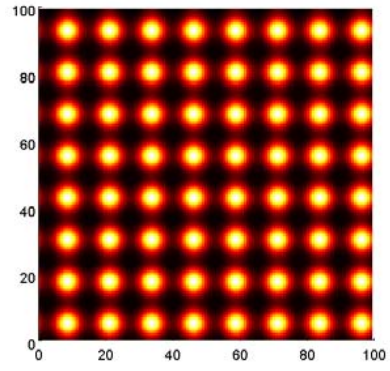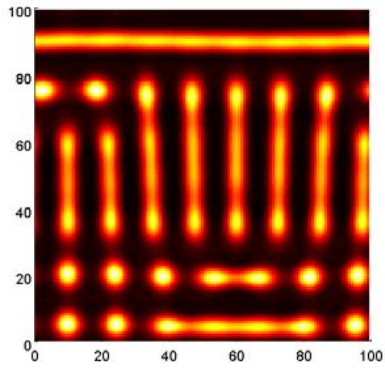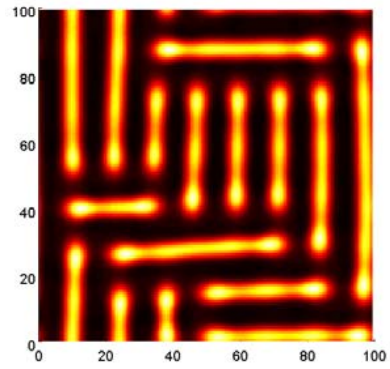
Figure 5.10: Surface patterns after long-term evolution for epitaxial Ge films of different average thickness on Si(001) substrates. (a) $h_0 = 1.1h_c$, (b) $h_0 = 1.2h_c$, (c) $h_0 = 1.4h_c$, (d) $h_0 = 1.5h_c$.
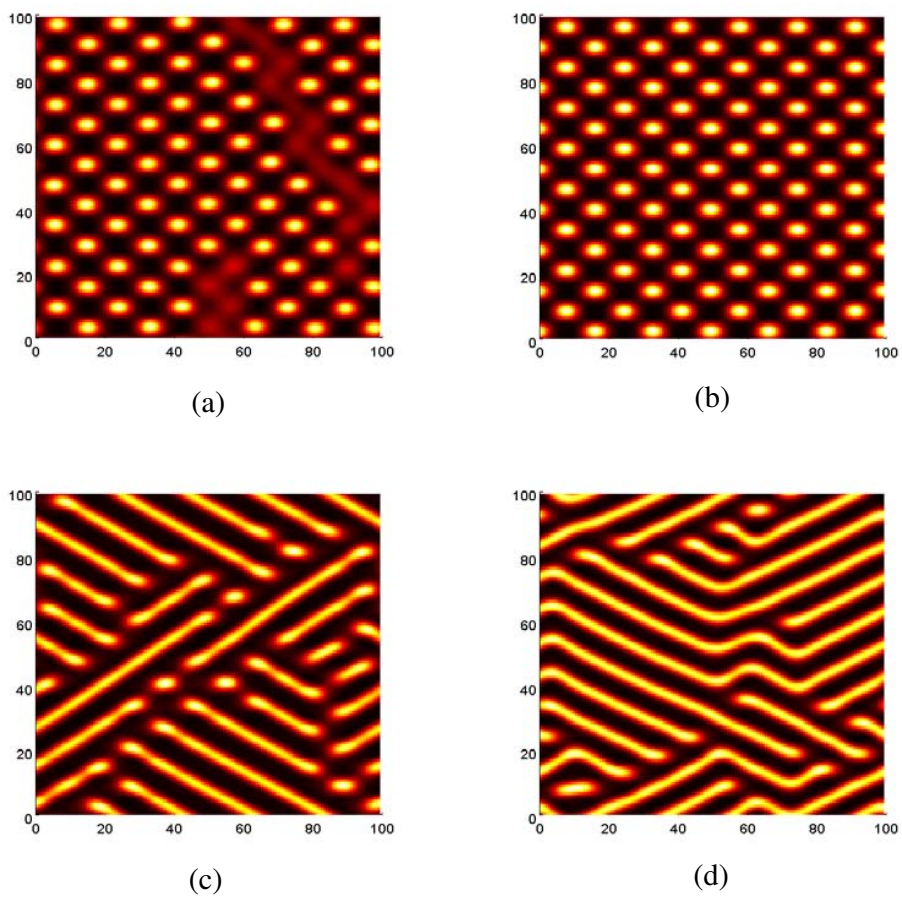
Figure 5.11: Surface patterns after long-term evolution for epitaxial Ge films of different average thickness on Si(113) substrates. (a) $h_0 = 1.05h_c$, (b) $h_0 = 1.1h_c$, (c) $h_0 = 1.25h_c$, (d) $h_0 = 1.5h_c$.

film thickness is slightly above the critical thickness ($h_0 = 1.1h_c$, Fig.5.10(a)), the islands form a cubic array. As the film thickness increases, the island array first becomes denser ($h_0 = 1.2h_c$, Fig.5.10(b)) and then connected ($h_0 = 1.4h_c$, Fig.5.10(c)). Further increase of the film thickness leads to a surface pattern with perpendicular lines in the <100> directions ($h_0 = 1.5h_c$, Fig.5.10(d)). Similar transition of the surface pattern from dots to lines has been observed experimentally [21, 28, 31, 50, 155, 156].

A few recent experiments have reported epitaxial growth of Ge on high-index Si substrates including Si(113) [47, 48]. It was observed that Ge islands are shaped like wires along the [$\bar{3}\bar{3}2$] direction. However, the numerical simulation with the present model predicts a diamond pattern of island array (Fig.5.7). Increasing the mean film thickness in the numerical simulation predicts a transition of the dot-shaped island array to a line-shaped pattern (Fig.5.11), but the lines are aligned along two directions of angles $\pm31^o$ off the [$\bar{1}10$] direction. This discrepancy indicates possible contributions on the pattern evolution from other physical origins (e.g., surface steps), in addition to the elastic anisotropy considered in the present study.

To our knowledge, no experimental observations have been reported for epitaxial surface evolution of SiGe or Ge films on Si(111) or Si(110) substrates. As predicted by the present numerical simulations, the triangular array of islands on Si(111) (Fig.5.5) and the parallel lines on Si(110) (Fig.5.6) may be attractive for practical applications in microelectronics and optoelectronics, thus worthwhile for further investigations with experimental efforts.

5.3 Self-assembled silicide nanostructures

5.3.1 Rare-earth metal silicides

Tremendous interest has been recently generated in self-assembled nanowires (SANWs) formed by epitaxial growth of rare-earth (RE) metals on silicon substrates. These one-dimensional nanostructures have metallic conduction and extremely low Schottky-barrier ($< 0.5eV$). These unique features make them attractive for applications as low-resistance interconnects or nanoelectrodes for electrically active nanostructures [157–159].

The very early work given by Preinesberger et al. [54] shown the formation of long, narrow Dy wires self-assembled on Si(001). Lately, Chen et al. [55] presented similar wire-like islands self-assembly for Er on Si(001), and, by using the Scanning Tunneling Microscopy (STM), they investigated the surface structures and presented that the nanowires have the same crystalline structure and orientation relative to the substrate, which indicates that continuous ErSi$_2$ thin films grown on Si(001). Following that, Chen et al. [160] studied other kinds of RE silicides (ErSi$_2$, ScSi$_2$, GdSi$_2$, and DySi$_2$) grown on Si(001), and illustrated that the epitaxial SANWs can be produced if the magnitude of the lattice mismatch between the silicide layer and the substrate is large along one of the crystal epitaxy axis and small along the perpendicular axis. More recently, to achieve better control of the orientations of SANWs, RE silicides grown on Si(110) and Si(111) have been reported [56, 57] to produce orientated SANWs aligning in specific directions.

It is generally agreed that the formation of silicide SANWs is due to lattice mismatch anisotropy between the silicides and the Si substrate. When
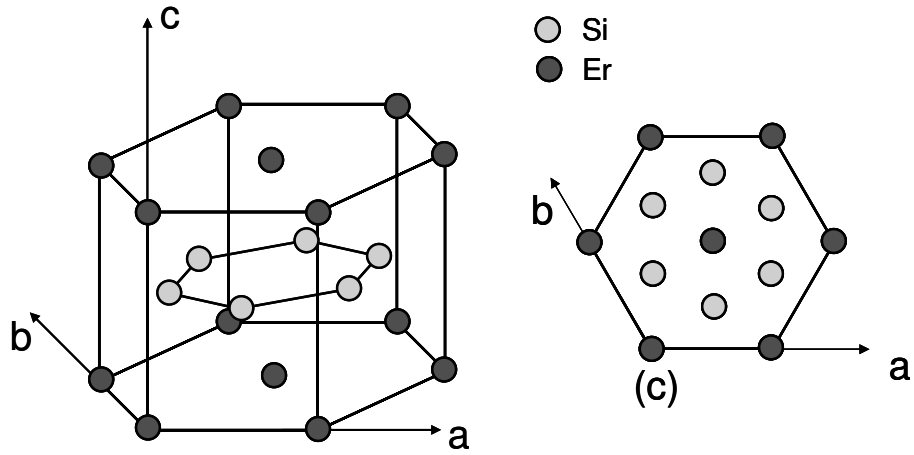
Figure 5.12: Spatial and 2D model of hexagonal ErSi$_2$ silicide unit cell.

the RE metals are deposited onto the Si substrate, metal silicides are formed through the nucleation-determined chemical reactions between the RE metal and Si atoms. RE silicides crystallize in three types of sturctures: hexagonal, tetragonal, and orthorhombic [53, 161, 162]. The hexagonal phase are always dominant and can coexist with other two phases [53, 58, 161–163]. Fig.5.12 and Fig.5.13 show the hexagonal and tetragonal unit cell of RE silides, respectively, and orthorhombic has the similar structure with tetragonal. The hexagonal silicides epitaxially growing on Si are subject to an anisotropic lattice mismatch, with a relatively large mismatch in the [0001] axis aligned with one of the <110> axes of the substrate, and with a relatively small mismatch in the perpendicular direction, [11$\bar{2}$0], aligned with the other <110> axis (Fig.5.14) [53, 58, 100, 164]. The mismatch strain for common silicides are listed in Table 5.2. With the increasing of coverage, 2D-3D transition happens through the Stranski-Krastanov growth mode, and self-assembled nanowire pattern forms. These nanowires are observed to grow along [11$\bar{2}$0] , which can usually exceed

104
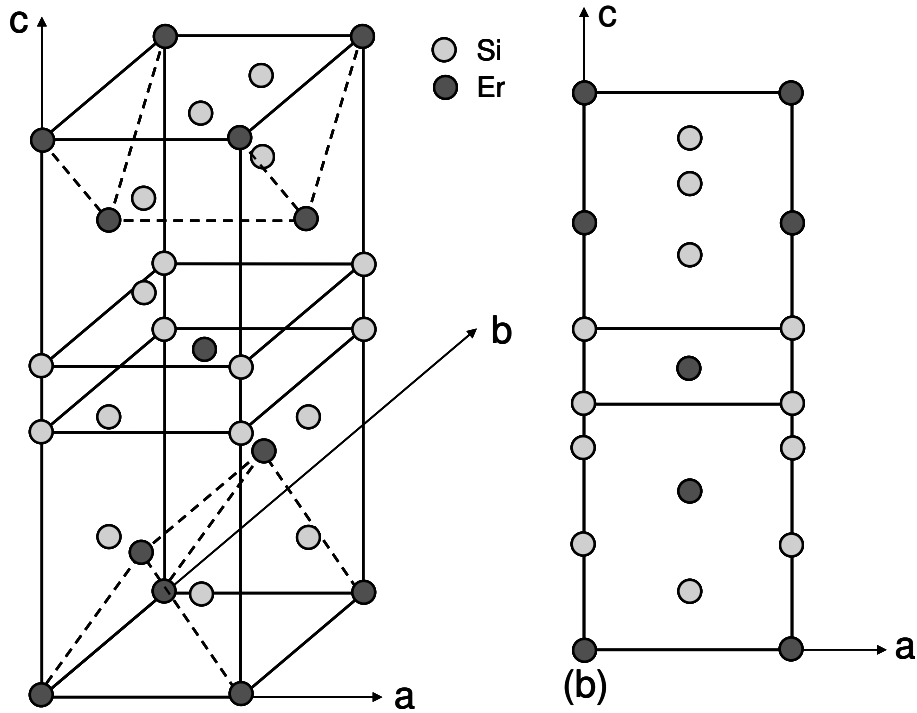
Figure 5.13: Spatial and 2D model of tetragonal ErSi$_2$ silicide unit cell.

1000$\mathring{A}$ in the length, and is constrained from growing along [0001] [56, 58]. In addition to nanowires, compact shaped islands are usually formed concomitantly with respect to these wires, depending on the detailed growth conditions [161–165]. This is believed due to the existence of tetragonal phase silicides. The tetragonal crystal structure has identical lattice spacing for a and b axis, and epitaxially grows on Si(001) with a and b axis aligned along the two orthogonal <110> directions, which leads to an epitaxial layer with the same mismatches in both directions [53, 58, 161, 162, 166]. Fig.5.15 schematically shows the tetragonal phase silicides epitaxy on Si(001).

In this section, we will investigate the self-assembly of RE silicides on Si with both hexagonal and tetragonal structures, and surface Si(001) is adopted
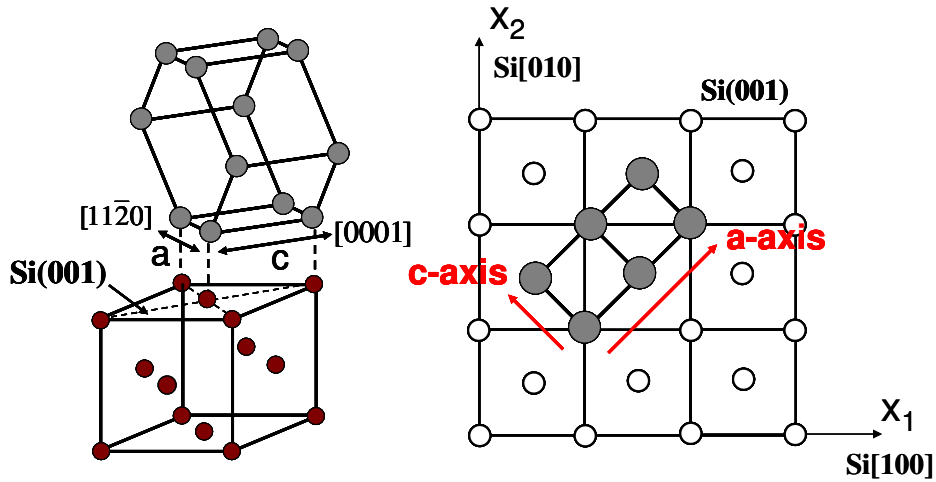
Figure 5.14: Schematic of hexagonal phase silicide epitaxy on Si(001).

Table 5.2: Lattice mismatch of hexagonal phase rare-earth metal silicides on Si(001)

$Silicides$	$ErSi_2$	$DySi_2$	$ScSi_2$	$GdSi_2$	$HoSi_2$
$[0001]mismatch$	6.5%	7.6%	−4.6%	8.9%	6.8%
$[11\bar{2}0]mismatch$	−1.3%	−0.1%	0.8%	0.8%	−0.75%

in our discussion.

5.3.2   Self-assembly of silicide nanowires

Consider a flat silicide layer with mean thickness h_0 epitaxy on a Si(001) substrate. An in-plane biaxial mismatch strain in the silicide film is obtained by comparing the lattice parameters of the silicides and the Si substrate. With respect to the base coordinate system of the substrate, a corresponding coordinate system is set up, with x_1 along the Si[100] direction and x_2 along the Si[010] direction, as shown in both Fig.5.14 and Fig.5.15. At the reference
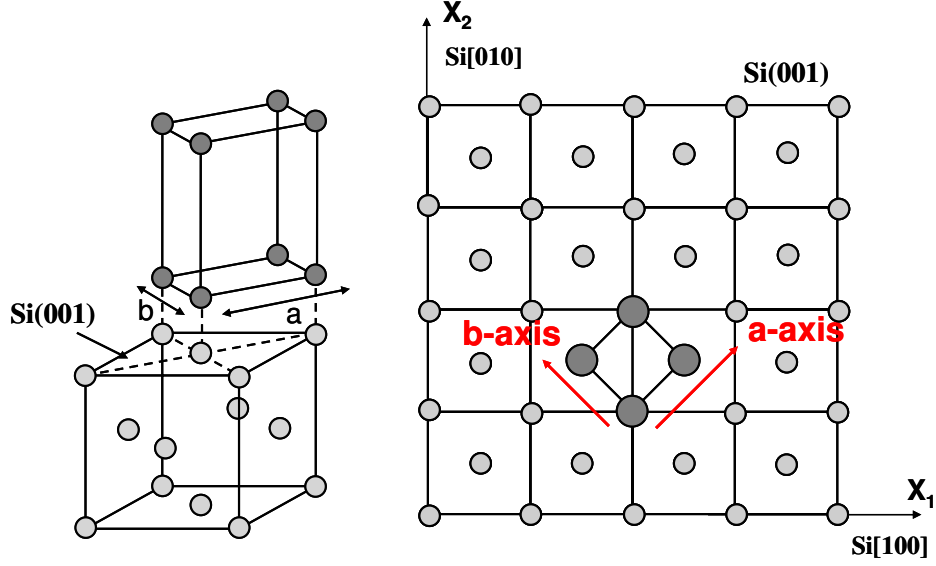
Figure 5.15: Schematic of tetragonal phase silicide epitaxy on Si(001).

state, the mismatch stresses can be calculated referring to the procedures in Chapter 2. It should be noted that, the alignment of base coordinate axis of the silicides is different from that of the Si substrate, and a transformation of the hexagonal elastic constants is necessary prior to subsequent calculation. Details about the transformation can be referred to Appendix B.

For both the hexagonal and tetragonal structures, because of the existence of Si vacancies, real silicide structures are approximately $(RE)Si_{1.7}$ [167, 168]. For simplicity, in the present work, we will refer to all the silicide structures as $(RE)Si_2$, and the elastic moduli of RE silicides are evaluated by simple linear mixing rule between RE and Si, namely

$$C_{ijkl}^{(RE)Si_2} = (1-x)C_{ijkl}^{(RE)} + xC_{ijkl}^{Si}, \qquad (5.8)$$

Table 5.3: Elastic constants for typical rare-earth metals and silicon

Substance	Elastic Constants (GPa)					
	$C_{11}(C_{22})$	C_{12}	$C_{13}(C_{23})$	C_{33}	$C_{44}(C_{55})$	C_{66}
Er	83.7	29.3	22.2	84.5	27.5	27.2
Dy	73.1	25.3	22.3	78.1	24.0	23.9
Gd	66.1	25.0	20.8	71.4	20.4	20.6
Ho	76.1	24.8	20.6	77.6	25.7	25.7
Si	166.2	64.4	64.4	166.2	79.8	79.8

Table 5.4: Surface energy density for typical rare-earth metals and silicon

substance	$\gamma(N/m)$	$Temp(^0C)$	$d\gamma/dt(N/(m \cdot K))$
Er	0.637	1530	-0.12e-3
Dy	0.648	1500	-0.13e-3
Gd	0.664	1350	-0.58e-4
Ho	0.650	1500	-0.125e-3
Si	0.775	1410	-0.145e-3

with $x = 2/3$. The elastic moduli for typical RE metals are listed in Table 5.3.

Upon annealing, the flat surface starts to evolve, and following the discussion in Chapter 2, the governing equation is derived taking the form of Eq.(2.19). Both linear and nonlinear are performed with the same procedure presented in the previous part for SiGe on Si system.

To be specific, the RE metal Er on Si(001) is investigated first. For the hexagonal structures, the [0001] axis of ErSi$_2$ is aligned along the Si[1$\bar{1}$0] axis and the [11$\bar{2}$0] axis along the Si[110] axis (Fig.5.14). Two mismatch strains aligning in the $a-$ and $c-$axis can be transformed into current system

by standard tensor transformation, and the mismatch stresses are calculated referring to Chapter 2. The physical constants used in simulations are listed in Tables 5.2-5.4, for the lattice mismatch, elastic constants, and surface energy density, respectively.

By doing the linear analysis, a similar length scale and time scale are defined as

$$L = \frac{\gamma_f \overline{E}_s}{2(3\overline{\epsilon}_m \overline{E}_f)^2}, \tau = \frac{\gamma_f^3 \overline{E}_s^4}{16\Omega^2 M (3\overline{\epsilon}_m \overline{E}_f)^8}, \qquad (5.9)$$

where $\overline{\epsilon}_m$ refers to the mean mismatch normal strains in Si[100] and Si[010] directions, i.e., $\overline{\epsilon}_m = \frac{1}{2}(\epsilon_{11}^{(0)} + \epsilon_{22}^{(0)})$, and other parameters are defined the same as those of Eq.(5.6). Compare with Eq.(5.6), coefficients are adjusted for the purpose of numerical stability.

Fig.5.16 plots the growth rate in the plane of wave vector. The fastest growing mode corresponds to two points located on the $[\bar{1}10]$ axis, which is the direction with a large mismatch. This suggests that the initial evolution would develop parallel stripe patterns perpendicular to $[\bar{1}10]$ direction. Fig.5.17 shows surface evolution from the nonlinear numerical simulation for ErSi$_2$ on Si(001). As predicted by the linear analysis, a parallel stripe pattern emerges at the early stage in the [110] direction. After long time evolution, regular parallel lines are formed aligning in the [110] direction. Good agreements are presented compare the simulation results with experimental observations for both the pattern shape and their orientation.

Now we looking at the tetragonal ErSi$_2$ structures, with which the a and b axis of ErSi$_2$ are aligned along the two orthogonal Si(110) axis, with identical mismatch strain (Fig.5.15). The growth rate is shown in Fig.(5.18).
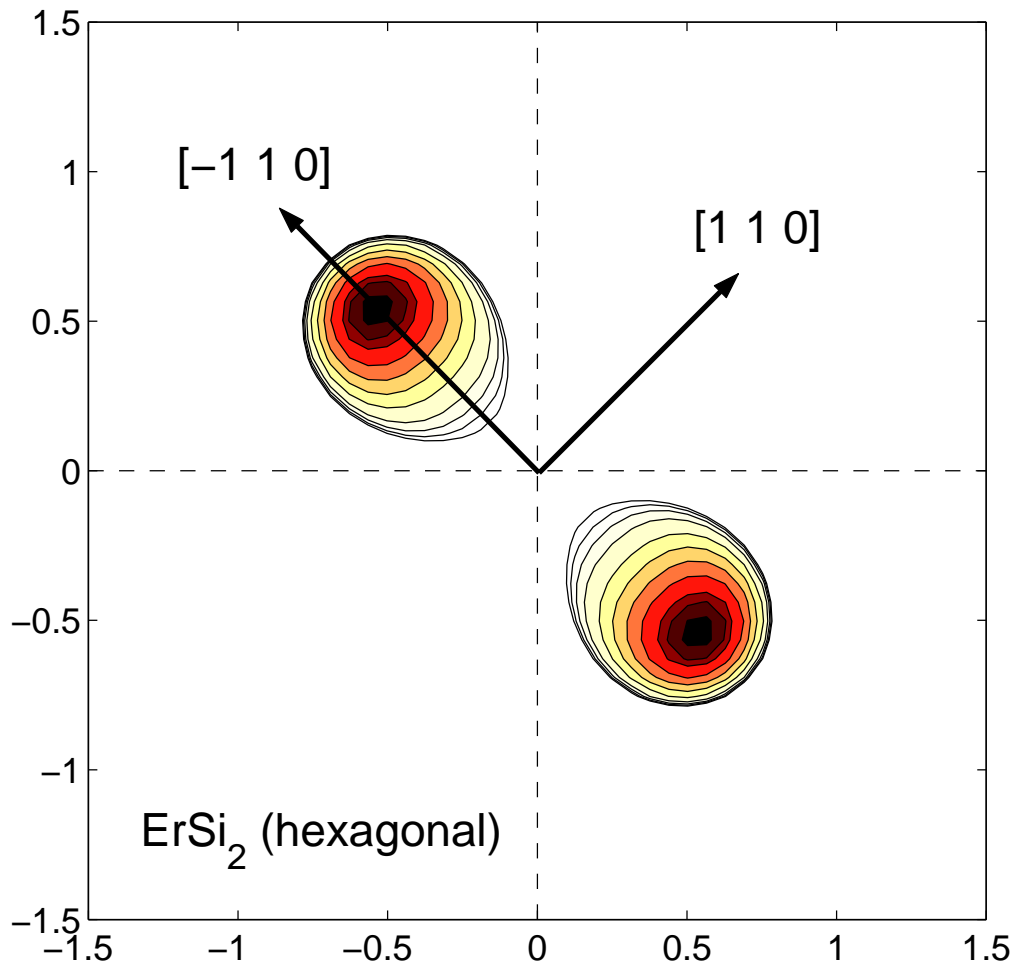
Figure 5.16: Contour plots of the growth rate $s(k_1, k_2)$ for hexagonal $ErSi_2$ on Si(001). Dark points indicate the peaks, which is located in $[\bar{1}10]$ direction.
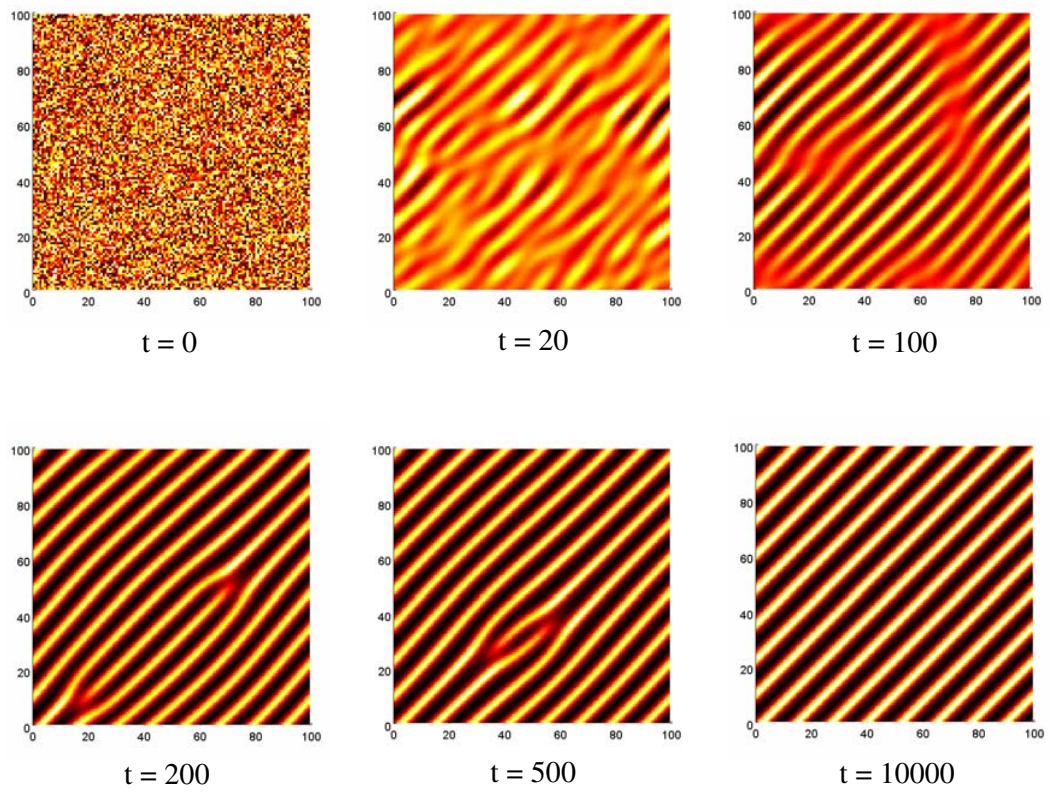
Figure 5.17: Evolution of surface morphology for hexagonal ErSi$_2$ on Si(001) from the numerical simulation. Parallel lines are eventually formed in the [110] direction.
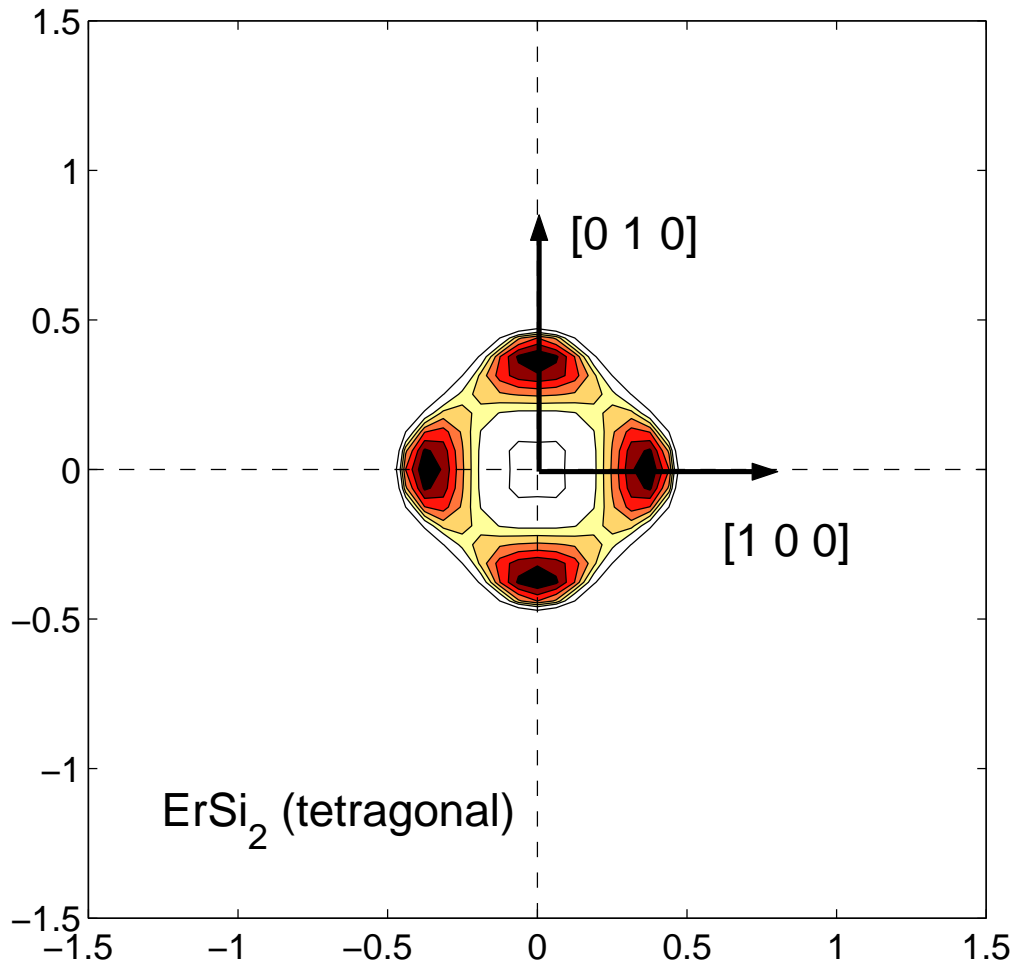
Figure 5.18: Contour plots of the growth rate $s(k_1, k_2)$ for tetragonal $ErSi_2$ on Si(001). Four dark points indicate the peaks, which is located in [100] and [010] directions.

t = 0 t = 200 t = 300

t = 500 t = 1000 t = 10000
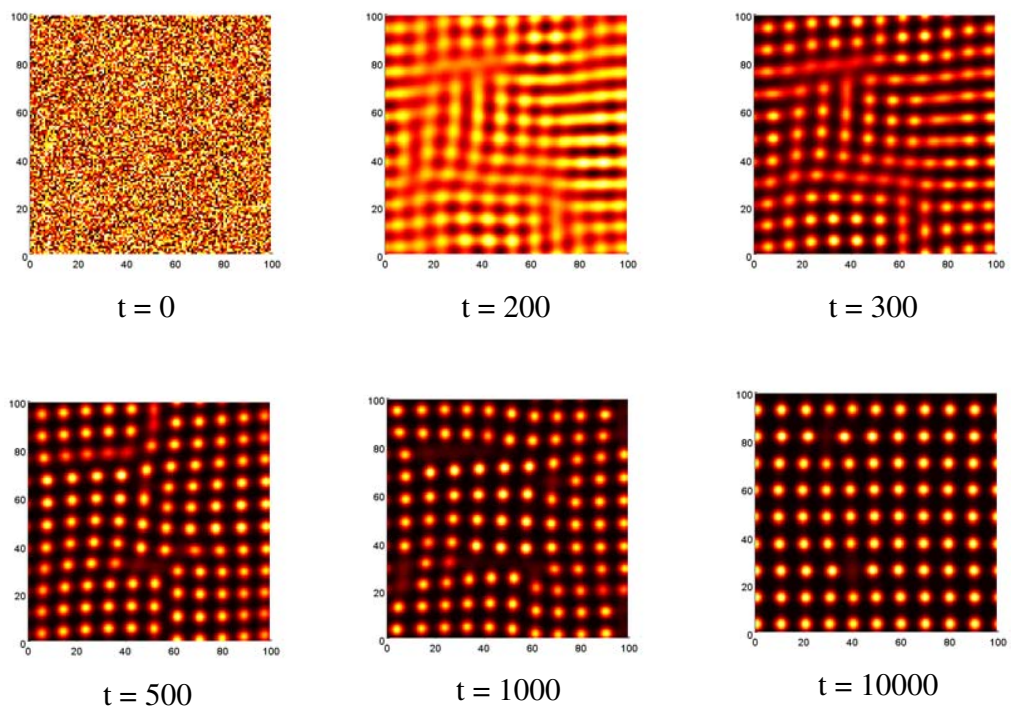
Figure 5.19: Evolution of surface morphology for tetragonal ErSi$_2$ on Si(001) from the numerical simulation. Compact dots are eventually formed.

In a diamond shaped region, the growth rate is positive, with four peaks located on the [100] and [010] axis. This indicates the initial evolution will form perpendicular ridges in [100] and [010] directions. Fig.5.19 shows the evolution of surface morphology by nonlinear simulation. The film surface evolves into orthogonal ripples in both [100] and [010] directions as predicted. The ridges then break up into islands, and, after long time evolution, form into well organized array. No any elongated islands are obtained for this situation. These regular islands also reflect the underlying crystal structure of Si(001), which is similar with the situation for Ge on Si(001). This can be explained by the isotropic strain (stress) state of the silicide thin film. Elastic anisotropy from the substrate dominates the surface evolution for this system.

Combination of the results from both the hexagonal and tetragonal silicide epitaxy investigation supportively illustrates that, in real RE silicide on Si system, the hexagonal structured silicides tend to form elongated islands aligning in the direction with small mismatch, while the tetragonal structured silicides can only form compact islands. Coexistence of both two structures offers a mixed pattern with both lines and dots. One thing need to mention is that, different from the presented simulation results here, instead of lines grown in a unique direction, orthogonal lines are commonly observed in experiments. This phenomenon has been attributed to several reasons. The existence of different surface terraces of the substrate could be one of them [53–55, 166, 169]. One type of terrace has dimmer rows parallel to the step edge, while the other type has dimmer rows perpendicular to the step edge. Thus the lines formed on the surface are tend to align in two perpendicular directions. Equal possibilities for hexagonal silicides with a- or c-axes lying in any one of the

114

<110> directions may also cause the generation of orthogonal lines.

5.4   Summary

In summary, we have studied the pattern evolution mechanism for heteroepitaxial film on anisotropic substrates, specific in two cases: SiGe islands on Si substrates and disilicide nanostructures on Si substrate. The effects of elastic anisotropy have been discussed in the early growing stage and during long time evolution. Numerical simulations show that anisotropic elastic field dominantly controls the evolution and formation of surface patterns. For SiGe situation, the theoretical results are corroborated experimentally to check the pattern variation with respect to surface orientation, pattern scaling determined by film composition and the film thickness effects on evolution. For disilicide case, results support that anisotropic mismatch strain is the reason for breaking the symmetry and forming elongated islands, which aligns in the direction of small mismatch strain. Good agreement of our simulations with experimental results for both cases serves a theoretical pathway for nano scale pattern tailoring in heteroepitaxial thin film growth.

Chapter 6

Conclusions and Outlook

In this dissertation, the pattern evolution process for epitaxial thin film on single crystal substrate is discussed by a nonlinear model. Both linear analysis and nonlinear numerical simulations are performed to investigate the effects of nonlinear energy components and system anisotropy in self-assembled surface pattern formation. Some general conclusions can be drawn with respect to several aspects.

At the initial stage of self-assembly, stress field energetically competes with the surface energy, stimulates the surface instability, and triggers the surface evolution. After a long time evolution, different scenarios can happen depend on weather the nonlinear stress field is included or not: without nonlinear stress terms, overall pattern remains unchanged with the roughness of surface growing; when the nonlinear stress components are considered, the film surface develops the "blow-up" instability by forming the deep circular grooving like "nanopits". So, without the wetting energy along the interface, for relatively thick film, nonlinear stress field can induce surface instability by

energy relaxation.

For SK growth mode, the wetting energy from the interface plays an important role in surface dynamics. The presence of both nonlinear stress field and wetting energy favors a stable evolution and organization of self-assembled islands, leaving a thin uniform wetting layer along the interface.

Real epitaxial systems are essentially anisotropic. Considering only the anisotropic mismatch stress can break the generic symmetry of an otherwise isotropic system, and, in addition to that, predict a bifurcation of surface pattern. Consideration of anisotropic mismatch stress enriches the surface dynamics and offers a way for pattern selection.

For the SiGe/Si system, the anisotropy in both the surface and bulk properties has profound effects on the nonlinear dynamics of pattern evolution. With the surface energy anisotropy neglected, ordered surface patterns form under the influence of elastic anisotropy, and they correlate well with the underlying crystal structures of the substrate. Variation in the Ge composition of SiGe films are found to lead to a change of the characteristic length scale and thus the feature size of the final pattern. Furthermore, a transition of the surface pattern from discrete islands to interconnected lines can be achieved by increasing the mean film thickness.

For RE silicides epitaxy on Si(001), elongated silicide nanowires are formed due to anisotropy of lattice mismatch strain between the silicides layer and the substrate. The strong mismatch strain breaks the symmetry and form elongated "wires" aligning in the direction of small mismatch strain.

In conclusion, the interplay between the nonlinear stress field and the interfacial wetting has a profound effect on the dynamics of surface evolution.

117

Further consideration of anisotropy can give a much richer dynamics of surface pattern, and, in principle, may offer some instructions for epitaxial thin film self-assembly for further applications.

Of course, materials discussed so far are by no means complete, and the science of self-assembly growth is still developing. Even for the well-studied SK growth mode, a lot of work remains to be done using crystal growth kinetics and energetic to achieve a better control over the pattern nucleation, size, composition, and uniformity. These unsolved issues are challenging and at the same time very interesting.

As mentioned in Chapter 4 and 5, current evolution model is far from completion, and can be further complicated by involving other kind of anisotropy, such as anisotropic surface dynamics, anisotropic surface energy, and in turn anisotropic wetting energy. Some tries have been reported mostly with anisotropic surface energy in recent years [96, 104–106], and the rest issues remain to be tackled. The reason for that is because of the lacking of acceptable models to give plausible description for these features both mathematically and physically.

Another issue related to the pattern control is some artificially design approach, such as strain field templates. The strain effect on SK growth has inspired research activities aiming to improve the uniformity of self-assembled nanostructures by strain engineering [35, 39, 170–176]. Qualitatively it is not difficult to speculate that a non-uniform strain field on the substrate surface would provide a modulated energy landscape that drives migration of adatoms on the surface and thus nucleation and growth. Under proper conditions, the regulation of the strain field may overrule the randomness of nucleation sites

at the atomistic scale, leading to ordering and uniformity. The difficulties however lie on the experimental realization of particular strain patterns and a quantitative understanding of how a non-uniform strain field interacts with the growth of self-assembled patterns. Several techniques have shown promise in controlling the strain field. The effectiveness in terms of improving the spatial and size uniformity varies, and the current practice is essentially trial-and-error with little knowledge on why and how to improve. To this end, it is critical to develop a quantitative model, based on which a mechanistic approach may proceed to more effectively control the synthesis of self-assembled patterns.

Appendix A

Solutions to Linear Elastic

Half-Space Problems

A.1   Isotropic solution

The classical approach to finding stress and displacement solutions due to tractions acting on the surface area can be traced back to Boussinesq [177] and Cerruti [178]. They employed the potential to get components of displacement and stress for a distributed normal and tangential load over the surface on an elastic half space, respectively. The results are given in terms of the integrals of the loading distribution over the area. Hence, if the distributed loading within the area are known explicitly, the solutions at any point in the solid can be found by evaluating the integrals. To be specific, for a concentrated normal force acting on the surface of a half plane with no body force.

Boussinesq's solution gives the displacements on the surface:

$$u_r = \frac{1-2\nu}{4\pi\mu}\frac{p_z}{r}, u_z = \frac{1-\nu}{2\pi\mu}\frac{p_z}{r}. \tag{A.1}$$

Thus, the surface displacements due to a distributed pressure, $p(x,y)$, are evaluated in the integral form:

$$u_x(x,y) = \frac{1-2\nu}{4\pi\mu} \int\int \frac{(x-\xi)p(\xi,\eta)}{(\xi-x)^2+(\eta-y)^2}d\xi d\eta, \tag{A.2}$$

$$u_y(x,y) = \frac{1-2\nu}{4\pi\mu} \int\int \frac{(y-\eta)p(\xi,\eta)}{(\xi-x)^2+(\eta-y)^2}d\xi d\eta, \tag{A.3}$$

$$u_z(x,y) = \frac{1-\nu}{2\pi\mu} \int\int \frac{p(\xi,\eta)}{\sqrt{(\xi-x)^2+(\eta-y)^2}}d\xi d\eta, \tag{A.4}$$

This integral form can be further simplified in Fourier space by using the property of convolution:

$$f(x,y) * g(x,y) = \int_{-\infty}^{+\infty}\int_{-\infty}^{+\infty} f(x-\xi,y-\eta)g(x,y)d\xi d\eta, \tag{A.5}$$

and its Fourier transform

$$F[f(x,y) * g(x,y)] = F[f] \cdot F[g]. \tag{A.6}$$

Fourier transform of Eq.(A.2)-(A.4) leads to

$$\hat{u}_x(k_1,k_2) = -\frac{1-2\nu}{2\mu}\frac{ik_1}{k^2}\hat{p}(k_1,k_2), \tag{A.7}$$

$$\hat{u}_y(k_1, k_2) = -\frac{1 - 2\nu}{2\mu} \frac{ik_2}{k^2} \hat{p}(k_1, k_2), \tag{A.8}$$

$$\hat{u}_z(k_1, k_2) = \frac{1 - \nu}{\mu} \frac{1}{k} \hat{p}(k_1, k_2). \tag{A.9}$$

Similarly, Cerruti's problem considers a concentrated shear force acting on the surface of a half plane with no body force. The displacement on the surface are given by

$$u_x = \frac{p_x}{2\pi\mu} \frac{x^2 + (1 - \nu)y^2}{(x^2 + y^2)^{3/2}}, \tag{A.10}$$

$$u_y = \frac{p_x}{2\pi\mu} \frac{\nu x y}{(x^2 + y^2)^{3/2}}, \tag{A.11}$$

$$u_z = -\frac{p_x}{4\pi\mu} \frac{(1 - 2\nu)x}{x^2 + y^2}. \tag{A.12}$$

Corresponding displacements for distributed shear tractions in both x and y directions, $\tau_x(x, y)$ and $\tau_y(x, y)$, take the form:

$$u_x = \frac{1}{2\pi\mu} \int \int \frac{[(x - \xi)^2 + (1 - \nu)(y - \eta)^2]\tau_x(\xi, \eta) + \nu(x - \xi)(y - \eta)\tau_y(\xi, \eta)}{[(x - \xi)^2 + (y - \eta)^2]^{3/2}} d\xi d\eta, \tag{A.13}$$

$$u_y = \frac{1}{2\pi\mu} \int \int \frac{[(1 - \nu)(x - \xi)^2 + (y - \eta)^2]\tau_y(\xi, \eta) + \nu(x - \xi)(y - \eta)\tau_x(\xi, \eta)}{[(x - \xi)^2 + (y - \eta)^2]^{3/2}} d\xi d\eta, \tag{A.14}$$

$$u_z = -\frac{1-2\nu}{4\pi\mu} \int \int \frac{(x-\xi)\tau_x(\xi,\eta) + (y-\eta)\tau_y(\xi,\eta)}{(x-\xi)^2 + (y-\eta)^2} d\xi d\eta, \qquad (A.15)$$

Again, Fourier transform of (A.13)-(A.15) leads to

$$\hat{u}_x(k_1, k_2) = \frac{1}{\mu k^3}[(k_2^2 + (1-\nu)k_1^2)\hat{\tau}_x - \nu k_1 k_2 \hat{\tau}_y], \qquad (A.16)$$

$$\hat{u}_y(k_1, k_2) = \frac{1}{\mu k^3}[(k_1^2 + (1-\nu)k_2^2)\hat{\tau}_y - \nu k_1 k_2 \hat{\tau}_x], \qquad (A.17)$$

$$\hat{u}_z(k_1, k_2) = \frac{1-2\nu}{2\mu} \frac{ik_1\hat{\tau}_x + ik_2\hat{\tau}_y}{k^2}. \qquad (A.18)$$

Combining the solutions to the Boussinesq's problem and Cerruti's problem gives the general solution for the isotropic linear elastic half-space problem,

$$\begin{pmatrix} \hat{u}_x \\ \hat{u}_y \\ \hat{u}_z \end{pmatrix} = \frac{1}{\mu k^3} \begin{bmatrix} (1-\nu)k^2 + \nu k_2^2 & -\nu k_1 k_2 & -\frac{1-2\nu}{2}ik_1 k \\ -\nu k_1 k_2 & (1-\nu)k^2 + \nu k_1^2 & -\frac{1-2\nu}{2}ik_2 k \\ \frac{1-2\nu}{2}ik_1 k & \frac{1-2\nu}{2}ik_2 k & (1-\nu)k^2 \end{bmatrix} \begin{pmatrix} \hat{\tau}_x \\ \hat{\tau}_y \\ \hat{p} \end{pmatrix}, \qquad (A.19)$$

which can be rewritten in the compact form,

$$\hat{u}_i = Q_{ij}\hat{T}_j. \qquad (A.20)$$

Index i and j take value from 1 to 3.

A.2 Generally anisotropic solution

Methods for solving problems with respect to anisotropic materials are well established so far [98, 179–182]. Essentially, all of these methods are related and extended upon the formulism given by either Lekhnitskii or Stroh [179, 180]. These methods, however, are limited to give solutions for cases where the stress and displacement fields depend on only two of the three spatial coordinates x_1, x_2, and x_3, and very few solutions exist for problems of general anisotropy when the stresses depend on all three coordinates. Solutions for a concentrated point force in an infinite body or on the surface of a half-plane are generally obtained using transform methods, such that a 2D problem is obtained in transform domain and can be solved by using Stroh and Lekhnitskii formulism [143, 183, 184]. Here we develop a procedure based on the transform method, and extend it to give solutions for general anisotropy. Similar procedures have been used previously for different applications but limited to cubic crystal structures only [143]. Special cases such as cubic structure and isotropic elasticity are reduced at the end of this part as the verification of our method. Consider a linear elastic half plane with generally anisotropic material subject to arbitrary surface tractions. Substituting the general Hooke's law into the equilibrium equation leads to

$$C_{ijkl}u_{k,jl} = 0, \qquad\qquad (A.21)$$

where C_{ijkl} is the elastic moduli and u_k the displacement, with the subscripts taking values from 1 to 3 for the coordinates. We take Fourier transform of

Eq.(A.21) with respect to the x_1 and x_2 coordinates and obtain that

$$L_{ij}\frac{\partial^2 \hat{u}_j}{\partial x_3^2} + ikM_{ij}\frac{\partial \hat{u}_j}{\partial x_3} - k^2 N_{ij}\hat{u}_j = 0, \tag{A.22}$$

where

$$\hat{u}_j = \hat{u}_j(x_3, k_1, k_2) = \frac{1}{2\pi}\int_{-\infty}^{+\infty}\int_{-\infty}^{+\infty} u_j(x_1, x_2, x_3)\exp(ik_1 x_1 + ik_2 x_2)dx_1 dx_2, \tag{A.23}$$

$$[L_{ij}] = \begin{bmatrix} C_{55} & C_{45} & C_{35} \\ \\ C_{45} & C_{44} & C_{34} \\ \\ C_{35} & C_{34} & C_{33} \end{bmatrix}, \tag{A.24}$$

$$[M_{ij}] = \frac{1}{k}\begin{bmatrix} 2(k_1 C_{15} + k_2 C_{56}) & k_1(C_{56} + C_{14}) + k_2(C_{25} + C_{46}) & k_1(C_{13} + C_{55}) + k_2(C_{45} + C_{36}) \\ & 2(k_1 C_{46} + k_2 C_{24}) & k_1(C_{36} + C_{45}) + k_2(C_{23} + C_{44}) \\ sym & & 2(k_1 C_{35} + k_2 C_{34}) \end{bmatrix}, \tag{A.25}$$

$$[N_{ij}] = \frac{1}{k^2} \begin{bmatrix} k_1^2 C_{11} + 2k_1 k_2 C_{16} + k_2^2 C_{66} & k_1^2 C_{16} + k_1 k_2 (C_{12} + C_{66}) + k_2^2 C_{26} \\ & k_1^2 C_{66} + 2k_1 k_2 C_{26} + k_2^2 C_{22} \\ \\ sym & \end{bmatrix}$$

$$\begin{bmatrix} k_1^2 C_{15} + k_1 k_2 (C_{14} + C_{56}) + k_2^2 C_{46} \\ \\ k_1^2 C_{56} + k_1 k_2 (C_{25} + C_{46}) + k_2^2 C_{24} \\ \\ k_1^2 C_{55} + 2k_1 k_2 C_{45} + k_2^2 C_{44} \end{bmatrix}, \qquad (A.26)$$

and $k = \sqrt{k_1^2 + k_2^2}$. The Voigt's abbreviated notation for the elastic moduli has been used in Eqs.(A.24)-(A.26).

The solution to Eq.(A.22) takes the general form

$$\hat{u}_j = v_j(k_1, k_2) \exp(\lambda k x_3). \qquad (A.27)$$

Substituting (A.27) into (A.22) leads to

$$(\lambda^2 L_{ij} + i\lambda M_{ij} - N_{ij})v_j = 0. \qquad (A.28)$$

Therefore, $v_j(k_1, k_2)$ can be determined as the eigen vector from Eq.(A.28) corresponding to the eigen value λ, which can be solved by setting the determinant of the coefficient matrix to be zero. In general, there exist six eigen values. For the half-space problem, however, the displacement vanishes as $x_3 \rightarrow -\infty$.

Thus, only the three eigen values with positive real part are retained. The complete solution takes the form

$$\hat{u}_j = \sum_{n=1}^{3} A_n v_j^n \exp(\lambda_n k x_3). \tag{A.29}$$

Next, the boundary condition at the surface ($x_3 = 0$) is specified to determine the coefficients An in Eq.(A.29).

The Fourier transform of the surface traction, $T_i(x_1, x_2) = \sigma_{3i}(x_1, x_2, 0)$, relates to the displacement as

$$\hat{T}_i = \Sigma_{n=1}^{3} D_i^{(n)} A_n, \tag{A.30}$$

where

$$D_i^{(n)} = (P_{ij} + k\lambda_n L_{ij})v_j^{(n)}, \tag{A.31}$$

$$[P_{ij}] = \begin{bmatrix} ik_1 C_{15} + ik_2 C_{56} & ik_1 C_{56} + ik_2 C_{25} & ik_1 C_{55} + ik_2 C_{45} \\ ik_1 C_{14} + ik_2 C_{46} & ik_1 C_{46} + ik_2 C_{24} & ik_1 C_{45} + ik_2 C_{44} \\ ik_1 C_{13} + ik_2 C_{36} & ik_1 C_{36} + ik_2 C_{23} & ik_1 C_{35} + ik_2 C_{34} \end{bmatrix} \tag{A.32}$$

This completes the solution procedure. To summarize, the flow of the solution steps is as follows.

(i) For each wave vector, (k_1, k_2), the eigen values and eigen vectors are obtained from Eq.(A.28);

(ii) For given surface traction, the coefficients An are solved from Eq.(A.30).

(iii) The displacement is determined by Eq.(A.29). In particular, for the present study, the surface displacement is related to the surface traction in form of

$$\hat{u}_j(x_3 = 0; k_1, k_2) = Q_{ij}(k_1, k_2)\hat{T}_i. \tag{A.33}$$

(iv) The strain and stress on the surface can be obtained from (A.29):

$$\frac{\partial \hat{u}_j}{\partial x_3} = \sum_{n=1}^{3} A_n \lambda_n k v_j^{(n)} \exp(\lambda_n k x_3), \tag{A.34}$$

$$\hat{\sigma}_{ij} = ik_\beta C_{ij\alpha\beta}\hat{u}_\alpha + C_{ij\alpha3}\left(\frac{\partial \hat{u}_\alpha}{\partial x_3} + ik_\alpha \hat{u}_3\right) + C_{ij33}\frac{\partial \hat{u}_\alpha}{\partial x_3}. \tag{A.35}$$

As a special case for the general solution, consider a half space of cubic crystal with its surface parallel to the (001) plane. In this case, the eigenvalue problem in (A.28) reduces to that in Lu and Suo [143]. The eigenvalues can then be obtained by solving a cubic algebraic equation of :

$$\lambda^6 + d_1\lambda^4 + d_2\lambda^2 + d_3 = 0, \tag{A.36}$$

where

$$d_1 = -\frac{R^2 + RS + S^2 - 1}{RS}, \tag{A.37}$$

$$d_2 = \frac{R^2 + RS + S^2 - 1}{RS} + \frac{S^3 - 2RS^2 + R^2S - 3S + 2R + 2}{R^2S}\frac{k_1^2 k_2^2}{k^4}, \tag{A.38}$$

$$d_3 = -\frac{(R-S)^2 - 1}{RS} \frac{k_1^2 k_2^2}{k^4} - 1, \tag{A.39}$$

with $R = C_{44}/(C_{12} + C_{44})$ and $S = C_{11}/(C_{12} + C_{44})$. Similarly, Eq.(A.30) reduces to Eq. (20) in Lu and Suo [143] for (001) cubic crystals.

An important thing need to note here is that the isotropic case can not be further recovered directly from the results of cubic crystals. It will be shown in the following that, isotropic material properties lead to triply degenerate eigenvalue in Eq.(A.36), and in turn no independent eigenvectors can be obtained by general solution (A.27). A different form is thus needed due to the degeneration.

We go back to Eq.(A.22) to solve the problem for isotropic cases. Now, Eqs.(A.24)-(A.26) becomes

$$[L_{ij}] = \begin{bmatrix} \mu & 0 & 0 \\ & \mu & 0 \\ sym & & \lambda + 2\mu \end{bmatrix}, \tag{A.40}$$

$$[M_{ij}] = \frac{1}{k} \begin{bmatrix} 0 & 0 & k_1(\lambda + \mu) \\ & 0 & k_2(\lambda + \mu) \\ sym & & 0 \end{bmatrix}, \tag{A.41}$$

$$[N_{ij}] = \frac{1}{k^2} \begin{bmatrix} k_1^2(\lambda+2\mu) + k_2^2\mu & k_1k_2(\lambda+\mu) & 0 \\ & k_1^2\mu + k_2^2(\lambda+2\mu) & 0 \\ sym & & 0 \end{bmatrix}. \qquad (A.42)$$

Then, Eq.(A.22) can be simplified to,

$$\frac{\partial^4 \hat{u}_1}{\partial x_3^4} - 2k^2 \frac{\partial^2 \hat{u}_1}{\partial x_3^2} + k^4 \hat{u}_1 = 0. \qquad (A.43)$$

The general solution to (A.43) is:

$$\hat{u}_1 = (A_1 + B_1 k x_3) \exp(k x_3). \qquad (A.44)$$

Similarly, we can get the general solution for other components in the form

$$\hat{u}_j = (A_j + B_j k x_3) \exp(k x_3). \qquad (A.45)$$

which are differing from (A.27). Substituting (A.45) into Eq.(A.22) together with the isotropic elastic moduli, we obtain that

$$\frac{B_1}{k_1} = \frac{B_2}{k_2}, \qquad (A.46)$$

$$A_3 = \frac{1}{k}[-ik_1 A_1 - ik_2 A_2 - \frac{k^2(\lambda+3\mu)}{ik_1(\lambda+\mu)} B_1], \qquad (A.47)$$

$$B_3 = -\frac{ik}{k_1}B_1. \tag{A.48}$$

Applying the boundary condition at the surface leads to three more equations that complete the solution,

$$\hat{\tau}_x = \mu\left(\frac{\partial \hat{u}_1}{\partial x_3} + ik_1\hat{u}_3\right) = \frac{\mu}{k}[(2k_1^2 + k_2^2)A_1 + k_1k_2B_1 - \frac{2\mu}{\lambda + \mu}k^2A_2], \tag{A.49}$$

$$\hat{\tau}_y = \mu\left(\frac{\partial \hat{u}_2}{\partial x_3} + ik_2\hat{u}_3\right) = \frac{\mu}{k}[(k_1k_2A_1 + 2k_1^2 + k_2^2)B_1 - \frac{2\mu}{\lambda + \mu}k^2B_2], \tag{A.50}$$

$$\hat{p} = \lambda(ik_1\hat{u}_1 + ik_2\hat{u}_2) + (\lambda + 2\mu)\frac{\partial \hat{u}_3}{\partial x_3} = 2\mu(-ik_1A_1 - ik_2B_1) + \frac{2\mu(\lambda + 2\mu)}{\lambda + \mu}\frac{ik^2}{k_1}A_2. \tag{A.51}$$

Combining (A.46)-(A.51) by eliminating coefficients recovers the relationship between the surface tractions and the surface displacements, which is identical to solutions by integrating the classical solutions to the Cerruti's and Boussinesq's problems obtained previously in (A.19).

Appendix B

Transformation of Anisotropic Elastic Moduli

In many cases, it is more convenient to work in an arbitrarily orientated coordinate system to calculate the stress and strain components. Thus a generalized Hooke's law must be used and the elastic coefficients need to be determined from a tensor transformation for the particular orientation.

Let C_{ijkl} be the elastic moduli at the natural crystalline coordinate (in Figure 5.1). In an arbitrarily rotated coordinates (e.g., in Figure 5.1 for the epitaxial system), the elastic moduli can be obtained by transformation

$$\widetilde{C}_{ijkl} = T_{im}T_{jn}T_{kp}T_{lq}C_{mnpq}, \qquad (B.1)$$

where is the rotation matrix from the reference coordinates to the epitaxial coordinates . For cubic crystals such as Si and Ge, the transformation reduces

to

$$\widetilde{C}_{ijkl} = C_{ijkl} - C_0[\sum_{n=1}^{3} T_{in}T_{jn}T_{kn}T_{ln} - \delta_{ij}\delta_{kl}\delta_{ik}], \qquad \text{(B.2)}$$

where $C_0 = C_{11} - C_{12} - 2C_{44}$ and no summation is implied for indices i and k. For convenience, the elastic moduli of Si and Ge in the four epitaxial coordinates considered in the present study are listed in the matrix form as follows.

Si(001), with the coordinate axes coinciding with the crystal directions, [100], [010], and [001], which is identical to the natural coordinates:

$$\mathbf{C}_{(001)} = \begin{bmatrix} 166.2 & 64.4 & 64.4 & 0 & 0 & 0 \\ 64.4 & 166.2 & 64.4 & 0 & 0 & 0 \\ 64.4 & 64.4 & 166.2 & 0 & 0 & 0 \\ 0 & 0 & 0 & 79.8 & 0 & 0 \\ 0 & 0 & 0 & 0 & 79.8 & 0 \\ 0 & 0 & 0 & 0 & 0 & 79.8 \end{bmatrix} (GPa). \qquad \text{(B.3)}$$

Si(111), with the coordinate axes in the crystal directions, $[2\bar{1}\bar{1}]$, $[01\bar{1}]$,

and [111]:

$$\widetilde{\mathbf{C}}_{(111)} = \begin{bmatrix} 195.1 & 54.8 & 45.1 & 0 & -13.6 & 0 \\ 54.8 & 195.1 & 45.1 & 0 & 13.6 & 0 \\ 45.1 & 45.1 & 204.7 & 0 & 0 & 0 \\ 0 & 0 & 0 & 60.5 & 0 & 13.6 \\ -13.6 & 13.6 & 0 & 0 & 60.5 & 0 \\ 0 & 0 & 0 & 13.6 & 0 & 70.2 \end{bmatrix} \quad (GPa). \qquad (B.4)$$

Si(**110**), with the coordinate axes in the crystal directions, $[\bar{1}10]$, $[001]$, and $[110]$:

$$\widetilde{\mathbf{C}}_{(110)} = \begin{bmatrix} 195.1 & 64.4 & 35.5 & 0 & 0 & 0 \\ 64.4 & 166.2 & 64.4 & 0 & 0 & 0 \\ 35.5 & 64.4 & 195.1 & 0 & 0 & 0 \\ 0 & 0 & 0 & 79.8 & 0 & 0 \\ 0 & 0 & 0 & 0 & 50.9 & 0 \\ 0 & 0 & 0 & 0 & 0 & 79.8 \end{bmatrix} \quad (GPa). \qquad (B.5)$$

Si(113), with the coordinate axes in the crystal directions, $[\bar{1}10]$, $[\bar{3}\bar{3}2]$, and $[113]$:

$$\widetilde{\mathbf{C}}_{(113)} = \begin{bmatrix} 195.1 & 40.8 & 59.1 & 11.1 & 0 & 0 \\ 40.8 & 202.7 & 51.5 & 5.1 & 0 & 0 \\ 59.1 & 51.5 & 184.4 & -16.2 & 0 & 0 \\ 11.1 & 5.1 & -16.2 & 66.9 & 0 & 0 \\ 0 & 0 & 0 & 0 & 74.5 & 11.1 \\ 0 & 0 & 0 & 0 & 11.1 & 56.2 \end{bmatrix} \quad (GPa). \quad (B.6)$$

Ge(001), with the coordinate axes coinciding with the crystal directions, $[100]$, $[010]$, and $[001]$, which is identical to the natural coordinates:

$$\mathbf{C}_{(001)} = \begin{bmatrix} 128.4 & 48.2 & 48.2 & 0 & 0 & 0 \\ 48.2 & 128.4 & 48.2 & 0 & 0 & 0 \\ 48.2 & 48.2 & 128.4 & 0 & 0 & 0 \\ 0 & 0 & 0 & 66.7 & 0 & 0 \\ 0 & 0 & 0 & 0 & 66.7 & 0 \\ 0 & 0 & 0 & 0 & 0 & 66.7 \end{bmatrix} \quad (GPa). \quad (B.7)$$

$\mathbf{Ge(111)}$, with the coordinate axes in the crystal directions, $[2\bar{1}\bar{1}]$, $[01\bar{1}]$, and $[111]$:

$$\widetilde{\mathbf{C}}_{(111)} = \begin{bmatrix} 155.0 & 39.3 & 30.5 & 0 & -12.5 & 0 \\ 39.3 & 155.0 & 30.5 & 0 & 12.5 & 0 \\ 30.5 & 30.5 & 163.9 & 0 & 0 & 0 \\ 0 & 0 & 0 & 49.0 & 0 & 12.5 \\ -12.5 & 12.5 & 0 & 0 & 49.0 & 0 \\ 0 & 0 & 0 & 12.5 & 0 & 57.8 \end{bmatrix} \quad (GPa). \qquad \text{(B.8)}$$

$\mathbf{Ge(110)}$, with the coordinate axes in the crystal directions, $[\bar{1}10]$, $[001]$, and $[110]$:

$$\widetilde{\mathbf{C}}_{(110)} = \begin{bmatrix} 155.0 & 48.2 & 21.6 & 0 & 0 & 0 \\ 48.2 & 128.4 & 48.2 & 0 & 0 & 0 \\ 21.6 & 48.2 & 155.0 & 0 & 0 & 0 \\ 0 & 0 & 0 & 66.7 & 0 & 0 \\ 0 & 0 & 0 & 0 & 40.1 & 0 \\ 0 & 0 & 0 & 0 & 0 & 66.7 \end{bmatrix} \quad (GPa). \qquad \text{(B.9)}$$

$\mathbf{Ge(113)}$, with the coordinate axes in the crystal directions, $[\bar{1}10]$, $[\bar{3}\bar{3}2]$, and $[113]$:

$$\widetilde{\mathbf{C}}_{(113)} = \begin{bmatrix} 155.0 & 26.4 & 43.4 & 10.3 & 0 & 0 \\ 26.4 & 162.0 & 36.3 & 4.7 & 0 & 0 \\ 43.4 & 36.3 & 145.1 & -14.9 & 0 & 0 \\ 10.3 & 4.7 & -14.9 & 54.8 & 0 & 0 \\ 0 & 0 & 0 & 0 & 61.9 & 10.3 \\ 0 & 0 & 0 & 0 & 10.3 & 45.0 \end{bmatrix} \quad (GPa). \qquad (B.10)$$

Bibliography

[1] G.E. Moore. Cramming more components onto integrated circuits. *Electronics Magazine*, 38(8), 1965.

[2] S. Luryi, J. Xu, and A. Zaslavsky, editors. *Future Trends in Microelectronics: The Road Ahead.* John Wiley and Sons, 1999.

[3] R. Turton. *The Quantum Dot : A Journey Into the Future of Microelectronics.* Oxford University Press, New York, 1995.

[4] M. Ohring. *The Materials science of Thin Films.* Academic Press, San Diego, CA, 2002.

[5] R. Mark and D. Ratner. *Nanotechnology: A Gentle Introduction to the Next Big Idea.* Upper Saddle River, 2003.

[6] X. Zhang, C. Sun, and N. Fang. Manufacturing at nanoscale: Top-Down, Bottom-Up and system engineering. *Journal of Nanoparticle Research*, 6:125–130, 2004.

[7] S.Y. Chou. Nanoimprint lithography and lithographically induced self-assembly. *MRS Bulletin*, 26:512–517, 2001.

[8] S. Zhang. Building from the bottom up. *Materials Today*, 6:20–27, 2003.

[9] R.D. Kamien. Physics: Topology from the bottom up. *Science*, 299:1671–1673, 2003.

[10] G.M. Whitesides, J.P. Mathias, and C.T. Seto. Molecular self-assembly and nanochemistry: A chemical strategy for the synthesis of nanostructures. *Science*, 254:1312, 1991.

[11] T.E. Price. *Introduction to VLSI Technology*. Prentice Hall, London, 1994.

[12] L.B. Freund and S. Suresh. *Thin Film Materials : Stress, Defect Formation and Surface Evolution*. Cambridge University Press, Cambridge, UK, 2004.

[13] J.M. Blakely. *Introduction to the Properties of Crystal Surfaces*. Pergamon Press, Oxford, New York, 1973.

[14] F.C. Frank and J.H. Van Der Merwe. One-dimensional dislocations II. misfitting monolayers and oriented overgrowth. *Proceedings of the Royal Society A*, 198:216–225, 1949.

[15] I.N. Stranski and L. Krastanow. Sitzungsberichte der akademie der wissenschaften in wien. *Akad. Wiss. Lit. Mainz Math. -Natur.*, K1.IIb(146), 1939.

[16] M. Volmer and A. Weber. Novel growth mechanism in heteroepitaxial semiconductor growth. *Zeitschrift fr Physikalische Chemie*, 119, 1926.

[17] D. Leonard, M. Krishnamurthy, C.M. Reaves, S.P. DenBaars, and P.M. Petroff. Direct formation of quantum-sized dots from uniform coherent

islands of InGaAs on GaAs-surface. *Applied Physics Letters*, 63:3203–3205, 1993.

[18] V.A. Shchukin and D. Bimberg. Spontaneous ordering of nanostructures on crystal surfaces. *Reviews of Modern Physics*, 71:1125–1171, 1999.

[19] Y.W. Mo, D.E. Savage, B.S. Swartzentruber, and M.G. Lagally. Kinetic pathway in Stranski-Krastanov growth of Ge on Si(001). *Physical Review Letters*, 65(8):1020–1023, 1990.

[20] D.J. Eaglesham and M. Cerullo. Dislocation-free Stranski-Krastanow growth of Ge on Si(100). *Physical Review Letters*, 64(16):1943–1946, 1990.

[21] A.G. Cullis, D.J. Robbins, A.J. Pidduck, and P.W. Smith. The characteristics of strain-modulated surface undulations formed upon epitaxial Si1-xGex alloy layers on Si. *Journal of Crystal Growth*, 123:333–343, 1992.

[22] P.O. Hansson, M. Albrecht, H.P. Strunk, E. Bauser, and J.H. Werner. Dimensionality and critical size of GeSi on Si(100). *Thin Solid Films*, 216:199–202, 1992.

[23] H.J. Osten, H.P. Zeindl, and E. Bugiel. Considerations about the critical thickness for pseudomorphic Si1-xGex growth on Si(001). *Journal of Crystal Growth*, 143:194–199, 1994.

[24] C.S. Ozkan, W.D. Nix, and H.J. Gao. Strain relaxation and defect formation in heteroepitaxial Si1-xGex films via surface roughening induced by

controlled annealing experiments. *Applied Physics Letters*, 70(17):2247–2249, 1997.

[25] J.A. Floro, E. Chason, R.D. Twesten, R.Q. Hwang, and L.B. Freund. SiGe coherent islanding and stress relaxation in the high mobility regime. *Physical Review Letters*, 79(20):3946–3949, 1997.

[26] W. Dorsch, H.P. Strunk, H. Wawra, G. Wagner, J. Groenen, and R. Carles. Strain-induced island scaling during Si1-xGex heteroepitaxy. *Applied Physics Letters*, 72(2):179–181, 1998.

[27] W. Dorsch, B. Steiner, M. Albrecht, H.P. Strunk, H. Wawra, and G. Wagner. The transition from ripples to islands in strained heteroepitaxial growth under low driving forces. *Journal of Crystal Growth*, 183(3):305–310, 1998.

[28] J.A. Floro, E. Chason, L.B. Freund, R.D. Twesten, R.Q. Hwang, and G.A. Lucadamo. Evolution of coherent islands in Si1-xGex/Si(001). *Physical Review B*, 59(3):1990–1998, 1999.

[29] I. Berbezier, A. Ronda, F. Volpi, and A. Portavoce. Morphological evolution of SiGe layers. *Surface Science*, 531:231–243, 2003.

[30] D. Bimberg, M. Grundmann, N.N. Ledentsov, S.S. Ruvimov, P. Werner, U. Richter, J. Heydenreich, V.M. Ustinov, P.S. Kopev, and Zh.I. Alferov. Self-organization processes in MBE-grown quantum dot structures. *Thin Solid Films*, 267:32–36, 1995.

[31] M. Meixner, E. Scholl, M. Schmidbauer, H. Raidt, and R. Kohler. For-

mation of island chains in SiGe/Si heteroepitaxy by elastic anisotropy. *Physical Review B*, 64(24):245307, 2001.

[32] K. Ohmori, Y.L. Foo, S. Hong, J.G. Wen, J.E. Greene, and I. Petrov. Directed self-assembly of Ge nanostructures on very high index, highly anisotropic Si(hkl) surfaces. *Nano Letters*, 5(2):369–372, 2005.

[33] T.I. Kamins and R.S. Williams. Lithographic positioning of self-assembled Ge islands on Si(001). *Applied Physics Letters*, 71(9):1201–1203, 1997.

[34] G. Jin, J.L. Liu, S.G. Thomas, Y.H. Luo, K.L. Wang, and B.Y. Nguyen. Controlled arrangement of self-organized Ge islands on patterned Si(001) substrates. *Applied Physics Letters*, 75(18):2752–2754, 1999.

[35] B. Yang, F. Liu, and M.G. Lagally. Local strain-mediated chemical potential control of quantum dot self-organization in heteroepitaxy. *Physical Review Letters*, 92(2):025502, 2004.

[36] C. Teichert, M.G. Lagally, L.J. Peticolas, J.C. Bean, and J. Tersoff. Stress-induced self-organization of nanoscale structures in SiGe/Si multilayer films. *Physical Review B*, 53(24):16334–16337, 1996.

[37] G. Bauer, A.A. Darhuber, and V. Holy. Self-assembled germanium-dot multilayers embedded in silicon. *Crystal Research and Technology*, 34(2):197–209, 1999.

[38] K. Sakamoto, H. Matsuhata, M.O. Tanner, D. Wang, and K.L. Wang. Alignment of Ge three-dimensional islands on faceted Si(001) surfaces. *Thin Solid Films*, 321:55–59, 1998.

[39] Y.H. Xie, S.B. Samavedam, M. Bulsara, T.A. Langdo, and E.A. Fitzgerald. Relaxed template for fabricating regularly distributed quantum dot arrays. *Applied Physics Letters*, 71(24):3567–3568, 1997.

[40] F. Leroy, G. Renaud, A. Letoublon, R. Lazzari, C. Mottet, and J. Goniakowski. Self-organized growth of nanoparticles on a surface patterned by a buried dislocation network. *Physical Review Letters*, 95(18), 2005.

[41] J. Coelho, G. Patriarche, F. Glas, I. Sagnes, and G. Saint-Girons. Stress-engineered orderings of self-assembled III-V semiconductor nanostructures. *Physica Status Solidi*, 2(4):1245–1250, 2005.

[42] G. Springholz, V. Holy, M. Pinczolits, and G. Bauer. Self-organized growth of three-dimensional quantum-dot crystals with fcc-like stacking and a tunable lattice constant. *Science*, 282(5389):734–737, 1998.

[43] T. Ogino, Y. Homma, Y. Kobayashi, H. Hibino, K. Prabhakaran, K. Sumitomo, H. Omi, S. Suzuki, T. Yamashita, D.J. Bottomley, F. Ling, and A. Kaneko. Design of Si surfaces for self-assembled nano architecture. *Surface Science*, 514(1-3):1–9, 2002.

[44] R. Nuryadi, Y. Ishikawa, Y. Ono, and M. Tabe. Thermal agglomeration of single-crystalline Si layer on buried SiO2 in ultrahigh vacuum. *The Journal of Vacuum Science and Technology B*, 20:167–172, 2002.

[45] Y. Ishikawa, Y.Imai, H. Ikeda, and M. Tabe. Pattern-induced alignment of silicon islands on buried oxide layer of silicon-on-insulator substrate. *Applied Physics Letters*, 83:3162–3164, 2003.

[46] D. Loretto, F.M. Ross, and C.A. Lucas. Quasi-one-dimensional CaF2 islands formed on Si(001) by molecular beam epitaxy. *Applied Physics Letters*, 68:2363–2365, 1996.

[47] H. Omi and T. Ogino. Self-assembled Ge nanowires grown on Si(113). *Applied Physics Letters*, 71(15):2163–2165, 1997.

[48] H. Omi and T. Ogino. Self-organization of Ge islands on high-index Si substrates. *Physical Review B*, 59(11):7521–7528, 1999.

[49] Y. Chen, D.A.A. Ohlberg, G. Medeiros-Robeiro, Y.A. Chang, and R.S. Williams. Growth and evolution of epitaxial erbium disilicide nanowires on Si(001). *Applied Physics A*, 75:353–361, 2002.

[50] Z.H. Zhang, K. Sumitomo, H. Omi, and T. Ogino. Influences of the Si(113) anisotropy on Ge nanowire formation and related island shape transition. *Surface Science*, 497(1-3):93–99, 2002.

[51] J.H. Lee. Wirelike growth of self-assembled hafnium silicides: Oxide mediate epitaxy. *Applied Surface Science*, 239:268–272, 2005.

[52] M. Hupalo and M.C. Tringides. Self-organization and geometry control of Pb islands grown on anisotropic substrates. *Physical Review B*, 73(4):041405, 2006.

[53] G. Chen, J. Wan, J.S. Yang, X.M. Ding, L. Ye, and X. Wang. Surface structures of erbium silicide ultra-thin films formed by solid phase epitaxy on Si(100). *Surface Science*, 513(1):203–210, 2002.

144

[54] C. Preinesberger, S. Vandre, T. Kalka, and M. Dahne-Prietsch. Formation of dysprosium silicide wires on Si(001). *Journal of Physics D-Applied Physics*, 31(12):L43–L45, 1998.

[55] Y. Chen, D.A.A. Ohlberg, G. Medeiros-Ribeiro, Y.A. Chang, and R.S. Williams. Self-assembled growth of epitaxial erbium disilicide nanowires on silicon (001). *Applied Physics Letters*, 76(26):4004–4006, 2000.

[56] Z.A. He, D.J. Smith, and P.A. Bennett. Faulted surface layers in dysprosium silicide nanowires. *Physical Review B*, 70(24):241402, 2004.

[57] J.L. McChesney, A. Kirakosian, R. Bennewitz, J.N. Crain, J.L. Lin, and F.J. Himpsel. Gd disilicide nanowires attached to Si(111) steps. *Nanotechnology*, 13(4):545–547, 2002.

[58] G.F. Ye, M.A. Crimp, and J. Nogami. Crystallographic study of self-assembled dysprosium silicide nanostructures on Si(001). *Physical Review B*, 74(3):033104, 2006.

[59] J. Nogami, B.Z. Liu, M.V. Katkov, C. Ohbuchi, and N.O. Birge. Self-assembled rare-earth silicide nanowires on Si(001). *Physical Review B*, 63(23):233305, 2001.

[60] A. Lorke, R.J. Luyken, J.M. Garcia, and P.M. Petroff. Growth and electronic properties of self-organized quantum rings. *Japanese Journal of Applied Physics*, 40:1857–1859, 2001.

[61] R. Blossey and A. Lorke. Wetting droplet instability and quantum ring formation. *Physical Review E*, 65:021603, 2002.

[62] R. Songmuang, S. Kiravittaya, and O.G. Schmidt. Shape evolution of InAs quantum dots during overgrowth. *Journal of Crystal Growth*, 249:416–421, 2002.

[63] T. Raz, D. Ritter, and G. Bahir. Formation of InAs self-assembled quantum rings on InP. *Applied Physics Letters*, 82(11):1706–1708, 2003.

[64] D. Granados and J.M. Garcia. In(Ga)As self-assembled quantum ring formation by molecular beam epitaxy. *Applied Physics Letters*, 82(15):2401–2403, 2003.

[65] J. Cui, Q. He, X.M. Jiang, Y.L. Fan, X.J. Yang, F. Xue, and Z.M. Jiang. Self-assembled SiGe quantum rings grown on Si(001) by molecular beam epitaxy. *Applied Physics Letters*, 83:2907–2909, 2003.

[66] R.J. Asaro and W.A. Tiller. Interface morphology development during stress corrosion cracking: Part I. via surface diffusion. *Metallurgical Transactions*, 3:1789–1796, 1972.

[67] M.A. Grinfeld. Instability of interface between nonhydrostatically stressed elastic body and melts. *Doklady Akademii Nauk Sssr*, 290(6):1358–1363, 1986.

[68] D.J. Srolovitz. On the stability of surfaces of stressed solids. *Acta Metallurgica*, 37(2):621–625, 1989.

[69] W.H. Yang and D.J. Srolovitz. Crack-like surface instabilities in stressed solids. *Physical Review Letters*, 71(10):1593–1596, 1993.

[70] W.H. Yang and D.J. Srolovitz. Surface-morphology evolution in stressed solids - surface-diffusion controlled crack initiation. *Journal of the Mechanics and Physics of Solids*, 42(10):1551–1574, 1994.

[71] B.J. Spencer and D.I. Meiron. Nonlinear evolution of the stress-driven morphological instability in a 2-dimensional semiinfinite solid. *Acta Metallurgica Et Materialia*, 42(11):3629–3641, 1994.

[72] Y. Xiang and W.N. E. Nonlinear evolution equation for the stress-driven morphological instability. *Journal of Applied Physics*, 91(11):9414–9422, 2002.

[73] R.H. Torii and S. Balibar. Helium crystals under stress - the Grinfeld instability. *Journal of Low Temperature Physics*, 89(1-2):391–400, 1992.

[74] J. Berrehar, C. Caroli, C. Lapersonnemeyer, and M. Schott. Surface patterns on single-crystal films under uniaxial-stress - experimental-evidence for the Grinfeld instability. *Physical Review B*, 46(20):13487–13495, 1992.

[75] B.J. Spencer, P.W. Voorhees, and S.H. Davis. Morphological instability in epitaxially strained dislocation-free solid films. *Physical Review Letters*, 67(26):3696–3699, 1991.

[76] L.B. Freund and F. Jonsdottir. Instability of a biaxially stressed thin-film on a substrate due to material diffusion over its free-surface. *Journal of the Mechanics and Physics of Solids*, 41(7):1245–1264, 1993.

[77] H. Liu and R. Huang. Effect of a cap layer on morphological stability

of a strained epitaxial film. *Journal of Applied Physics*, 97(11):113537, 2005.

[78] H.J. Gao and W.D. Nix. Surface roughening of heteroepitaxial thin films. *Annual Review of Materials Science*, 29:173–209, 1999.

[79] M. Coll, J. Gazquez, A. Pomar, T. Puig, F. Sandiumenge, and X. Obradors. Stress-induced spontaneous dewetting of heteroepitaxial YBa2Cu3O7 thin films. *Physical Review B*, 73(7):075420, 2006.

[80] W.T. Tekalign and B.J. Spencer. Evolution equation for a thin epitaxial film on a deformable substrate. *Journal of Applied Physics*, 96(10):5505–5512, 2004.

[81] Y.Y. Pang and R. Huang. Nonlinear effect of stress and wetting on surface evolution of epitaxial thin films. *Physical Review B*, 74(7):075413, 2006.

[82] C.H. Lam, C.K. Lee, and L.M. Sander. Competing roughening mechanisms in strained heteroepitaxy: A fast kinetic Monte Carlo study. *Physical Review Letters*, 89(21):216102, 2002.

[83] R. Zhu, E. Pan, and P.W. Chung. Fast multiscale kinetic Monte Carlo simulations of three-dimensional self-assembled quantum dot islands. *Physical Review B*, 75(20):205339, 2007.

[84] J. Tersoff and R.M. Tromp. Shape transition in growth of strained islands - spontaneous formation of quantum wires. *Physical Review Letters*, 70(18):2782–2785, 1993.

[85] J. Tersoff, B.J. Spencer, A. Rastelli, and H. von Kanel. Barrierless formation and faceting of SiGe islands on Si(001). *Physical Review Letters*, 89(19):196104, 2002.

[86] A. Pradhan, N.Y. Ma, and F. Liu. Theory of equilibrium shape of an anisotropically strained island: Thermodynamic limits for growth of nanowires. *Physical Review B*, 70(19):193405, 2004.

[87] F.M. Ross, J. Tersoff, and R.M. Tromp. Coarsening of self-assembled Ge quantum dots on Si(001). *Physical Review Letters*, 80(5):984–987, 1998.

[88] J.A. Floro, M.B. Sinclair, E. Chason, L.B. Freund, R.D. Twesten, R.Q. Hwang, and G.A. Lucadamo. Novel SiGe island coarsening kinetics: Ostwald ripening and elastic interactions. *Physical Review Letters*, 84(4):701–704, 2000.

[89] F. Liu, A.H. Li, and M.G. Lagally. Self-assembly of two-dimensional islands via strain-mediated coarsening. *Physical Review Letters*, 8712(12):126103, 2001.

[90] F. Liu, P. Rugheimer, E. Mateeva, D.E. Savage, and M.G. Lagally. Nanomechanics - response of a strained semiconductor structure. *Nature*, 416(6880):498–498, 2002.

[91] K. Kassner, C. Misbah, J. Muller, J. Kappey, and P. Kohlert. Phase-field modeling of stress-induced instabilities. *Physical Review E*, 6303(3):036117, 2001.

[92] J.J. Eggleston and P.W. Voorhees. Ordered growth of nanocrystals via a morphological instability. *Applied Physics Letters*, 80(2):306–308, 2002.

149

[93] D.J. Seol, S.Y. Hu, Z.K. Liu, L.Q. Chen, S.G. Kim, and K.H. Oh. Phase-field modeling of stress-induced surface instabilities in heteroepitaxial thin films. *Journal of Applied Physics*, 98(4):044910, 2005.

[94] Y. Ni, L.H. He, and A.K. Soh. Three-dimensional phase field simulation for surface roughening of heteroepitaxial films with elastic anisotropy. *Journal of Crystal Growth*, 284(1-2):281–292, 2005.

[95] B.J. Spencer, S.H. Davis, and P.W. Voorhees. Morphological instability in epitaxially strained dislocation-free solid films - nonlinear evolution. *Physical Review B*, 47(15):9760–9777, 1993.

[96] C.H. Chiu. The self-assembly of uniform heteroepitaxial islands. *Applied Physics Letters*, 75(22):3473–3475, 1999.

[97] Y.W. Zhang and A.F. Bower. Numerical simulations of island formation in a coherent strained epitaxial thin film system. *Journal of the Mechanics and Physics of Solids*, 47(11):2273–2297, 1999.

[98] V.B. Shenoy and L.B. Freund. A continuum description of the energetics and evolution of stepped surfaces in strained nanostructures. *Journal of the Mechanics and Physics of Solids*, 50(9):1817–1841, 2002.

[99] E.A. Fitzgerald. Gesi/Si nanostructures. *Annual Review of Materials Science*, 25:417–454, 1995.

[100] Y.K. Lee, N. Fujimura, T. Ito, and N. Itoh. Epitaxial-growth and structural characterization of erbium eilicide formed on (100)Si through a Solid-Phase reaction. *Journal of Crystal Growth*, 134(3-4):247–254, 1993.

[101] L.B. Freund. Dislocation mechanisms of relaxation in strained epitaxial films. *Materials Research Bulletin*, 17:52–60, 1992.

[102] W.W. Mullins. Theory of thermal grooving. *Journal of Applied Physics*, 28:333–339, 1957.

[103] H.J. Gao. Some general-properties of stress-driven surface evolution in a heteroepitaxial thin-film structure. *Journal of the Mechanics and Physics of Solids*, 42(5):741–772, 1994.

[104] Y.W. Zhang. Self-organization, shape transition, and stability of epitaxially strained islands. *Physical Review B*, 61(15):10388–10392, 2000.

[105] Y.W. Zhang and A.F. Bower. Three-dimensional analysis of shape transitions in strained-heteroepitaxial islands. *Applied Physics Letters*, 78(18):2706–2708, 2001.

[106] T.V. Savina, A.A. Golovin, S.H. Davis, A.A. Nepomnyashchy, and P.W. Voorhees. Faceting of a growing crystal surface by surface diffusion. *Physical Review E*, 67(2):021606, 2003.

[107] J.W. Cahn. Surface stress and the chemical-equilibrium of small crystals .1. the case of the isotropic surface. *Acta Metallurgica*, 28(10):1333–1338, 1980.

[108] R.C. Cammarata. Surface and interface stress effects in thin-films. *Progress in Surface Science*, 46(1):1–38, 1994.

[109] H. Ibach. The role of surface stress in reconstruction, epitaxial growth

and stabilization of mesoscopic structures. *Surface Science Reports*, 29(5-6):195–263, 1997.

[110] T.V. Savina, P.W. Voorhees, and S.H. Davis. The effect of surface stress and wetting layers on morphological instability in epitaxially strained films. *Journal of Applied Physics*, 96(6):3127–3133, 2004.

[111] R.V. Kukta and L.B. Freund. Minimum energy configuration of epitaxial material clusters on a lattice-mismatched substrate. *Journal of the Mechanics and Physics of Solids*, 45(11-12):1835–1860, 1997.

[112] C.H. Chiu and H.J. Gao. A numerical study of stress controlled surface diffusion during epitaxial film growth. *Materials Research Society Symposium - Proceedings*, 356:33–44, 1995.

[113] M. Ortiz, E.A. Repetto, and H. Si. A continuum model of kinetic roughening and coarsening in thin films. *Journal of the Mechanics and Physics of Solids*, 47(4):697–730, 1999.

[114] B.J. Spencer. Asymptotic derivation of the glued-wetting-layer model and contact-angle condition for Stranski-Krastanow islands. *Physical Review B*, 59(3):2011–2017, 1999.

[115] Z.G. Suo and Z.Y. Zhang. Epitaxial films stabilized by long-range forces. *Physical Review B*, 58(8):5116–5120, 1998.

[116] A.A. Golovin, S.H. Davis, and P.W. Voorhees. Self-organization of quantum dots in epitaxially strained solid films. *Physical Review E*, 68(5):056203, 2003.

[117] S.P. Gill. Self-organised growth on strained substrates: the influence of anisotropic strain, surface energy and surface diffusivity. *Thin Solid Films*, 423(2):136–145, 2003.

[118] H.H. Yu. The asymmetric effect of stress in the morphological instability of a growing thin film. *Modelling and Simulation in Materials Science and Engineering*, 13(6):797–808, 2005.

[119] R. Panat, K.J. Hsia, and D.G. Cahill. Evolution of surface waviness in thin films via volume and surface diffusion. *Journal of Applied Physics*, 97(1):013521, 2005.

[120] G. Medeiros-Ribeiro, A.M. Bratkovski, T.I. Kamins, D.A.A. Ohlberg, and R.S. Williams. Shape transition of germanium nanocrystals on a silicon (001) surface from pyramids to domes. *Science*, 279(5349):353–355, 1998.

[121] Z. Gai, B. Wu, J.P. Pierce, G.A. Farnan, D.J. Shu, M. Wang, Z.Y. Zhang, and J. Shen. Self-assembly of nanometer-scale magnetic dots with narrow size distributions on an insulating substrate. *Physical Review Letters*, 89(23):235502, 2002.

[122] L.N. Trefethen. *Spectral Methods in MATLAB*. SIAM, Philadelphia, PA, 2000.

[123] G. Evans. *Numerical Methods for Partial Differential Equations*. Springer, London, New York, 2000.

[124] D. Gottlieb and S.A. Orszag. *Numerical Analysis of Spectral Methods : Theory and Applications*. Philadelphia, Pa, 1977.

[125] B. Mercier. *An introduction to the numerical analysis of spectral methods.* Springer-Verlag, Berlin ; New York, 1989.

[126] J.P. Boyd. *Chebyshev and Fourier Spectral Methods.* Springer-Verlag, Berlin ; New York, 1989.

[127] R.G. Voigt, D. Gottlieb, and M.Y. Hussaini, editors. *Spectral Methods for Partial Differential Equations.* SIAM, 1984.

[128] M. Seul and D. Andelman. Domain shapes and patterns - the phenomenology of modulated phases. *Science*, 267(5197):476–483, 1995.

[129] N. Bowden, S. Brittain, A.G. Evans, J.W. Hutchinson, and G.M. Whitesides. Spontaneous formation of ordered structures in thin films of metals supported on an elastomeric polymer. *Nature*, 393(6681):146–149, 1998.

[130] P.J. Yoo and H.H. Lee. Evolution of a stress-driven pattern in thin bilayer films: Spinodal wrinkling. *Physical Review Letters*, 91(15):154502, 2003.

[131] W. Lu and Z. Suo. Dynamics of nanoscale pattern formation of an epitaxial monolayer. *Journal of the Mechanics and Physics of Solids*, 49(9):1937–1950, 2001.

[132] Z.Y. Huang, W. Hong, and Z. Suo. Evolution of wrinkles in hard films on soft substrates. *Physical Review E*, 70(3):030601, 2004.

[133] Z. Suo and W. Wang. Diffusive void bifurcation in stressed solid. *Journal of Applied Physics*, 76(6):3410–3421, 1994.

[134] J.A. Floro, S.J. Hearne, J.A. Hunter, P. Kotula, E. Chason, S.C. Seel, and C.V. Thompson. The dynamic competition between stress generation and relaxation mechanisms during coalescence of Volmer-Weber thin films. *Journal of Applied Physics*, 89(9):4886–4897, 2001.

[135] P. Berger, P. Kohlert, K. Kassner, and C. Misbah. Pattern selection in biaxially stressed solids. *Physical Review Letters*, 90(17):176103, 2003.

[136] J. Paret. Long-time dynamics of the three-dimensional biaxial Grinfeld instability. *Physical Review E*, 72(1):011105, 2005.

[137] J.A. Floro, G.A. Lucadamo, E. Chason, L.B. Freund, M. Sinclair, R.D. Twesten, and R.Q. Hwang. SiGe island shape transitions induced by elastic repulsion. *Physical Review Letters*, 80(21):4717–4720, 1998.

[138] Q.H. Xie, A. Madhukar, P. Chen, and N.P. Kobayashi. Vertically self-organized InAs quantum box islands on GaAs(100). *Physical Review Letters*, 75(13):2542–2545, 1995.

[139] G. Jin, Y.S. Tang, J.L. Liu, and K.L. Wang. Self-organized Ge quantum wires on Si(111) substrates. *Journal of Vacuum Science & Technology a-Vacuum Surfaces and Films*, 17(4):1406–1409, 1999.

[140] G. Jin, Y.S. Tang, J.L. Liu, and K.L. Wang. Growth and study of self-organized Ge quantum wires on Si(111) substrates. *Applied Physics Letters*, 74(17):2471–2473, 1999.

[141] Y.W. Zhang. Surface stability and evolution of biaxially strained epitaxial thin films. *Applied Physics Letters*, 87(12):121916, 2005.

[142] P. Liu, Y.W. Zhang, and C. Lu. Anisotropy effect on heteroepitaxial growth of self-assembled islands. *Applied Physics Letters*, 88(4):41922, 2006.

[143] W. Lu and Z. Suo. Symmetry breaking in self-assembled monolayers on solid surfaces. II. anisotropic substrate elasticity. *Physical Review B*, 65(20):205418, 2002.

[144] R.V. Kukta, N. Vasiljevic, N. Dimitrov, and K. Sieradzki. Self-assembly of paired nanoribbons. *Physical Review Letters*, 95(18):186103, 2005.

[145] P. Liu, Y.W. Zhang, and C. Lu. Three-dimensional finite-element simulations of the self-organized growth of quantum dot superlattices. *Physical Review B*, 68(19):195314, 2003.

[146] P. Sutter and M.G. Lagally. Nucleationless three-dimensional island formation in low-misfit heteroepitaxy. *Physical Review Letters*, 84(20):4637–4640, 2000.

[147] C. Roland and G.H. Gilmer. Growth of germanium films on Si(001) substrates. *Physical Review B*, 47(24):16286–16298, 1993.

[148] G. Abstreiter, P. Schittenhelm, C. Engel, E. Silveira, A. Zrenner, D. Meertens, and W. Jager. Growth and characterization of self-assembled Ge-rich islands on Si. *Semiconductor Science and Technology*, 11(11):1521–1528, 1996.

[149] Z.M. Jiang, X.M. Jiang, W.R. Jiang, Q.J. Jia, W.L. Zheng, and D.C. Qian. Lattice strains and composition of self-organized Ge dots grown on Si(001). *Applied Physics Letters*, 76(23):3397–3399, 2000.

[150] T. Kitajima, B. Liu, and S.R. Leone. Two-dimensional periodic alignment of self-assembled Ge islands on patterned Si(001) surfaces. *Applied Physics Letters*, 80(3):497–499, 2002.

[151] L. Vegard. Die konstitution der mischkristalle und die raumfullung der atome. *Zeitschrift fuer Physik*, 5, 1921.

[152] A.A. Stekolnikov, J. Furthmuller, and F. Bechstedt. Absolute surface energies of group-IV semiconductors: Dependence on orientation and reconstruction. *Physical Review B*, 65(11):115318, 2002.

[153] A.A. Stekolnikov, J. Furthmuller, and F. Bechstedt. Adatoms, dimers, and interstitials on group-IV(113) surfaces: First-principles studies of energetical, structural, and electronic properties. *Physical Review B*, 67(19), 2003.

[154] B.G. Orr, D. Kessler, C.W. Snyder, and L. Sander. A model for strain-induced roughening and coherent island growth. *Europhysics Letters*, 19:33–38, 1992.

[155] J.L. Gray, R. Hull, C.H. Lam, P. Sutter, J. Means, and J.A. Floro. Beyond the heteroepitaxial quantum dot: Self-assembling complex nanostructures controlled by strain and growth kinetics. *Physical Review B*, 72(15):155323, 2005.

[156] D.E. Jesson, S.J. Pennycook, J.M. Baribeau, and D.C. Houghton. Direct imaging of surface cusp evolution during strained-layer epitaxy and implications for strain relaxation. *Physical Review Letters*, 71(11):1744–1747, 1993.

[157] G.K. Gueorguiev, J.M. Pacheco, and D. Tomanek. Quantum size effects in the polarizability of carbon fullerenes. *Physical Review Letters*, 92(21):215501, 2004.

[158] J. Eisenmenger, Z.P. Li, W.A.A. Macedo, and I.K. Schuller. Exchange bias and asymmetric reversal in nanostructured dot arrays. *Physical Review Letters*, 94(5):057203, 2005.

[159] V. Ng, Y.V. Lee, B.T. Chen, and A.O. Adeyeye. Nanostructure array fabrication with temperature-controlled self-assembly techniques. *Nanotechnology*, 13(5):554–558, 2002.

[160] Y. Chen, D.A.A. Ohlberg, and R.S. Williams. Nanowires of four epitaxial hexagonal silicides grown on Si(001). *Journal of Applied Physics*, 91(5):3213–3218, 2002.

[161] G. Kaltsas, A. Travlos, A.G. Nassiopoulos, N. Frangis, and J. VanLanduyt. High crystalline quality erbium silicide films on (100)silicon, grown in high vacuum. *Applied Surface Science*, 102:151–155, 1996.

[162] N. Frangis, J. VanLanduyt, G. Kaltsas, A. Travlos, and A.G. Nassiopoulos. Growth of erbium-silicide films on (100) silicon as characterised by electron microscopy and diffraction. *Journal of Crystal Growth*, 172(1-2):175–182, 1997.

[163] J.E. Baglin, F.M.D. Heurle, and C.S. Petersson. The formation of silicides from thin-films of some rare-earth-metals. *Applied Physics Letters*, 36(7):594–596, 1980.

[164] A. Travlos, N. Salamouras, and N. Boukos. Growth, structure and electrical properties of epitaxial thulium silicide thin films on silicon. *Journal of Applied Physics*, 81(3):1217–1221, 1997.

[165] C.H. Luo, G.H. Shen, and L.J. Chen. Vacancy ordering structures in epitaxial RESi2-x thin films on (111)Si and (001)Si. *Applied Surface Science*, 113/114:457–461, 1997.

[166] W. Zhou, Y. Zhu, T. Ji, X. Hou, and Q. Cai. Formation and evolution of erbium silicide nanowires on vicinal and flat Si(001). *Nanotechnology*, 17:852–858, 2006.

[167] E. Houssay, A. Rouault, O. Thomas, R. Madar, and J.P. Senateur. Metallurgical reinvestigation of rare earth silicides. *Applied Surface Science*, 38:156–161, 1989.

[168] J. Magaud, A. Pasturel, G. Kresse, and J. Hafner. Role of silicon vacancies in yttrium-disilicide compounds from ab initio calculations. *Physical Review B*, 55:13479, 1997.

[169] D.J. Chadi. Stabilities of single-layer and bilayer steps on Si(001) surfaces. *Physical Review Letters*, 59(15):1691–1694, 1987.

[170] K. Hausler, K. Eberl, F. Noll, and A. Trampert. Strong alignment of self-assembling InP quantum dots. *Physical Review B*, 54(7):4913–4918, 1996.

[171] K.M. Kim, Y.J. Park, Y.M. Park, C.K. Hyon, E.K. Kim, and J.H. Park. Alignment of InAs quantum dots on a controllable strain-relaxed sub-

strate using an InAs/GaAs superlattice. *Journal of Applied Physics*, 92(9):5453–5456, 2002.

[172] Q. Gong, R. Notzel, G.J. Hamhuis, T.J. Eijkemans, and J.H. Wolter. Self-organized strain engineering on GaAs(311) B: Template formation for quantum dot nucleation control. *Applied Physics Letters*, 81(17):3254–3256, 2002.

[173] B.C. Lee, S.D. Lin, C.P. Lee, H.M. Lee, J.C. Wu, and K.W. Sun. Selective growth of single InAs quantum dots using strain engineering. *Applied Physics Letters*, 80(2):326–328, 2002.

[174] A. Konkar, A. Madhukar, and P. Chen. Stress-engineered spatially selective self-assembly of strained InAs quantum dots on nonplanar patterned GaAs(001) substrates. *Applied Physics Letters*, 72(2):220–222, 1998.

[175] S. Kohmoto, H. Nakamura, T. Ishikawa, and K. Asakawa. Site-controlled self-organization of individual InAs quantum dots by scanning tunneling probe-assisted nanolithography. *Applied Physics Letters*, 75(22):3488–3490, 1999.

[176] T. Ishikawa, T. Nishimura, S. Kohmoto, and K. Asakawa. Site-controlled InAs single quantum-dot structures on GaAs surfaces patterned by in situ electron-beam lithography. *Applied Physics Letters*, 76(2):167–169, 2000.

[177] J. Boussinesq. *Application des Potentiels a l'etude de l'equilibre et du mouvement des solides elastiques*. Gauthier-Villars, 1885.

[178] V. Cerruti. *Roma Acc. Lincei Mem. Fis. Mat.* 1882.

[179] S.G. Lekhnitskii. *Theory of Elasticity of an Anisotropic Elastic Body.* Holden-Day, San Francisco, 1963.

[180] A.N. Stroh. Dislocations and cracks in anisotropic elasticity. *Philosophical Magazine*, 3:625–646, 1958.

[181] A.N. Stroh. Steady-state problems in anisotropic elasticity. *Journal of Mathematical Physics*, 41:77–103, 1962.

[182] T.C.T. Ting. *Anisotropic Elasticity.* Oxford University Press, New York, 1996.

[183] K.C. Wu. Generalization of the Stroh formalism to 3-dimensional anisotropic elasticity. *Journal of Elasticity*, 51:213–225, 1998.

[184] J.R. Willis. Hertzian contact of anisotropic bodies. *Journal of the Mechanics and Physics of Solids*, 14:163–176, 1966.

Vita

Yaoyu Pang was born in Changzhou, Jiangsu Province, China on August 25, 1979, the son of Jiacong Pang and Lanping Yao. After completing his 5-year special class for gifted young at Changzhou Senior Middle School of Jiangsu Province in 1997, he entered Beijing Institute of Technology in Beijing and received degree of B.S. in Engineering Mechanics in July 2001. In August 2002, Yaoyu Pang started his graduate study in the Engineering Mechanics Department at the University of Texas at Austin, and received his M.S.E. degree in December 2004. After that, Yaoyu Pang continued his graduate study in the same department for his Ph.D. degree.

Permanent Address: LaoDong XinCun 73-D-301

Changzhou, Jiangsu, 213003

P.R.China

This dissertation was typeset with $\text{\LaTeX}\,2_\varepsilon$[1] by the author.

---

[1]$\text{\LaTeX}\,2_\varepsilon$ is an extension of LaTeX. LaTeX is a collection of macros for TeX. TeX is a trademark of the American Mathematical Society. The macros used in formatting this dissertation were written by Dinesh Das, Department of Computer Sciences, The University of Texas at Austin, and extended by Bert Kay, James A. Bednar, and Ayman El-Khashab.